arXiv:2108.05455v3 [astro-ph.SR] 10 Mar 2022

The K2 Galactic Archaeology Program Data Release 3: Age-abundance patterns in C1-C8, C10-C18

Joel C. Zinn,[1, 2, *] Dennis Stello,[2, 3, 4, 5] Yvonne Elsworth,[6, 4] Rafael A. García,[7] Thomas Kallinger,[8]
Savita Mathur,[9, 10] Benoît Mosser,[11] Marc Hon,[2] Lisa Bugnet,[7, 12] Caitlin Jones,[6] Claudia Reyes,[2]
Sanjib Sharma,[3, 5] Ralph Schönrich,[13] Jack T. Warfield,[14, 15] Rodrigo Luger,[16, 17] Andrew Vanderburg,[18]
Chiaki Kobayashi,[19] Marc H. Pinsonneault,[14] Jennifer A. Johnson,[14] Daniel Huber,[20] Sven Buder,[21, 5]
Meridith Joyce,[21, 5] Joss Bland-Hawthorn,[3, 5] Luca Casagrande,[22] Geraint F. Lewis,[3] Andrea Miglio,[4, 6]
Thomas Nordlander,[21, 5] Guy R. Davies,[6, 4] Gayandhi De Silva,[23, 24, 5] William J. Chaplin,[6, 4] and
Victor Silva Aguirre[4]

[1]Department of Astrophysics, American Museum of Natural History, Central Park West at 79th Street, New York, NY 10024, USA
[2]School of Physics, University of New South Wales, Barker Street, Sydney, NSW 2052, Australia
[3]Sydney Institute for Astronomy, School of Physics, A28, The University of Sydney, NSW 2006, Australia
[4]Stellar Astrophysics Centre, Department of Physics and Astronomy, Aarhus University, Ny Munkegade 120, DK-8000 Aarhus C,
Denmark
[5]ARC Centre of Excellence for All Sky Astrophysics in 3 Dimensions (ASTRO 3D), Australia
[6]School of Physics and Astronomy, University of Birmingham, Edgbaston, Birmingham, B15 2TT, UK
[7]AIM, CEA, CNRS, Université Paris-Saclay, Université Paris Diderot, Sorbonne Paris Cité, F-91191 Gif-sur-Yvette, France
[8]Institute of Astrophysics, University of Vienna, Türkenschanzstrasse 17, Vienna 1180, Austria
[9]Instituto de Astrofísica de Canarias, La Laguna, Tenerife, Spain
[10]Dpto. de Astrofísica, Universidad de La Laguna, La Laguna, Tenerife, Spain
[11]LESIA, Observatoire de Paris, PSL Research University, CNRS, Sorbonne Université, Université de Paris Diderot, 92195 Meudon,
France
[12]Flatiron Institute, Simons Foundation, 162 Fifth Ave, New York, NY 10010, USA
[13]Mullard Space Science Laboratory, University College London, Holmbury St Mary, Dorking RH5 6NT, UK
[14]Department of Astronomy, The Ohio State University, 140 West 18th Avenue, Columbus OH 43210, USA
[15]Department of Physics, The Ohio State University, 191 West Woodruff Avenue, Columbus OH 43210
[16]Center for Computational Astrophysics, Flatiron Institute, New York, NY, USA
[17]Virtual Planetary Laboratory, University of Washington, Seattle, WA, USA
[18]Department of Astronomy, The University of Texas at Austin, Austin, TX 78712, USA
[19]Centre for Astrophysics Research, Department of Physics, Astronomy and Mathematics, University of Hertfordshire, Hatfield, AL10
9AB, UK
[20] Institute for Astronomy, University of Hawai'i, 2680 Woodlawn Drive, Honolulu, HI 96822, USA
[21]Research School of Astronomy and Astrophysics, Australian National University, Canberra, ACT 2611, Australia
[22]Research School of Astronomy and Astrophysics, Mount Stromlo Observatory, The Australian National University, ACT 2611, Australia
[23]Australian Astronomical Optics, Faculty of Science and Engineering, Macquarie University, Macquarie Park, NSW 2113, Australia
[24]Macquarie University Research Centre for Astronomy, Astrophysics & Astrophotonics, Sydney, NSW 2109, Australia

ABSTRACT

We present the third and final data release of the K2 Galactic Archaeology Program (K2 GAP) for Campaigns C1-C8 and C10-C18. We provide asteroseismic radius and mass coefficients, κ_R and κ_M, for $\sim 19,000$ red giant stars, which translate directly to radius and mass given a temperature. As such, K2 GAP DR3 represents the largest asteroseismic sample in the literature to date. K2 GAP DR3 stellar parameters are calibrated to be on an absolute parallactic scale based on Gaia DR2, with red giant branch and red clump evolutionary state classifications provided via a machine-learning approach. Combining these stellar parameters with GALAH DR3 spectroscopy, we determine asteroseismic ages with precisions of $\sim 20 - 30\%$ and compare age-abundance relations to Galactic chemical evolution models among both low- and high-α populations for α, light, iron-peak, and neutron-capture elements. We confirm recent indications in the literature of both increased Ba production at late Galactic times,

Corresponding author: Joel C. Zinn
jzinn@amnh.org

as well as significant contribution to r-process enrichment from prompt sources associated with, e.g., core-collapse supernovae. With an eye toward other Galactic archaeology applications, we characterize K2 GAP DR3 uncertainties and completeness using injection tests, suggesting K2 GAP DR3 is largely unbiased in mass/age and with uncertainties of $2.9\%\,(\text{stat.})\pm0.1\%\,(\text{syst.})$ & $6.7\%\,(\text{stat.})\pm0.3\%\,(\text{syst.})$ in κ_R & κ_M for red giant branch stars and $4.7\%\,(\text{stat.})\pm0.3\%\,(\text{syst.})$ & $11\%\,(\text{stat.})\pm0.9\%\,(\text{syst.})$ for red clump stars. We also identify percent-level asteroseismic systematics, which are likely related to the time baseline of the underlying data, and which therefore should be considered in TESS asteroseismic analysis.

1. INTRODUCTION

Studies of Galactic chemical evolution have mostly focussed on targets in the solar neighborhood, where stars are relatively easy to observe, and which was the sole domain, historically, of precise parallaxes, and therefore, stellar ages (e.g., Nordström et al. 2004). Because stars for the most part maintain their birth abundances, stellar abundances and ages can be used to infer the chemical enrichment history of the Galaxy, providing information on the details of contributions to the insterstellar medium from nucleosynthetic channels like supernovae and stellar winds.

The local stellar population has been found to have a bimodal chemical distribution in alpha elements (e.g., O, Mg, Ca, Si) as seen in $[\alpha/\text{Fe}]$ versus $[\text{Fe/H}]$[1]: there exists one population of low-α stars with spatial distributions apparently more confined to the plane of the Galaxy and with intermediate to young ages, and there exists another population of high-α stars with hotter kinematics; centrally-concentrated spatial distributions in the disk; and older ages (e.g., Fuhrmann 1998; Prochaska et al. 2000; Gratton et al. 2000; Bensby et al. 2003; Haywood et al. 2013). With the understanding that α elements are produced primarily in core-collapse supernovae (CCSNe), with some contributions to the heavier nuclei from Type Ia supernovae (SNe Ia), whereas iron is mostly produced in SNe Ia, the low-α population has been interpreted as having mostly contributions from SNe Ia and the high-α population has been interpreted as having mostly contributions from CCSNe (Burbidge et al. 1957; Timmes et al. 1995).

Studies of stellar populations beyond the solar neighborhood have shown that the low-α and high-α populations maintain their chemical bimodality, and to a certain extent, their distinct radial spatial distributions, with the high-alpha stars more centrally concentrated (Nidever et al. 2014; Hayden et al. 2015), though not necessarily intrinsically having a different vertical spatial distribution (Hayden et al. 2017). There are also

interesting chemical distinctions among these populations when looking at non–α-element abundance ratios (e.g., Prochaska et al. 2000; Bensby et al. 2003; Adibekyan et al. 2012; Weinberg et al. 2019; Griffith et al. 2019; Nissen et al. 2020). Given expectations that the bimodality is ultimately related to different chemical enrichment histories, it is natural to ask how these populations evolved, and, in so doing, test understandings of the nucleosynthetic production sites' yields with time. Indeed, the underlying origin of these spatial and chemical distinctions is under debate (e.g., Chiappini et al. 1997; Schönrich & Binney 2009a,b; Kobayashi & Nakasato 2011; Minchev et al. 2015; Hayden et al. 2017; Mackereth et al. 2018; Spitoni et al. 2019; Clarke et al. 2019).

Thanks to an unprecedented collection of well-measured stellar kinematics from Gaia (Gaia Collaboration et al. 2016, 2018), and with large spectrocopic surveys like APOGEE (Majewski et al. 2017), GALAH (De Silva et al. 2015), and LAMOST (Newberg et al. 2012) providing hundreds of thousands of detailed abundance measurements probing well beyond the solar vicinity, the bottleneck to progress on the origin and evolution of the elements in the Galaxy becomes stellar age.

Stellar composition has historically been used as a proxy for stellar age, based on the idea that Galactic enrichment increases with time, with input to the interstellar medium through asymptotic giant branch (AGB) stars, SNe Ia, and CCSNe continually injecting metals over time according to so-called delay-time distributions, in ratios that themselves depend on time due to the birth composition of the stars producing the elements changing (Tinsley 1979; McWilliam 1997). Kinematic information can also serve as an age proxy, with older stellar populations experiencing dynamical heating from discrete merger events (e.g., Grand et al. 2016) as well as secular processes involving, e.g., spiral arms (Carlberg & Sellwood 1985; Minchev & Quillen 2006); the central bar (Saha et al. 2010; Grand et al. 2016); and giant molecular clouds (e.g., Spitzer & Schwarzschild 1951).

To make precise statements about the chemical evolution of the Galaxy, however, requires genuine stellar age estimates independent of kinematics and abundances so as to not assume the age-abundance patterns under

---

[1] Here and throughout the paper we use the standard notation $[\text{X/Fe}] \equiv \log_{10}\left(\frac{\text{X}}{\text{Fe}}\right) - \log_{10}\left(\frac{\text{X}_\odot}{\text{Fe}_\odot}\right)$.

question. Work appealing to stellar ages to solve this conundrum has either made recourse to turnoff stars — whose ages can be reliably determined through isochrone matching (Pont & Eyer 2004; Jørgensen & Lindegren 2005; Lin et al. 2019), but which are relatively dim and therefore probe predominantly local volumes — or to spectroscopic ages (e.g., Sun et al. 2020; Ness et al. 2016). Although machine learning–based spectroscopic ages have increased sample sizes to hundreds of thousands, they do not seem to yield reliable for ages > 8 Gyr (Ting & Rix 2019). Another approach is to make reference to Galactic stellar population models, and match a predicted age-color relation to observed colors (e.g., Bland-Hawthorn et al. 2019). As we will show here, such photometric ages — with typical uncertainties of 30-50% — are significantly less precise than the 20-30% K2 asteroseismic age uncertainties we present here.

Because asteroseismic ages do not assume either an age-kinematics relation or age-metallicity relation, they can provide interesting constraints on Galactic chemical evolution. Indeed, asteroseismic ages have supported literature estimates that the two α populations have different age distributions (e.g., Silva Aguirre et al. 2018; Miglio et al. 2021), while complicating the understanding that the high-α population is uniformly old (Chiappini et al. 2015; Anders et al. 2017; Warfield et al. 2021). These studies have mostly been limited to asteroseismic data from the Kepler mission (Borucki et al. 2008), which probes a single, 100 sq. deg. field of view at roughly fixed Galactic radius corresponding to that of the Sun. With the extended Kepler mission, K2 (Howell et al. 2014), has come access to regions of the sky across the ecliptic, and exploratory work based on data from four K2 campaigns has shown promise for better understanding the α bimodality (Rendle et al. 2019; Warfield et al. 2021). The K2 Galatic Archaeology Program (GAP; Stello et al. 2015) takes advantage off this opportunity, targeting red giant stars with the express intent of investigating the chemical evolution of the Galaxy beyond the solar vicinity using asteroseismic ages.

In this paper, we describe the final data release of K2 GAP, which combines red giant asteroseismic data from Campaign 1 (C1) from K2 GAP DR1 (Stello et al. 2017) and data from C4, C6, & C7 from K2 GAP DR2 (Zinn et al. 2020) with results from the remaining K2 campaigns. In K2 GAP Data Release 3 (DR3), we improve upon K2 GAP DR2 by verifying the accuracy and precision of asteroseismology with an injection test exercise, and calibrate our results against Gaia DR2 (Gaia Collaboration et al. 2018) radii[2]. Finally, we derive ages based on these calibrated asteroseismic masses in order to compare abundance enrichment histories of low- and high-α populations with Galactic chemical evolution models from Kobayashi et al. (2020a).

2. DATA

2.1. *Asteroseismic data*

In this data release, we add asteroseismic data from C2, C3, C5, C8, and C10-C18 to results from C1 from K2 GAP DR1 (Stello et al. 2017) and C4, C6, & C7 from K2 GAP DR2 (Zinn et al. 2020). In what follows, we describe the procedure to derive the asteroseismic values for stars in these new campaigns, and we also describe how the results from all of the campaigns are combined together.

The majority of K2 GAP targets were chosen to satisfy simple color and magnitude cuts, with a minority chosen based on surface gravity selections from spectroscopic surveys (APOGEE [Majewski et al. 2010], SEGUE [Yanny et al. 2009]; or RAVE [Steinmetz et al. 2006]). Most of the campaigns have targets that are chosen based on a $J - K_{\rm s} > 0.5$ color cut and a magnitude cut of $9 \lesssim V \lesssim 15$, where the visual magnitude is computed from 2MASS photometry according to

$$V \approx K_{\rm s} + 2((J - K_{\rm s}) + 0.14) + 0.256e^{2(J-K_{\rm s})},$$

which is a relation introduced by (De Silva et al. 2015). The targets were prioritized for the most part by ranking targets in order of brightest to faintest visual magnitude, with higher priority given to targets selected based on spectroscopy.

The majority of the targeted stars were observed by K2, and follow the target selection functions, with a few exceptions. Notably, the priorities of C7 targets were mistakenly reversed during the Kepler office target list consolidation. For details of the effects of this on the C7 selection function, see Zinn et al. (2020) and Sharma et al. (2019); the selection functions for all the campaigns are described in S. Sharma et al., submitted. In addition, module 4 failed while taking data in C10. We therefore exclude data from this module in C10 because of the short duration of data collection before the failure; modules 3 and 7 had already failed by the time the K2

---

[2] Here and throughout the text, when we mention Gaia radii, we refer to radii we calculate using APOGEE spectroscopy and Gaia parallaxes, according to the Stefan-Boltzmann law. These radii are distinct from the `radius_val` values provided as part of Gaia DR2; the latter are not as accurate as we require here because they do not account for extinction, and assume inhomogeneous temperatures. See §4 for details.

mission began, and so there are no data for these modules in K2 GAP. These missing modules can be seen in the K2 GAP DR3 footprint shown in Figure 1.

There are known systematics in the K2 light curves that require special processing beyond the raw light curves produced by the K2 office. In particular, the K2 satellite repositioned itself every ~6 hours to maintain pointing following the partial failure of its gyroscope system. These thruster firings induce trends in the light curves that would hinder asteroseismic analysis. The light curves used in our analysis were therefore detrended from the raw K2 data using the EVEREST pipeline (Luger et al. 2018) for all observed K2 GAP target stars except C1, for which we used the K2SFF pipeline (Vanderburg & Johnson 2014), and targets classified as extended in the Ecliptic Plane Input Catalog (EPIC; Huber et al. 2016), which were not processed by EVEREST. C10 suffered a failure of module 4 shortly into the start of the campaign, and so we did not use data from targets on module 4. C11 was separated into two parts due to a roll angle correction such that some stars had light curves only for one part of the campaign; we combined the light curves of the two parts when available for the same target. C18 lasted about 50d due to the spacecraft running low on fuel, and has correspondingly reduced quality data. C19 only had about a week's worth of data with pointing comparable to previous campaigns, and, as such, we do not consider the data from C19 in this data release.

Following this detrending, we removed non-asteroseismic variability using a boxcar high-pass filter with a width of 4 days, and performed sigma-clipping to reject flux values more than 4-σ discrepant. For the campaigns new to this data release, we additionally regularized the spectral window function by inpainting any gaps in the light curves according to the algorithm of García et al. (2014) and Pires et al. (2015).

2.2. *Spectroscopic data*

APOGEE DR16 (Ahumada et al. 2020) spectroscopic data are used for calibrating the asteroseismic data (§4). APOGEE DR16 is part of SDSS-IV (Blanton et al. 2017), and which is described in Ahumada et al. (2020). APOGEE observes in the H-band using the high-resolution ($R \sim 22,500$) APOGEE spectrograph (Wilson et al. 2019) mounted on the Sloan Foundation 2.5-m telescope (Gunn et al. 2006) at Apache Point Observatory. APOGEE observes about half of its targets in the disc, with Galactic latitude, $b \leq 16°$, with dedicated selection of the bulge, halo, and special programs comprising the rest of its observing allotment. Targets are selected according to color-magnitude cuts of

$J - K_\mathrm{s} \geq 0.5$ and $7 \lesssim H \lesssim 14$, across the sky (Zasowski et al. 2013, 2017). The data are reduced according to Nidever et al. (2015), using the APOGEE Stellar Parameters and Chemical Abundances Pipeline, (ASPCAP; Holtzman et al. 2015; García Pérez et al. 2016). The final stellar parameter calibration and validation process is discussed by Holtzman et al. (2018).

GALAH data are used for our analysis of age-abundance patterns (§5). GALAH is an optical spectroscopic survey targeting stars in the Galactic disc with $12 < V < 14$ and $|b| > 10°$ (Martell et al. 2017). The survey operates from the 3.9-m Anglo-Australian Telescope at Siding Spring Observatory in Australia, using the HERMES multi-object spectrograph (Sheinis et al. 2014). HERMES's high resolution ($R \sim 28,000$) spectra are reduced according to the procedure documented in Kos et al. (2017). GALAH DR2 presented spectroscopic parameters from The Cannon (Ness et al. 2015), trained on a subset of $\sim 11,000$ stars (Buder et al. 2018; Heiter et al. 2015) using Spectroscopy Made Easy (SME; Valenti & Piskunov 1996; Piskunov & Valenti 2017). In this work, we use abundances from GALAH DR3, which improves upon GALAH DR2 by deriving stellar parameters and abundances for all stars directly through the spectroscopic analysis code SME, which performs on-the-fly spectrum synthesis calculations; this reduces potential bias from selection effects in the Cannon training process (e.g., Holtzman et al. 2018). The SME analysis code utilises grids of pre-computed non-LTE departure coefficients for thirteen chemical elements; these grids and the models they are based on are presented by Amarsi et al. (2020; and references therein), and are publicly available (Amarsi 2020).

3. METHODS

3.1. *Asteroseismic radius and mass scaling relations*

Given the large sample size of the K2 GAP targets, it is not feasible to fit individual modes for each star to determine mass and radius. Instead, we condense the modes' information to two quantities, which can be measured relatively straightforwardly and which are related to the mass and radius of a star through so-called scaling relations.

The first of these quantities, the frequency at maximum acoustic power, ν_max, is thought to be related to the acoustic cutoff frequency, and therefore with the surface gravity of the star (Brown et al. 1991; Kjeldsen & Bedding 1995; Chaplin et al. 2008; Belkacem et al. 2011). Assuming this relation holds homologously across evolutionary state, this implies a scaling relation of the form
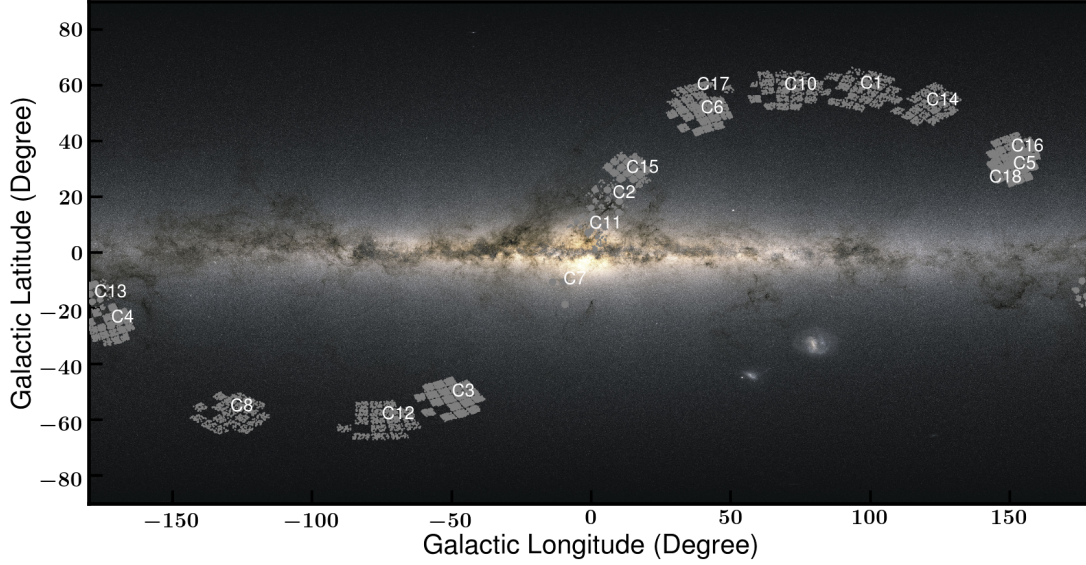
Figure 1. Distribution of the K2 GAP sample across the sky. Targets in dense fields close to the Galactic plane were selected only within 1-degree circles centered on each module rather than across entire modules. Also visible are the rectangular gaps corresponding to CCD modules 3 & 7, which failed prior to the start of the K2 mission, and module 4, which failed during Campaign 10. Background image modified from ESA/Gaia/DPAC.

$$\frac{\nu_{\max}}{\nu_{\max,\odot}} \approx \frac{M/M_\odot}{(R/R_\odot)^2\sqrt{(T_{\mathrm{eff}}/T_{\mathrm{eff},\odot})}}. \qquad (1)$$

The second quantity of interest, the large frequency separation, $\Delta\nu$, describes the frequency difference between modes of consecutive radial order that share the same degree. A second, independent scaling relation relates $\Delta\nu$ to the average stellar density (Ulrich 1986; Kjeldsen & Bedding 1995)

$$\frac{\Delta\nu}{\Delta\nu_\odot} \approx \sqrt{\frac{M/M_\odot}{(R/R_\odot)^3}}. \qquad (2)$$

The latter scaling relation is well-understood theoretically, and is valid, strictly speaking, in the limit of large radial order. However, given a stellar structure model, one can compute the expected $\Delta\nu$ at the observed radial order as well as a $\Delta\nu$ in the limit of large radial order, and therefore derive a correction factor, $f_{\Delta\nu}$, to translate the observed $\Delta\nu$ to the large radial order $\Delta\nu$ that enters into Equation 2 (e.g., White et al. 2011; Sharma et al. 2016). We therefore use a modified version of Equation 2:

$$\frac{\Delta\nu}{f_{\Delta\nu}\Delta\nu_\odot} \approx \sqrt{\frac{M/M_\odot}{(R/R_\odot)^3}}. \qquad (3)$$

Note that these corrections do not take into account frequency shifts due to the approximations of adiabatic thermal structures and mixing length theory widely used in stellar evolution models (e.g., Jørgensen et al. 2020, 2021). However, such considerations are secondary adjustments to $f_{\Delta\nu}$, given the empirical success of $f_{\Delta\nu}$ in producing agreement of asteroseismic radii and masses with independent estimates (e.g., Huber et al. 2017; Brogaard et al. 2018; Zinn et al. 2019b). We opt to use the $f_{\Delta\nu}$ corrections from Sharma et al. (2016), which are computed on a star-by-star basis according to the star's properties (e.g., temperature, metallicity, etc.) by interpolation in a grid of theoretically computed $f_{\Delta\nu}$. The asfgrid code to compute $f_{\Delta\nu}$ values is publicly available (Sharma et al. 2016; Sharma & Stello 2016)[3]

In analogy with corrections to the $\Delta\nu$ scaling relation, there are observational indications that the $\nu_{\max}$ scaling relation of Equation 1 should be modified to include a correction to the observed $\nu_{\max}$, $f_{\nu_{\max}}$ (Epstein et al. 2014; Yıldız et al. 2016; Huber et al. 2017; Viani et al. 2017; Kallinger et al. 2018). For this reason, we use a modified $\nu_{\max}$ scaling relation:

$$\frac{\nu_{\max}}{f_{\nu_{\max}}\nu_{\max,\odot}} \approx \frac{M/M_\odot}{(R/R_\odot)^2\sqrt{(T_{\mathrm{eff}}/T_{\mathrm{eff},\odot})}}. \qquad (4)$$

[3] http://www.physics.usyd.edu.au/k2gap/Asfgrid/

Table 1. Solar reference values for each pipeline contributing to K2 GAP DR3

Pipeline	$\nu_{\mathrm{max},\odot}$	$\Delta\nu_\odot$
A2Z	3097.33	134.92
CAN	3140	134.92
COR	3050	134.92
SYD	3090	135.1
BAM	3094	134.84
BHM	3050	134.92

Although progress is being made to make robust theoretical predictions of ν_{max} (e.g., Belkacem et al. 2013; Zhao et al. 2016; Zhou et al. 2020), it cannot yet be computed based on first principles to the precision required to be useful, as can be done for $\Delta\nu$. We therefore make empirical estimates of $f_{\nu_{\mathrm{max}}}$ in §4 for RGB and RC stars, which, in practice, are scalar values such that we can think of $f_{\nu_{\mathrm{max}}}$ as indistinguishable from a modified $\nu_{\mathrm{max},\odot}$.

The solar reference values in Equations 3 & 4 should, in theory, be measured using the same analysis as one would measure ν_{max} and $\Delta\nu$. Therefore, each pipeline has different solar reference values, which are listed in Table 1. We assume here a solar temperature of $T_{\mathrm{eff},\odot} = 5772K$ (Mamajek et al. 2015).

By re-arranging Equations 3 & 4, the radius scaling relation is found to be

$$\frac{R}{R_\odot} \approx \left(\frac{\nu_{\mathrm{max}}}{f_{\nu_{\mathrm{max}}}\nu_{\mathrm{max},\odot}}\right)\left(\frac{\Delta\nu}{f_{\Delta\nu}\Delta\nu_\odot}\right)^{-2}\left(\frac{T_{\mathrm{eff}}}{T_{\mathrm{eff},\odot}}\right)^{1/2} \tag{5}$$

$$\equiv \kappa_R \left(\frac{T_{\mathrm{eff}}}{T_{\mathrm{eff},\odot}}\right)^{1/2}, \tag{6}$$

and the mass scaling relation expression is found to be

$$\frac{M}{M_\odot} \approx \left(\frac{\nu_{\mathrm{max}}}{f_{\nu_{\mathrm{max}}}\nu_{\mathrm{max},\odot}}\right)^{3}\left(\frac{\Delta\nu}{f_{\Delta\nu}\Delta\nu_\odot}\right)^{-4}\left(\frac{T_{\mathrm{eff}}}{T_{\mathrm{eff},\odot}}\right)^{3/2} \tag{7}$$

$$\equiv \kappa_M \left(\frac{T_{\mathrm{eff}}}{T_{\mathrm{eff},\odot}}\right)^{3/2}. \tag{8}$$

Here, we have factored out the dependence on temperature. Since the majority of the K2 GAP DR3 stars do not have spectroscopic temperature estimates, we report, as we did in K2 GAP DR2, the radius and mass coefficients, κ_R and κ_M. This allows the user to compute radii and masses using consistent temperature scales in

the context of their work. We also provide the $f_{\Delta\nu}$ we compute according to Sharma et al. (2016) in Table 2, though to maintain complete consistency, users should re-compute these values using the same temperature scale as they do to convert radius and mass coefficients into radii and masses. As a reference, should there be a $100K$ discrepancy in the EPIC temperatures used to compute $f_{\Delta\nu}$ as we do here and the user's temperatures, a 1% systematic would be introduced into $f_{\Delta\nu}$. Users may generate their own $f_{\Delta\nu}$ values using the publicly-available `asfgrid` code.

3.2. Derived asteroseismic parameters

We make use of the same pipelines as the previous K2 GAP data releases to extract these aforementioned asteroseimsic quantities, ν_{max} and $\Delta\nu$, from K2 light curves: A2Z (Mathur et al. 2010); BAM (Zinn et al. 2019c); BHM (Hekker et al. 2010); CAN (Kallinger et al. 2010, 2016); COR (Mosser & Appourchaux 2009; Mosser et al. 2010); and SYD (Huber et al. 2009). The generalized problem that each of these pipelines addresses is to identify a regular pattern of solar-like oscillations in the presence of red and white noise. The problem of detecting solar-like oscillations in K2 data also involves systematic noise that can mimic solar-like oscillations (see Stello et al. 2017; Zinn et al. 2019c). Though their implementations vary, the above asteroseismic pipelines share common approaches of 1) fitting a model to the power spectrum to remove the stellar red noise; 2) fitting a Gaussian excess in power above the red noise, with a mean corresponding to ν_{max} (A2Z, BAM, BHM, CAN, COR) or heavily smoothing the excess to localize the frequency of its peak as ν_{max} (SYD); and 3) identifying $\Delta\nu$ using either individually fitted modes (CAN) or some version of the autocorrelation function (A2Z, BAM, BHM, CAN, COR, SYD). For more details on their implementation and methodology in the context of K2, please see Stello et al. (2017) and Zinn et al. (2020).[4]

We follow the procedure laid out in K2 GAP DR2 to derive average asteroseismic parameters for each star. This method is similar to the one adopted for the APOKASC-2 sample, which is described in Pinson-

---

[4] The following changes were implemented in the SYD pipeline compared to its description and use in K2 GAP DR2: 1) in addition to the nominal ν_{max} and $\Delta\nu$ confidence cuts mentioned in Zinn et al. (2020), stars are required to fall within the empirical $\Delta\nu$–ν_{max} relation from Stello et al. (2009), such that $0.75(0.262\nu_{\mathrm{max}}^{0.772}) < \Delta\nu < 1.5(0.262\nu_{\mathrm{max}}^{0.772})$; 2) stars for which $\Delta\nu$ was deemed measurable were determined based on a machine learning approach from an independent analysis of K2 data (Reyes et al. 2022).

neault et al. (2018). In short, we re-scale each of the pipeline $\nu_{\max}$ and $\Delta\nu$ values such that the average values for the entire sample across all pipelines is the same, which requires an iterative approach and results in averaged values for each star, denoted $\langle\nu'_{\max}\rangle$ and $\langle\Delta\nu'\rangle$. Three modifications have been implemented here compared to the methodology described in Zinn et al. (2020). First, the A2Z $\Delta\nu$ values are not incorporated into the $\langle\Delta\nu'\rangle$ due to a significant systematic offset from other pipeline values. Second, for stars that were observed in more than one campaign, variance-weighted averages for each pipeline are computed before proceeding, such that there is only one measurement per star. Third, whereas previously the sigma-clipping was done at the end of each iteration, we now allow the average $\nu_{\max}$ to converge before performing a 3-σ clipping and continuing the iteration process. For each star with at least two pipeline values returned, we then take the average $\nu_{\max}$ value, $\langle\nu'_{\max}\rangle$, and adopt the scatter in those $\nu_{\max}$ values as the uncertainty on $\nu_{\max}$, $\sigma_{\langle\nu'_{\max}\rangle}$. The same exercise is performed for $\Delta\nu$ to compute $\langle\Delta\nu'\rangle$ and $\sigma_{\langle\Delta\nu'\rangle}$. In so doing, we are assuming that the different pipelines have systematic differences in $\Delta\nu$ and $\nu_{\max}$ measurements that tend to cancel out when averaged together. This exercise is done for RGB and RC stars separately, based on evolutionary states computed using the machine-learning approach described in Hon et al. (2017, 2018). In brief, the machine learning approach takes advantage of the fact that red giant branch and red clump stars exhibit differences in the observed mode structure (Bedding et al. 2011). These differences are detectable by visual inspection, and are therefore amenable to being learned by machine learning algorithms. The classifier developed by Hon et al. (2017, 2018) uses a convolutional neural network — an architecture optimized for image processing — to learn characteristic red giant and red clump mode features present in power spectra rendered as 2D images. In this work, evolutionary states are assigned arbitrarily at the initial iteration, and in subsequent iterations, for stars with a defined $\langle\Delta\nu'\rangle$ and $\langle\nu'_{\max}\rangle$, machine-learning evolutionary states are assigned. The final iteration proceeds with only stars with defined $\langle\Delta\nu'\rangle$ and $\langle\nu'_{\max}\rangle$. As part of this process, each pipeline has assigned scale factors, $X_{\nu_{\max},\,\mathrm{RGB}}$, $X_{\Delta\nu,\,\mathrm{RGB}}$, $X_{\nu_{\max},\,\mathrm{RC}}$, and $X_{\Delta\nu,\,\mathrm{RC}}$ that describe by how much the pipeline-specific solar reference value (Table 1) should be multiplied to be put on the $\langle\nu'_{\max}\rangle$ and $\langle\Delta\nu'\rangle$ scale for RGB stars and RC stars, respectively. These modified solar reference values are provided in Table 3. Here, we also indicate the analogous scaling factors from APOKASC-2 (Pinsonneault et al. 2018), where differences are a result of slightly
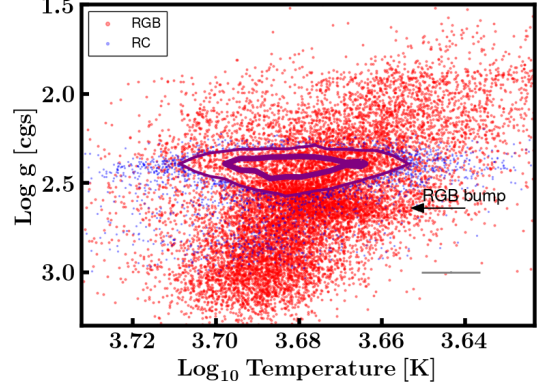

Figure 2. Kiel diagram for K2 GAP DR3, with stars colored red (blue) if classified as red giant branch stars (red clump stars). The purple curves delineate the 38% and 68% contours for red clump stars, for clarity in seeing the RGB bump (indicated by the arrow). The surface gravity is calculated using the EPIC temperature in combination with $\langle\nu'_{\max}\rangle$, according to Equation 1. The spread in temperature of the red clump is caused in part by its intrinsic width set by population-level variations in metallicity, mass, & age, and also by the EPIC temperature uncertainty, which is indicated by the typical error bar indicated in the lower right.

different methodology and due to not working with the same pipelines: BAM was not a part of the APOKASC-2 analysis. It is also likely that there are significant differences introduced in the pipeline's asteroseismic scales due to the difference between the time baselines of Kepler and K2, which we discuss in §4.

We list in Table 2 the individual, re-scaled pipeline values, $\nu'_{\max} = X_{\nu_{\max}}\nu_{\max}$ and $\Delta\nu' = X_{\Delta\nu}\Delta\nu$. As in K2 GAP DR2, we do not list $\nu'_{\max}$ or $\Delta\nu'$ if that pipeline value is sigma-clipped in the averaging procedure. We correct pipeline-specific $\Delta\nu'$ as well as $\langle\Delta\nu'\rangle$ with the theoretical $f_{\Delta\nu}$ from Sharma et al. (2016) using the EPIC temperatures & metallicities listed in Table 2. We use these re-scaled $\nu'_{\max}$ and $\Delta\nu'$ values to compute re-scaled κ'_R and κ'_M values for each star and for each pipeline, using the solar reference values appropriate for each pipeline (see Table 1). Our recommended radius and mass coefficients, $\langle\kappa_R\rangle$ and $\langle\kappa_M\rangle$, are those computed using the average parameters $\langle\nu'_{\max}\rangle$ and $\langle\Delta\nu'\rangle$ and APOKASC-2 solar reference values modified so that our radii are on the Gaia parallactic scale (see §4): $\nu_{\max,\odot,\,\mathrm{RGB}} = 3081\mu\mathrm{Hz}$, $\nu_{\max\odot,\,\mathrm{RC}} = 3096\mu\mathrm{Hz}$ and $\Delta\nu_{\odot,\,\mathrm{RGB/RC}} = 135.146\mu\mathrm{Hz}$ (Pinsonneault et al. 2018). The pipeline-specific and average radius & mass coefficients are provided in Table 4, with their uncer-
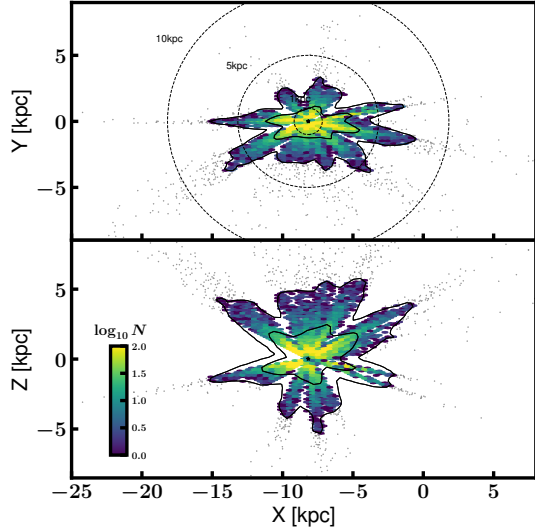
Figure 3. The distribution of K2 GAP DR3 stars (i.e., GAP targets with $\langle \nu'_{\max} \rangle$, as defined in §3.2) shown in Galacto-centric coordinates. The Sun's position of (X, Y, Z) = (-8.18kpc, 0kpc, 0.021kpc) is marked as the black star, and is taken from a combination of the distance to Sgr A* (Gravity Collaboration et al. 2019; X) and the Gaia DR2 Galactic disc velocity distribution symmetry analysis from Bennett & Bovy (2019; Z). The inner (outer) contour represents the 68th (98th) percentile of the plotted stars. Within these contours, the logarithmic density of stars is indicated according to the color bar. Dashed circles indicate distances of 1kpc, 5kpc, and 10kpc.

tainties calculated according to standard propagation of uncertainty.[5]

In K2 GAP DR2, we established that the uncertainties from our averaging process follow χ^2 statistics, and can be described to a good appproximation by fractional uncertainties that are mostly a function of evolutionary state. We report in Table 5 the median fractional uncertainties in $\langle \nu'_{\max} \rangle$, $\langle \Delta \nu' \rangle$, $\langle \kappa_R \rangle$, and $\langle \kappa_M \rangle$ for both RGB stars and RC stars, and which may be considered typical of the uncertainties in our sample. We also include typical fractional uncertainties in these parameters from K2 GAP DR2, APOKASC-2 (Pinsonneault et al. 2018), and another, independent analysis of Kepler data (Yu et al. 2018). The typical $\Delta \nu$ uncertainty for K2 GAP DR3 is somewhat larger than it was in K2 GAP DR2 due to the previously mentioned difference in how sigma clipping is performed in the averaging procedure used in the two data releases. The resulting precisions

in RGB masses, which are determinative in asteroseismic age precisions, are about a factor of two larger than those of Kepler, corresponding to uncertainties of about $20 - 30\%$ in age.

We provide all the results returned by every pipeline in Table 6. Included in this table are machine-learning evolutionary states based on $\langle \Delta \nu' \rangle$ and $\langle \nu'_{\max} \rangle$, as well as evolutionary states based on individual pipeline values, which are taken to be $\Delta \nu'$ and $\nu'_{\max}$.[6] We also include the EPIC IDs for stars that had no measured asteroseismic parameters by any pipeline but that were targeted as part of K2 GAP so that users may investigate asteroseismic selection functions as needed; we quantify K2 GAP DR3 completeness as a function of mass and radius in §4.1. The K2 GAP DR3 sample that we refer to in what follows is a subset of the totality of targeted stars, and consists only of the stars with a valid $\langle \nu'_{\max} \rangle$. There are 19417 such stars, 18821 of which also have a valid $\langle \Delta \nu' \rangle$ and therefore $\langle \kappa_R \rangle$ and $\langle \kappa_M \rangle$. Stars with both $\langle \nu'_{\max} \rangle$ and $\langle \Delta \nu' \rangle$ are assigned an evolutionary state, resulting in 12978 RGB stars and 5843 RC stars. The numbers of stars with asteroseismic detections broken down by campaign and pipeline are listed in Table 7. The Kiel diagram for the K2 GAP DR3 sample is shown in Figure 2 and its distribution on the sky is shown in Figure 1; the sample is also shown in Galactocentric coordinates in Fig. 3.

4. VALIDATION OF ASTEROSEISMIC VALUES IN K2 GAP DR3

4.1. Injection tests

In the previous section, we detailed the dependence of asteroseismic results across pipelines. However, there are likely additional systematics due to the length of the K2 light curves compared to, e.g., Kepler light curves. Indeed, Hekker et al. (2012) revealed non-negligible variations in completeness, precision, and accuracy in red giant asteroseismic parameters due to the length of the time series (i.e., the time baseline). In order to test the completeness, precision, and accuracy of the different asteroseismic modelling pipelines for K2-like data, we generated synthetic data for which we knew the "true" $\nu_{\max}$ and $\Delta \nu$ from Kepler and performed blind injection recovery tests.

---

[5] Since A2Z $\Delta \nu$ values do not contribute to $\langle \Delta \nu' \rangle$, there are no $\Delta \nu'_{A2Z}$ values populated in Table 2, and the $\kappa_{R,A2Z}$ and $\kappa_{M,A2Z}$ values in Table 4 are calculated using the raw $\Delta \nu$ and re-scaled $\nu'_{\max}$ values.

[6] The A2Z evolutionary states are based on raw $\Delta \nu$ and re-scaled $\nu'_{\max}$. Also, in the small number of cases where there were multiple observations of the same star across different campaigns, we adopted the evolutionary state from the campaign with the smallest evolutionary state uncertainty according to the machine learning approach.

We first created a grid in magnitude-$\nu_{\max}$ space from the distribution of Kepler stars from APOKASC (Pinsonneault et al. 2018); the faint giant sample of Mathur et al. (2016); and the M-giant sample of Stello et al. (2014), in order to select Kepler stars evenly across this parameter space. From each bin, when possible, we generated K2-like light curves based on 80d segments of Kepler light curves via two methods. First, we attempted to select from each bin three Kepler stars with at least five quarters of data each, from which we created 15 synthetic K2 light curves (selecting five different 80d sections from three stars). Second, we attempted to generate 15 synthetic K2 light curves from 15 different Kepler stars from a single 80d section of each of their light curves; in practice, not each bin had enough stars to create 30 synthetic K2 light curves from these two methods. Each of these synthetic K2 light curves was created using KASOC v1 Q1-Q14 light curves (Handberg & Lund 2014), linearly interpolating the Kepler flux onto a cadence of a star in K2 C3 to mimic the spectral window of actual C3 data and the frequency resolution of K2. We then increased the white noise level for each of the synthetic K2 light curves according to the following procedure. First, the white noise as a function of magnitude was computed for the entire grid of Kepler stars as well as the 10291 non-GAP C3 targets with EVEREST long-cadence light curves. The white noise for each star was computed by taking the standard deviation of its light curve filtered to remove variability slower than $\sim 150\mu$Hz. For both of these samples, the 20th percentile of the white noise levels as a function of magnitude were fitted using third degree polynomials. Each synthetic K2 light curve's white noise level was increased by the ratio of the Kepler-to-K2 white noise if that ratio was less than unity at the Kepler star's magnitude. In practice, this resulted in increasing the white noise level for stars fainter than $Kp = 14$, by on average 10% and by no more than 20%.

We show in Figure 4a the SNR of the synthetic sample.[7] We compute the SNR of the synthetic K2 data in a way that takes into account both the expected maximum mode amplitude and the granulation background level at $\nu_{\max}$. To do so, we adopt the approach from Campante et al. (2016), assuming 3 modes per order, ignoring observation integration time effects, and assuming a noise level according to the observed star-to-star white noise level at high frequencies in the spectra. For the mode maximum amplitude, we adopt the model $\mathcal{M}_{4,\beta}$ from Corsaro et al. (2013). The points are colored by

the provenance of the Kepler data, where there are potentially multiple synthetic stars per KIC ID because of the division of the Kepler light curves into 80d sections. In total, there are 57 synthetic stars from the M-giant catalogue (Stello et al. 2014); 891 synthetic stars from the faint giant catalogue (Mathur et al. 2016); and 1691 synthetic stars from the APOKASC catalogue (Pinsonneault et al. 2018). The dashed lines demarcate the boundaries of our grid used to draw the synthetic light curves in $\nu_{\max}$ space. We also show the distribution in magnitude space in Figure 4b, with vertical lines demarcating the magnitude bins used to populate the synthetic sample.

The pipelines' analysis of these synthetic K2 data proceeded blindly (i.e., the synthetic data were treated as real data), and the resulting asteroseismic parameters were processed using an iteration of the averaging procedure described in §3.2. The average results are denoted in the following figures as 'ALL', and any pipeline-specific results for synthetic K2 data are only shown if they pass the same muster as the real data (i.e., having at least two pipelines return results).

In Figure 5, we show the accuracy of the recovery for each of the asteroseismic pipelines, based on the ground-truth Kepler asteroseismic values. For this exercise, each pipeline analyzed the Kepler light curves to generate ground-truth labels. For the purposes of this plot and those that follow, uncertainties on the binned median are computed by inflating the standard uncertainty on the binned mean by a factor of $\sqrt{\frac{\pi}{2}}$ (Kenney & Keeping 1962).

We show the trends in the K2 asteroseismic values as a function of both $\nu_{\max}$ and $\Delta\nu$, and which are evident at the percent level as a function of $\nu_{\max}$ and $\Delta\nu$. There are also biases when averaged over all of $\nu_{\max}$ and $\Delta\nu$, which can be seen by the fact that the trends for some pipelines in Figure 5 are systematically offset below the one-to-one line. This suggests that there are non-negligible systematics in asteroseismic pipeline recovery that are a function of baseline, and which would result in too-small radii and masses compared to Kepler asteroseismology (see the below comparison between mass distributions in K2 and Kepler). Time baseline seems to have the smallest impact on $\Delta\nu$, since several pipelines report nearly identical $\Delta\nu$ with Kepler as with K2 data (though some pipelines show substantial disagreement). $\nu_{\max}$, however, suffers from significant biases based on the time baseline: excursions of a $2-3\%$ and zero-point biases of $1-2\%$ are observed. There are also indications that some pipelines may have SNR-dependent biases, which manifest as trends in the fractional agreement between Kepler and synthetic K2 values as a function of SNR

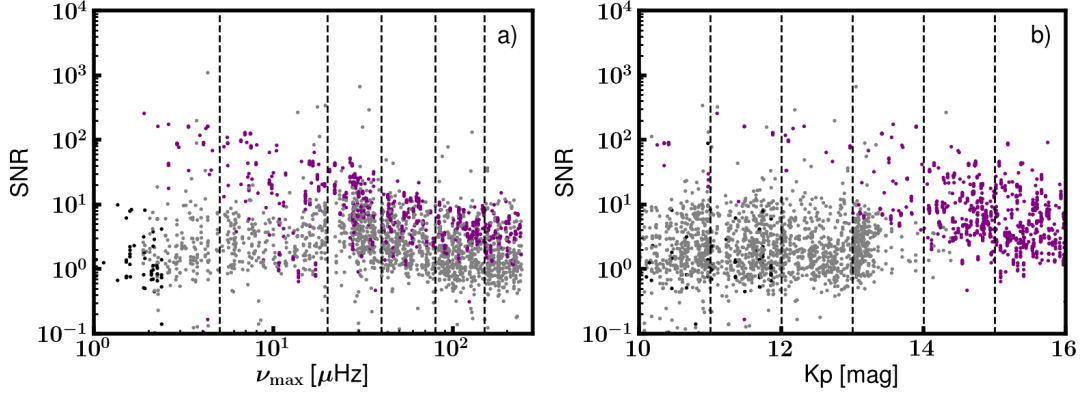[7] Note that this is the SNR in power, not amplitude.

Figure 4. Distribution of the expected signal-to-noise ratio (SNR) for synthetic K2 stars as a function of the Kepler $\nu_{\max}$ (a) and Kepler magnitude (b). Synthetic stars are colored according to their provenance: Pinsonneault et al. (2018) (grey); Mathur et al. (2016) (purple); or Stello et al. (2014) (black). The synthetic population was drawn from a range of SNR and $\nu_{\max}$ in order to test the accuracy and precision of the asteroseismic pipelines in K2 GAP DR3.

in Figure 6. Note that the SNR shown in this figure is not the same SNR as shown in Figure 4a: the SNR in Figure 6 represents the relative SNR at fixed $\nu_{\max}$, and is computed by dividing out the median trend from Figure 4a.

Although we will be calibrating our K2 data based on independent estimates of radius in §4, these biases are important to note, and are being investigated in the context of TESS (Stello et al. 2021). It should also be noted that there could be additional biases introduced in asteroseismic analysis based on the preparation of the pixel-level data and the details of processing the light curves into power spectra (e.g., choices in frequency filter). Based on internal consistency checks against K2SFF light curves (Vanderburg & Johnson 2014), such effects are smaller than time baseline biases shown here ($< 1\%$).

Apart from testing the $\nu_{\max}$-, $\Delta\nu$- SNR- and time baseline–dependent biases in pipeline results, we can also test the internal consistency of the uncertainties using the synthetic K2 data. Since we have results from precise Kepler data, we can compare it to the less precise, simulated K2 data for the same stars, and evaluate if pipeline results are internally consistent to within their reported uncertainties. To do so, the observed distribution of the fractional deviation between the K2 and the Kepler measurements ('true' in Fig. 7) is compared to the expected distribution ('reported' in Figure 7), created by drawing Gaussian random variables assuming the reported K2 uncertainty for each simulated K2 star. If the reported uncertainties were self-consistent, then the two distributions would be identical. If the pipeline tends to over-estimate uncertainties, the 'reported' distribution would be skewed toward higher uncertainties compared to the 'true' distribution, and vice versa. The

internal consistency is globally good for most pipelines. This plot also indicates the relative precision of the pipelines, with the dashed line indicating $\sigma_{\Delta\nu} = 0.01$ and $\sigma_{\nu_{\max}} = 0.03$, which are representative values for the internal uncertainties for the pipelines. For $\Delta\nu$, there is perhaps a tendency that the pipelines that provide results for fewer stars (and hence maybe are more strict in accepting which measurements are valid) show smaller deviations between 'true' and 'reported' values. By the same token, the more values a pipeline accepts as valid, the more results deviating strongly from the truth are reported.

The above exercise tests the internal consistency of the uncertainties reported by each pipeline, but, by comparing the reported uncertainties to the scatter in the pipeline values for each star, $\sigma_{\langle\nu'_{\max}\rangle}$ and $\sigma_{\langle\Delta\nu'\rangle}$ described in §3, we can better establish the accuracy of the pipeline uncertainties. Indeed, even if a pipeline consistently assigns uncertainties to their parameters, it does not necessarily correspond to the true uncertainty — i.e., including systematic uncertainties — in the physical parameter: each pipeline's methodology is on its own system and measures $\nu_{\max}$ and $\Delta\nu$ in slightly different ways. This can be seen to the extent that the scaling factors for each pipeline, $X_{\nu_{\max}}$ and $X_{\Delta\nu}$, differ from unity, indicating that the pipelines measure asteroseismic values on scales that differ by up to 1%. Even after correction to the mean scale, the top panels of Figures 8-11 show that there are residual fractional deviations between re-scaled pipeline values and the mean values across pipelines, $\nu'_{\max}$ and $\langle\nu'_{\max}\rangle$ as a function of $\nu_{\max}$ and $\Delta\nu$. By adopting the scatter across pipelines in asteroseismic values as our uncertainties in K2 GAP DR3, we take into account the uncertainties due to these differences in pipeline methodologies. We show compar-
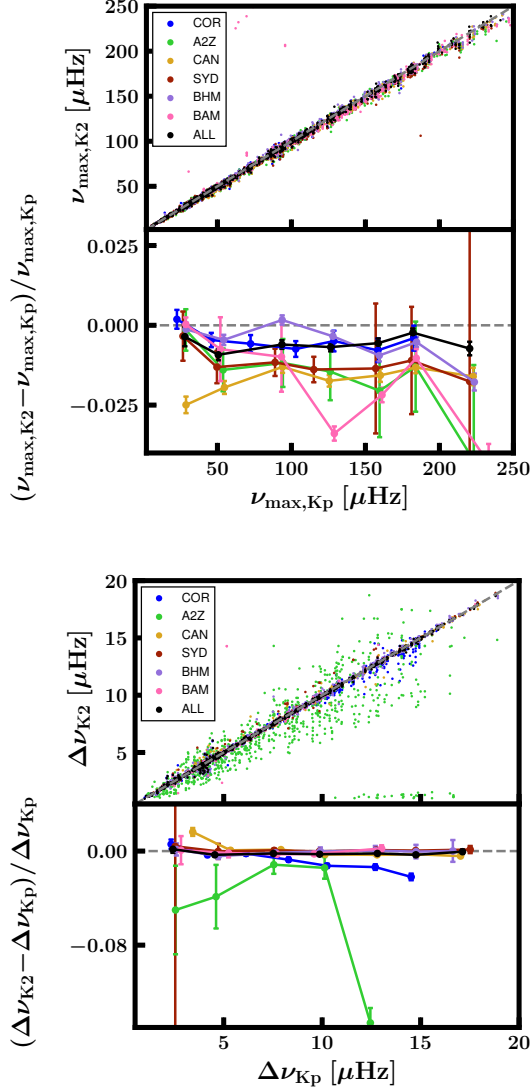
Figure 5. Binned medians and uncertainties on the median of the fractional difference between Kepler and synthetic K2 ν_{max} (top) & $\Delta\nu$ (bottom) values for each pipeline contributing results to K2 GAP DR3, according to the legend. Deviations from the dashed line indicate that the pipeline returns K2 values that are on a different scale than the pipeline's Kepler results (labelled as $\nu_{\mathrm{max,K2}}$ & $\nu_{\mathrm{max,Kp}}$ [top] and $\Delta\nu_{\mathrm{K2}}$ & $\Delta\nu_{\mathrm{Kp}}$ [bottom], respectively).

isons between the internal uncertainties for each pipeline and the K2 GAP DR3 uncertainties in the right panels of Figures 8-11. The region above (below) the dotted lines is a regime of where the pipeline-reported uncertainties are larger (smaller) than the K2 GAP DR3 adopted uncertainties. As found in DR2, the pipelines often agree on $\Delta\nu$ and ν_{max} better than would be expected from their internal uncertainties.

The uncertainties $\sigma_{\langle\nu'_{\mathrm{max}}\rangle}$ and $\sigma_{\langle\Delta\nu'\rangle}$ do not explicitly take into account the reported measurement/statistical
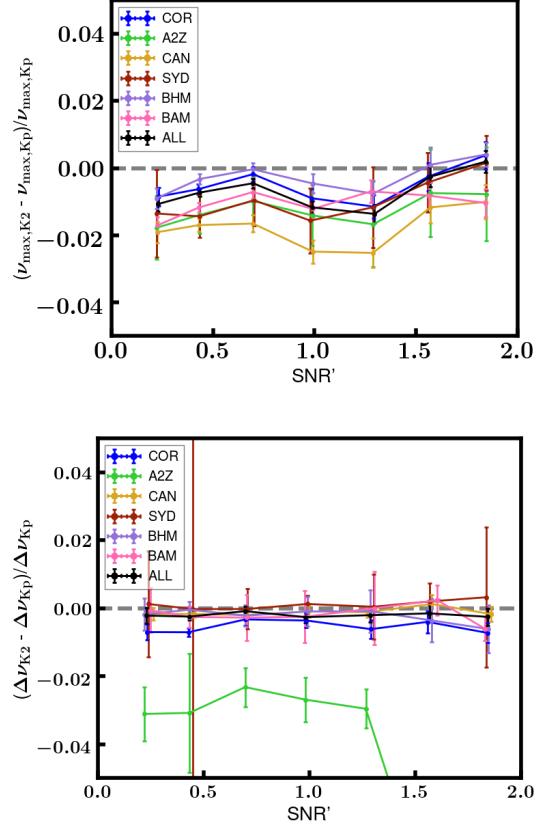

Figure 6. Fractional difference between Kepler and synthetic K2 values, for each pipeline according to the legend, as a function of the synthetic K2 signal-to-noise ratio (SNR). The differences are shown as binned medians and uncertainties on the medians. Trends as a function of SNR would indicate a pipeline's asteroseismic values are noise-dependent.

uncertainties of the pipelines, but, by virtue of $\sigma_{\langle\nu'_{\mathrm{max}}\rangle}$ and $\sigma_{\langle\Delta\nu'\rangle}$ being defined based on the pipeline-to-pipeline scatter, they capture both systematic uncertainties in the pipeline methods and statistical measurement uncertainties: large bias in the pipeline results will tend to increase the pipeline-to-pipeline scatter, as would large measurement uncertainty. Even if we assume the reported pipeline measurement uncertainties represent the true uncertainties, which is to varying degrees an inaccurate assumption (cf., Fig. 7), it is not clear how the statistical uncertainties in the pipeline measurements should be combined to yield a purely statistical uncertainty in $\langle\nu'_{\mathrm{max}}\rangle$ and $\langle\Delta\nu'\rangle$, which are averages of the pipeline measurements. This is because the pipelines will have some degree of correlation in their measurements owing to all the pipelines analyzing the same power spectrum for a given star (i.e., there is only one realization of the data). In order to estimate a purely statistical uncertainty on $\langle\nu'_{\mathrm{max}}\rangle$ and $\langle\Delta\nu'\rangle$, we conservatively assume that all the pipeline

measurements are completely correlated, and compute uncertainties on $\langle \nu'_{\max} \rangle$ and $\langle \Delta\nu' \rangle$, which we report in Table 2 as $\varsigma_{\langle \nu'_{\max} \rangle}$ and $\varsigma_{\langle \Delta\nu' \rangle}$. These latter uncertainties are larger than our adopted empirical uncertainties in this work, $\sigma_{\langle \nu'_{\max} \rangle}$ and $\sigma_{\langle \Delta\nu' \rangle}$, by factors of ~ 2.2 and ~ 1.5, respectively. Assuming a correlation of 0.1 among all pipelines reduces the differences to ~ 1.2 and 0.95. Because the reported pipeline uncertainties are to varying degrees unreliable (Fig. 7) and because of the unknown correlation among different pipeline measurements, these uncertainties are not used in this analysis, but are rather provided as a conservative indication of a purely statistical uncertainty compared to our adopted empirical uncertainties, $\sigma_{\langle \nu'_{\max} \rangle}$ and $\sigma_{\langle \Delta\nu' \rangle}$.

We next estimate the completeness of each pipeline's results by comparing the number of recovered stars to the total number of synthetic stars. The completeness fraction, where 1.0 indicates a perfect recovery rate, is shown as a function of $\nu_{\max}$, $\Delta\nu$, radius, and mass in Figures 12-15. The synthetic sample was created with a range of SNRs, and with magnitude-dependent noise consistent with K2 data, but the distribution of the synthetic sample is not, in detail, representative of the K2 GAP DR3 sample. For this reason, the completeness curves plotted in Figures 12-15 are indicative but not determinative of the completeness of the respective parameters in K2 GAP DR3. Note also that the completeness is defined with respect to Kepler results, so this completeness is, strictly speaking, an estimate of the completeness of recovering K2 data with respect to Kepler and not necessarily an absolute completeness estimate, which must await a future analysis using Gaia as a reference (e.g., following the Kepler observation completeness analysis from Wolniewicz et al. 2021).

We see that the completeness curves are peaked in the middle of parameter space for $\nu_{\max}$ and $\Delta\nu$, with lower completeness at high and low values of $\nu_{\max}$ and $\Delta\nu$. This is understood to be related to the frequency resolution: both $\Delta\nu$ and $\nu_{\max}$ detection is limited on the lower end by the time baseline, and on the upper end by the sampling rate of the K2 observations. It is even more difficult to recover $\nu_{\max}$ and $\Delta\nu$ at low values because of another effect: there are fewer modes that are excited at low $\nu_{\max}$, and they can be difficult to distinguish from noise, especially at the frequency resolution of K2. This latter effect is the reason why there is a marked decrease in completeness for $\nu_{\max} \lesssim 10\mu$Hz. This incompleteness has been noted in previous data releases (Stello et al. 2017; Zinn et al. 2020) but we are able to robustly quantify it here for the first time: although it varies by pipeline, at least $\approx 20\%$ of stars with $\nu_{\max} \lesssim 10\mu$Hz are not detected.

The completeness fractions in radius and mass space are not one-to-one mappings from $\nu_{\max}$ and $\Delta\nu$, since, for a given surface gravity ($\nu_{\max}$), there is a spread in mass ($\Delta\nu$). For this reason, we consider the radius and mass completeness curves separately from the $\nu_{\max}$ and $\Delta\nu$ cases. The completeness in radius suffers from a drop-off in recovery with increasing radius, due to incompleteness in $\nu_{\max}$ and $\Delta\nu$ at lower frequencies. Given the lack of a strong correlation between radius and age on the giant branch (since the majority of a red giant's lifetime is spent on the main sequence as opposed to climbing the giant branch), the drop-off in recovery with increasing radius does not require a selection function correction in age space, but does have implications for a selection function correction as a function of distance. The completeness curves are much less peaked in mass space. This is of particular interest for Galactic archaeology applications of K2 GAP DR3: were completeness a strong function of mass, it would require special treatment in the selection function. There is a tendency for low-mass stars to be under-represented among some pipelines, for $M \lesssim 1.2 M_\odot$. This may be relevant for detailed studies since this will map onto an under-representation of older stars. Regarding the completeness of the underlying K2 GAP sample itself, typically 97% of the proposed targets in any given campaign were observed, with the targets following simple color-magnitude cuts (S. Sharma, in prep.).

Figure 16a is indicative of the mass distribution for those stars in the K2 GAP DR3 sample with both $\langle \nu'_{\max} \rangle$ and $\langle \Delta\nu' \rangle$, where the ordinate is an asteroseismic proxy for mass proposed by Huber et al. (2010) that scales like $M^{0.25}$, given the asteroseismic scaling relations (Eqs. 3 & 4). For reference, Figure 16b shows the Kepler sample from Yu et al. (2018). Comparing the Kepler and K2 samples, we find a good correspondence, with a couple of differences worth noting. First, the right edge of the clump is better defined in Kepler data by having better precision and more high-mass secondary red clump stars. The Kepler sample also extends to higher frequencies than does K2 GAP DR3, presumably due to better noise properties in Kepler compared to K2. However, K2 has double the fraction of low-frequency ($< 20\mu$Hz) oscillators than does Kepler, in spite of the tendency to not recover stars in this frequency regime with K2-like time baselines (Fig. 12). Note that the overall shift in mass between the Yu et al. (2018) and K2 GAP DR3 samples is consistent with the time baseline systematics in $\nu_{\max}$ (Fig. 5), such that the SYD Kepler $\nu_{\max}$ values would be expected to be larger by $\sim 1\%$ than K2 $\nu_{\max}$ values.
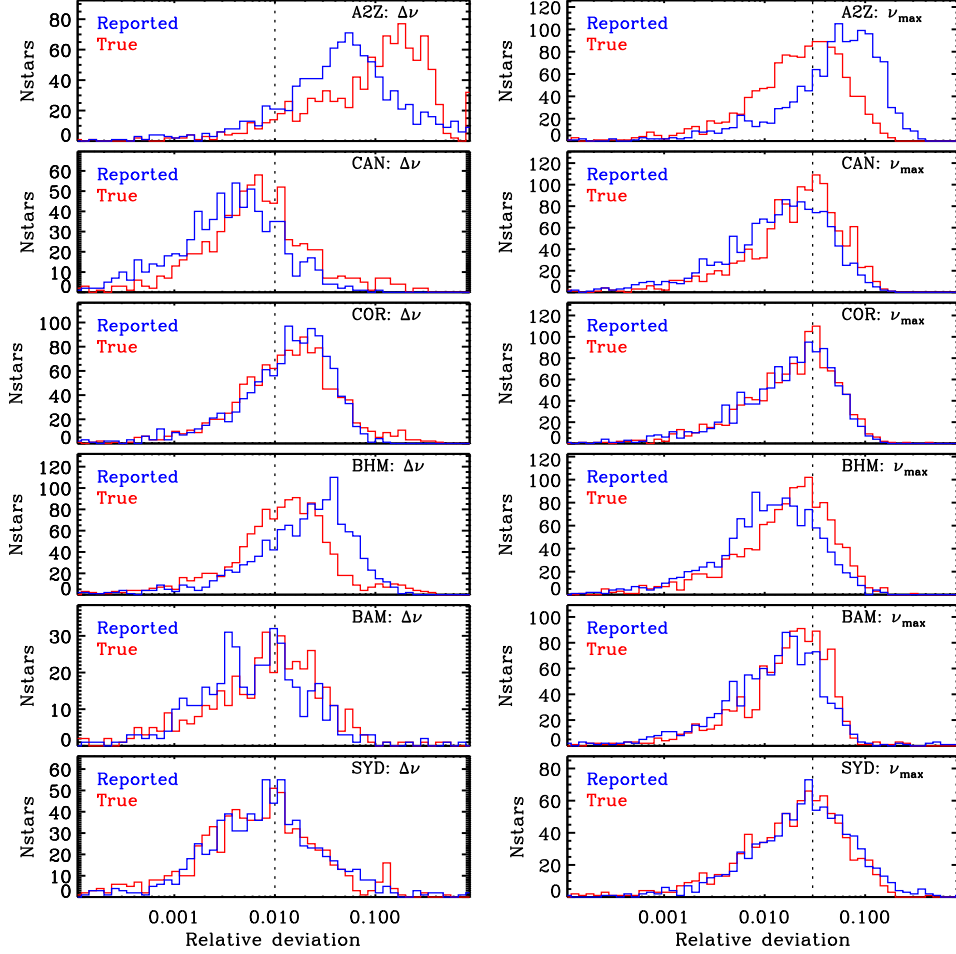
Figure 7. Reported pipeline fractional uncertainty distributions on K2 asteroseismic values ('reported') and the inferred fractional uncertainty distributions by comparing Kepler and K2 values ('true'). The dashed lines are shown for reference, and correspond to fractional uncertainties of 1% for $\Delta\nu$ and 3% for ν_{max}.

As with Figure 16a, Figure 17 shows the K2 GAP DR3 stars in the mass proxy v. ν_{max} space, but for each pipeline and separately for raw pipeline results (ν_{max}, $\Delta\nu$; left panels) and re-scaled pipeline values (ν'_{max}, $\Delta\nu'$; right panels). The structures of the distributions in this space are generally similar across pipelines, though there are differences in detail. For instance, we see that there are some pipeline-dependent differences in the recovery of low-mass red clump stars and the recovery of low-frequency stars. There are also differences between the raw and re-scaled values, the most salient of which are that 1) raw values have more scatter in the ordinate (due to requiring more than one pipeline returning results to define the re-scaled values, which will tend to select stars with more precise asteroseimsic values) and 2) there tend to be fewer low-frequency and high-frequency re-scaled values (a selection effect of it being less likely for multiple pipelines to return values for stars affected by K2's white noise and time baseline). The diagonal ridge on the left side of the red clump distribution is

due to requiring that stars with $\Delta\nu < 3.2$ be assigned a red giant branch evolutionary state (see §3.2). However, we see that this choice does not cut out true red clump stars, which are found in the locus where the density of the blue points saturates.

4.2. *Asteroseismic calibration with Gaia*

In §3, we indicated that it is important to use appropriate solar reference values, according to the asteroseismic pipeline being used. The K2 GAP DR3 values are averages across pipelines, so the question arises as to what solar reference value scale is appropriate. One proposal would be to adopt the solar reference values from APOKASC-2 (Pinsonneault et al. 2018), $\nu_{\mathrm{max},\odot} = 3076\mu\mathrm{Hz}$ and $\Delta\nu_\odot = 135.146\mu\mathrm{Hz}$, given that APOKASC-2 values are also averages across pipelines. Although we follow a very similar methodology to place the pipeline values on a common scale, it differs in some regards (e.g., sigma-clipping and not weighting pipeline values by uncertainties during the averaging process).
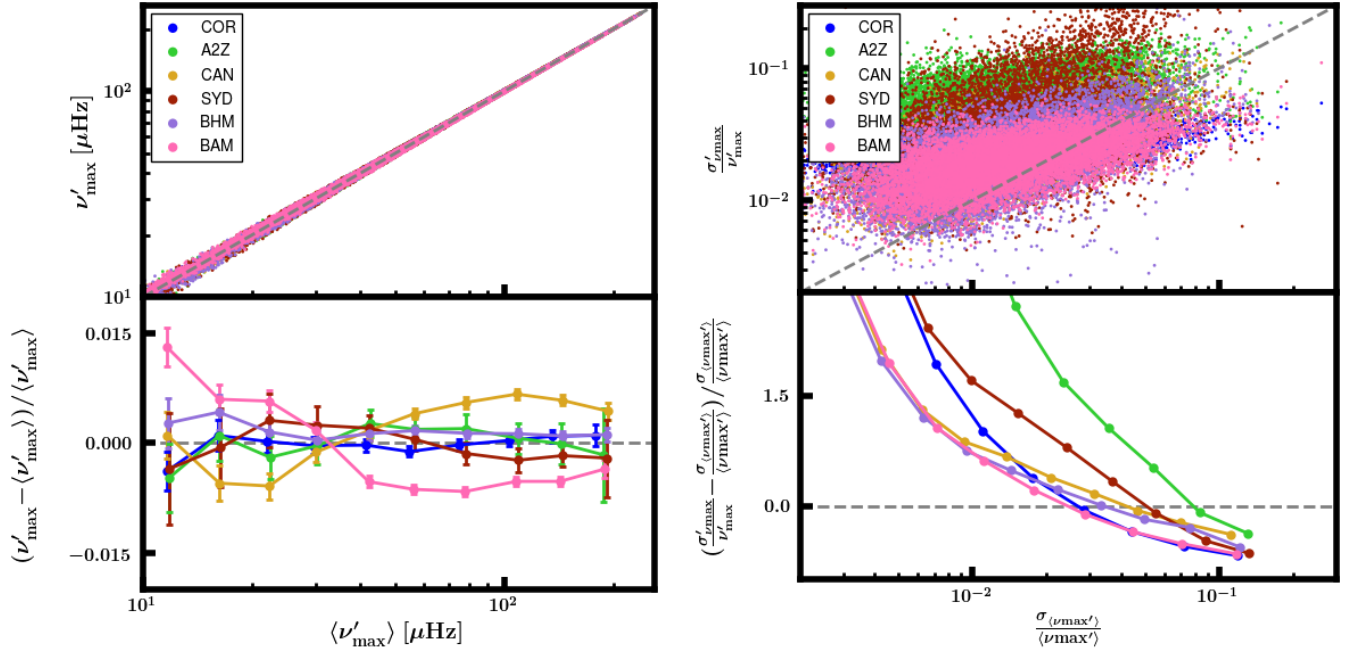
Figure 8. Left: comparison of RGB $\nu_{\max}$ among pipelines, showing the re-scaled $\nu'_{\max}$ from each pipeline versus the mean $\langle \nu'_{\max} \rangle$ across pipelines in the top panel, and the fractional difference between $\langle \nu'_{\max} \rangle$ and $\nu'_{\max}$ in the bottom panel, with error bars showing binned errors on the median fractional difference, assuming the uncertainty on $\langle \nu'_{\max} \rangle$ to be the standard deviation among the re-scaled pipeline $\nu'_{\max}$ values, $\sigma_{\langle \nu'_{\max} \rangle}$. Right: the fractional scatter across $\nu'_{\max}$ for a given star with multiple pipeline values is plotted against the reported fractional uncertainty on $\nu'_{\max}$ for each pipeline. The fractional difference between the two fractional uncertainties is shown in the bottom panel.
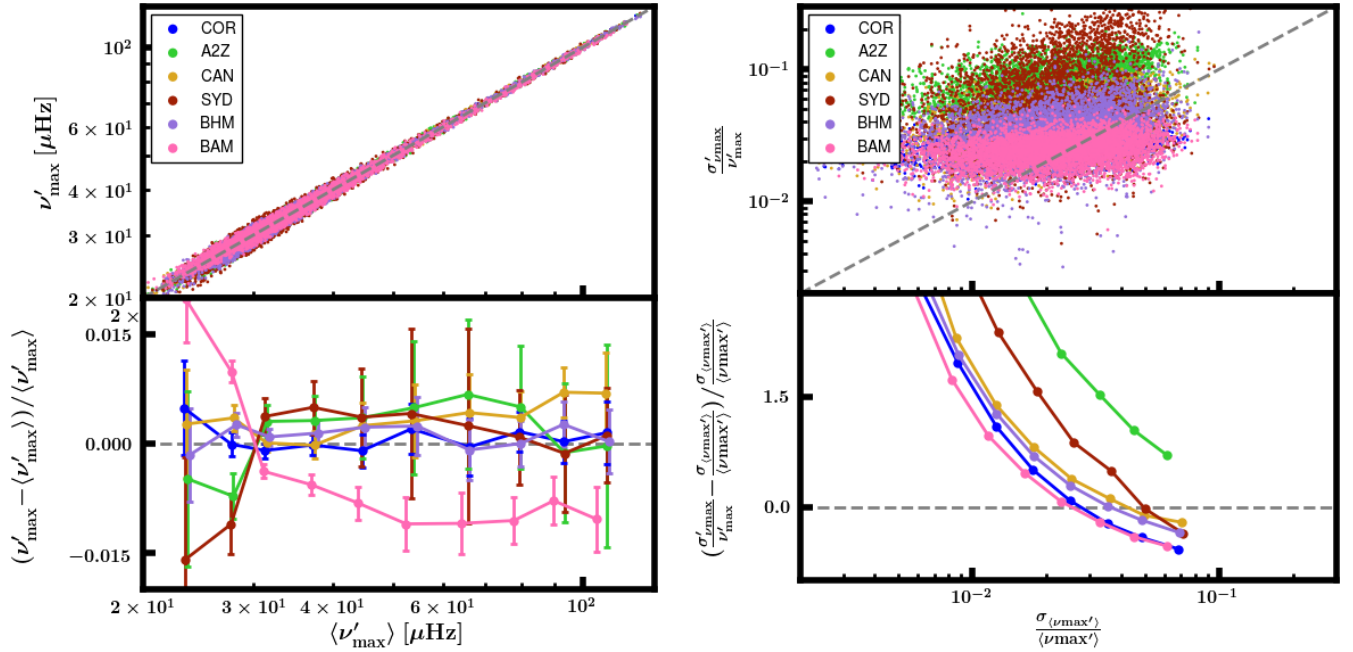
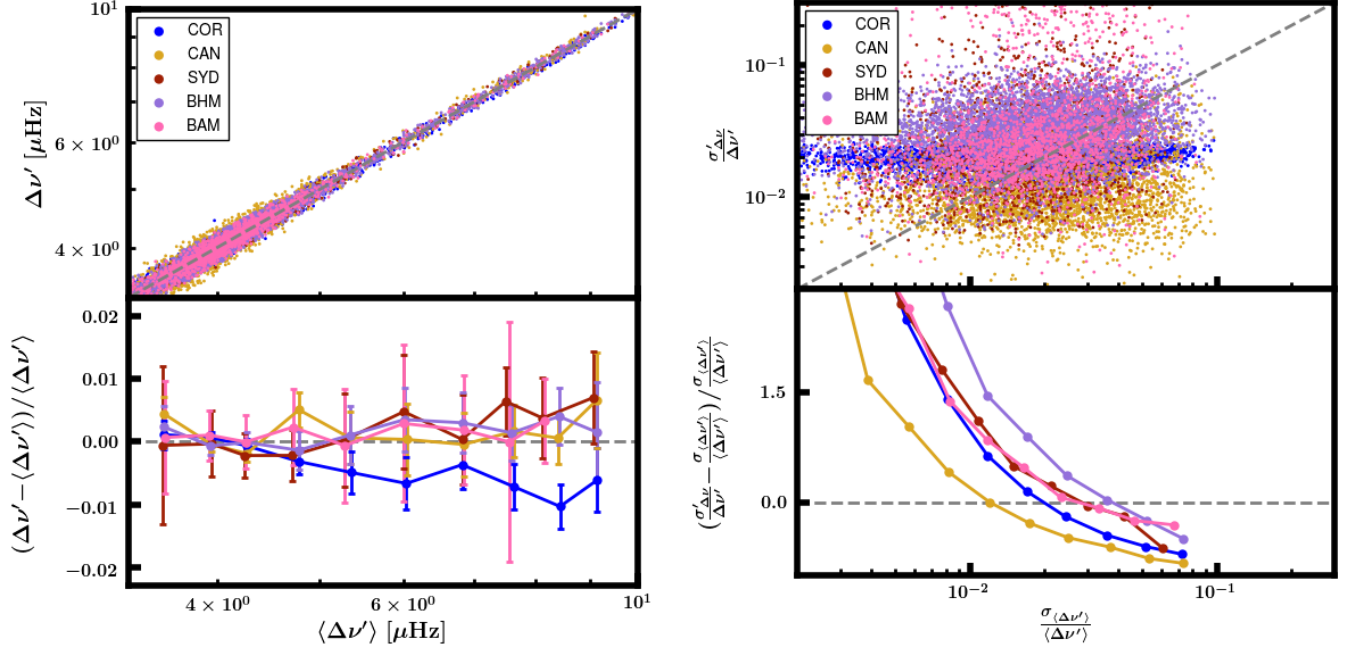**Figure 9.** Same as Figure 8, but for RC stars.
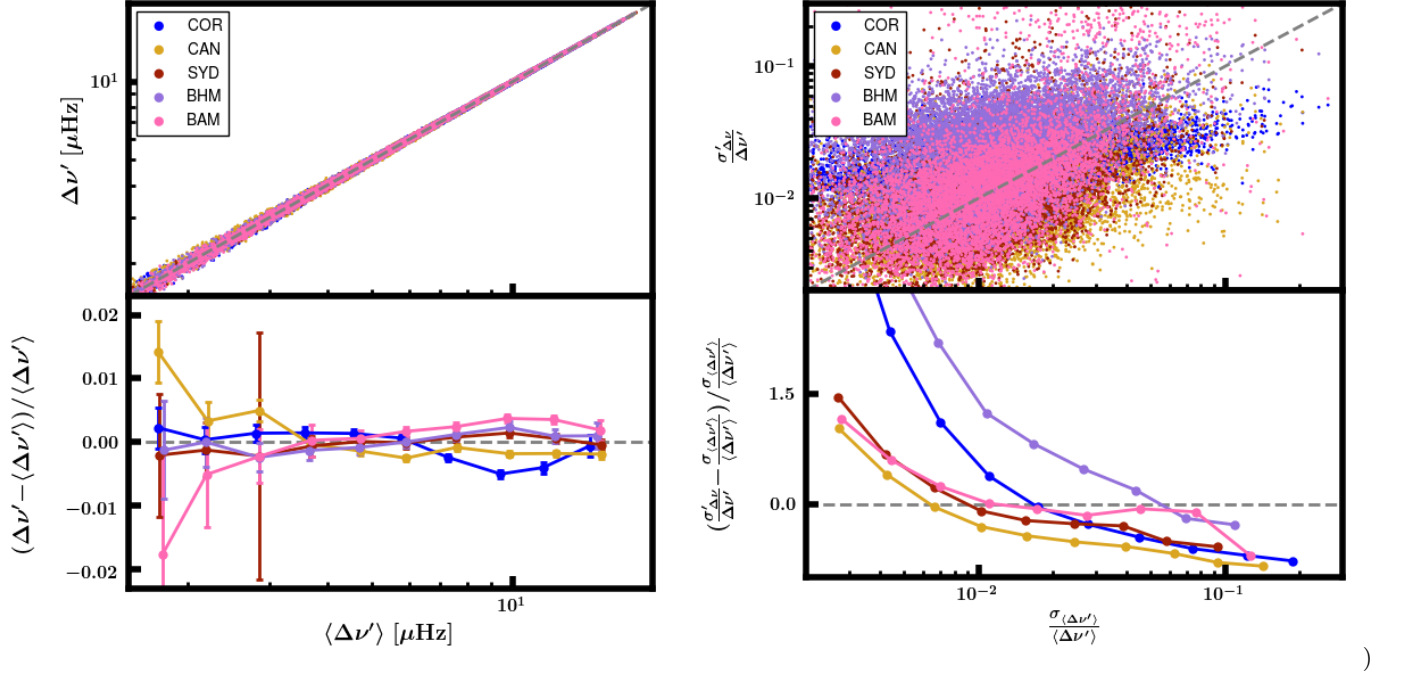
Figure 10. Same as Figure 8, but for $\Delta\nu$.

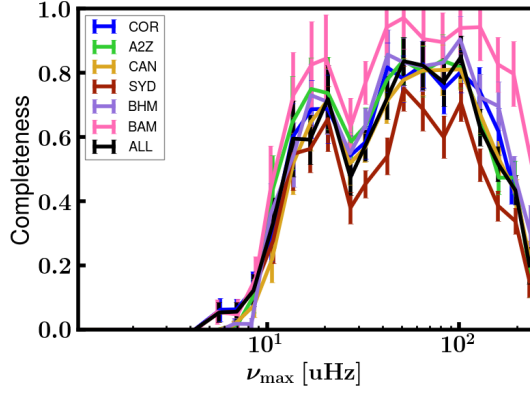**Figure 11.** Same as Figure 10, but for RC stars.

Figure 12. The recovery rate as a function of $\nu_{\max}$ for the pipelines contributing to K2 GAP DR3. A completeness of 1 would indicate that the pipelines recover all of the injected synthetic K2 stars generated from Kepler data, and gives confidence that the pipeline is recovering all the detectable stars in real K2 data.
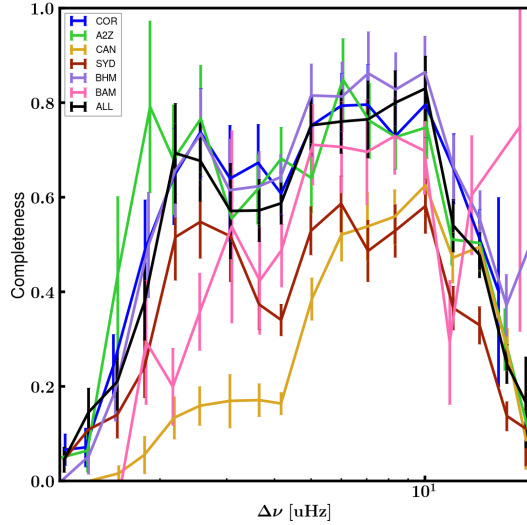

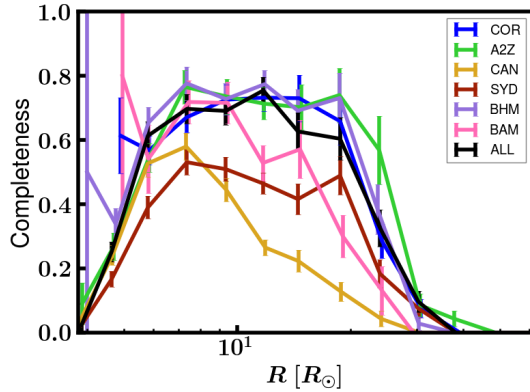**Figure 13.** The same as Figure 12, but for $\Delta\nu$.

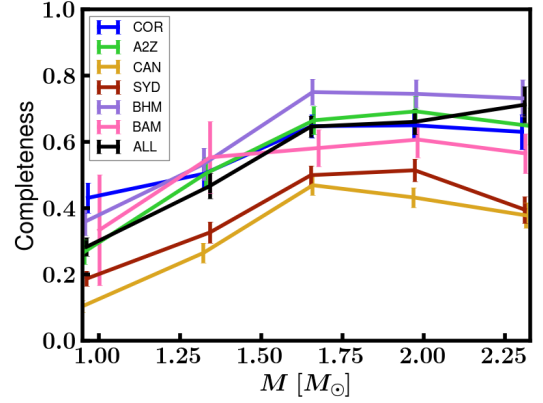**Figure 14.** The same as Figure 12, but for radius.

Figure 15. The same as Figure 12, but for mass.

As well, we include results from BAM, which was not a pipeline considered in Pinsonneault et al. (2018). For this reason, we cannot assume that $\langle\nu'_{\max}\rangle$ and $\langle\Delta\nu'\rangle$ are on the same scale as defined by Pinsonneault et al. (2018) just because we use the solar reference values from the cluster calibration procedure in Pinsonneault et al. (2018). It is also possible that the difference in Kepler versus K2 observation duration results in systematically different parameter measurements (see §4.1).

With this in mind, in what follows, we calibrate the K2 GAP DR3 $\langle\nu'_{\max}\rangle$ values using a non-unity, scalar $f_{\nu_{\max}}$ (§3), or, equivalently, by re-scaling the APOKASC-2 $\nu_{\max,\odot}$ value. Our Gaia calibration sample is the subset of stars in the K2 GAP DR3 sample with $\langle\nu'_{\max}\rangle$ and $\langle\Delta\nu'\rangle$ that have APOGEE DR16 (Ahumada et al. 2020) temperatures & metallicities and Gaia parallaxes & proper motions from *Gaia* Data Release 2 (Gaia Collaboration et al. 2018; Lindegren et al. 2018).

With the known zero-point offset in Gaia parallax (e.g., Lindegren et al. 2018; Khan et al. 2019; Zinn et al. 2019a) in mind, we appeal to the methodology described in Schönrich et al. (2019), which infers distances in Gaia-based bulk stellar motions. This method can be sensitive to knowing the selection function of the stellar population, and so we take care to model the selection function of GAP targets according to Schönrich & Aumer (2017). The resulting parallax zero-points show a scatter of $\sim 10\mu$as across the campaigns, comparable to the positional variation found by Chan & Bovy (2020) and Khan et al. (2019).

We perform the calibration using a subset of the Gaia-APOGEE-K2 overlap, knowing that there are certain known systematics that could bias the calibration. First, we limit the impact of parallax zero-point by only working with stars with raw Gaia parallaxes of $\pi > 0.4$mas, parallax uncertainties less than 10%, and Gaia G-band magnitude < 13mag, out of an abundance of caution, in
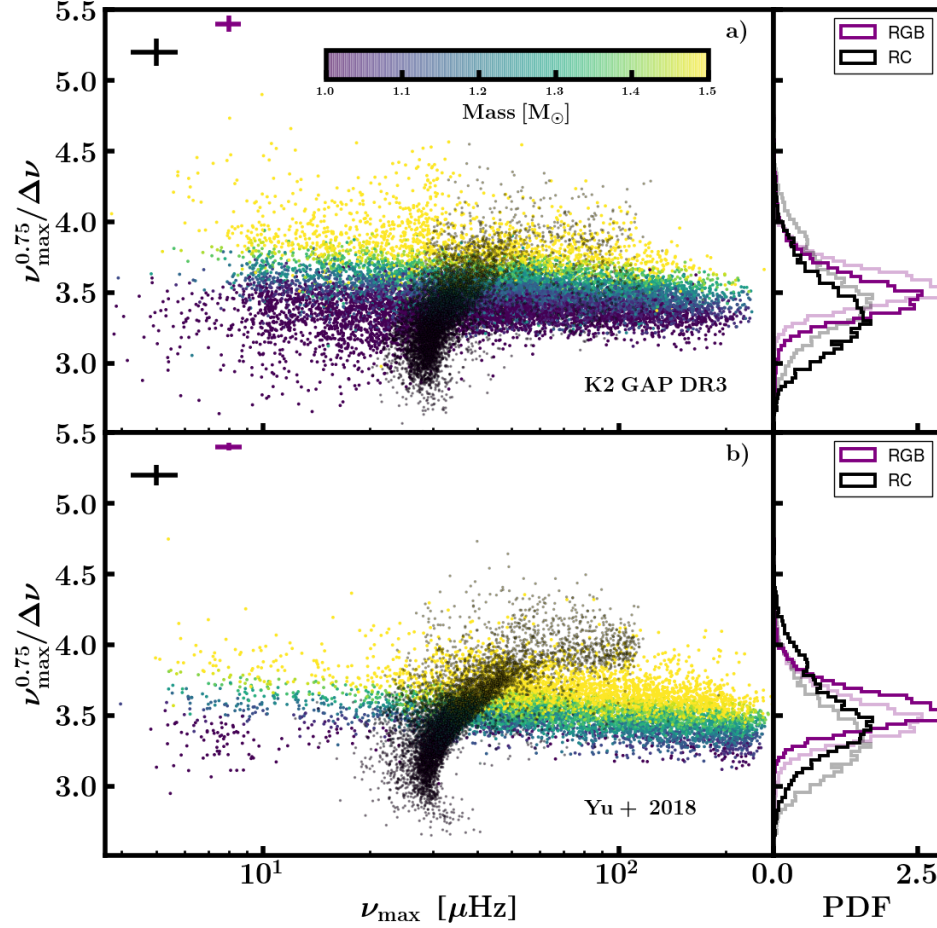
Figure 16. Asteroseismic mass diagram for K2 GAP DR3 (a) and the Yu et al. (2018) Kepler sample (b), where the ordinate is a proxy for mass. Stars are colored by their asteroseismic mass, which is computed according to Equation 8, using EPIC temperatures. Red clump stars are indicated by black symbols. Stars are classified as first-ascent red giant or not based on a machine-learning approach (see §3.2). Typical uncertainties for red giant branch stars and red clump stars are indicated by the purple and black error bars. The probability density functions (PDFs) of red giant branch and red clump mass proxies are shown on the panels on the right, where the lighter curves in each panel show the bold curves from the other panel, for comparison.

light of indications of parallax- and magnitude dependent offsets (Schönrich et al. 2019; Zinn et al. 2019a). We also reject metal-poor stars ([Fe/H] < -1) from subsequent analysis, since there are indications that asteroseismic scaling relation systematics could exist in the metal-poor regime (Epstein et al. 2014; Zinn et al. 2019b; though see Kallinger et al. 2018). We further reject stars that are highly evolved ($R > 30R_\odot$), in order to avoid potential systematics in the asteroseismic scale in the luminous regime (Mosser et al. 2013; Stello et al. 2014; Kallinger et al. 2018; Zinn et al. 2019b). Finally, we reject from consideration 12 RGB and 2 RC stars that have asteroseismic and Gaia radius disagreement by more than 3σ, leaving 841 RGB and 214 RC stars for calibration. Since this sample has APOGEE spectroscopic abundances, we also modify the $f_{\Delta\nu}$ for our calibration

sample by adjusting the metallicity that goes into computing $f_{\Delta\nu}$ to account for non-solar α abundances according to the Salaris et al. (1993) prescription.

The Gaia radii are computed following the procedure from Zinn et al. (2017), wherein a bolometric flux, Gaia parallax, and APOGEE effective temperature are combined using the Stefan-Boltzmann law. We use a $K_{\rm s}$-band bolometric correction (González Hernández & Bonifacio 2009) to minimize extinction effects, and employ the three-dimensional dust map of Green et al. (2015), as implemented in `mwdust`[8] (Bovy et al. 2016).

We see in Figure 18 similar trends as we did in K2 GAP DR2 (Zinn et al. 2020): there is an over-estimation

_____
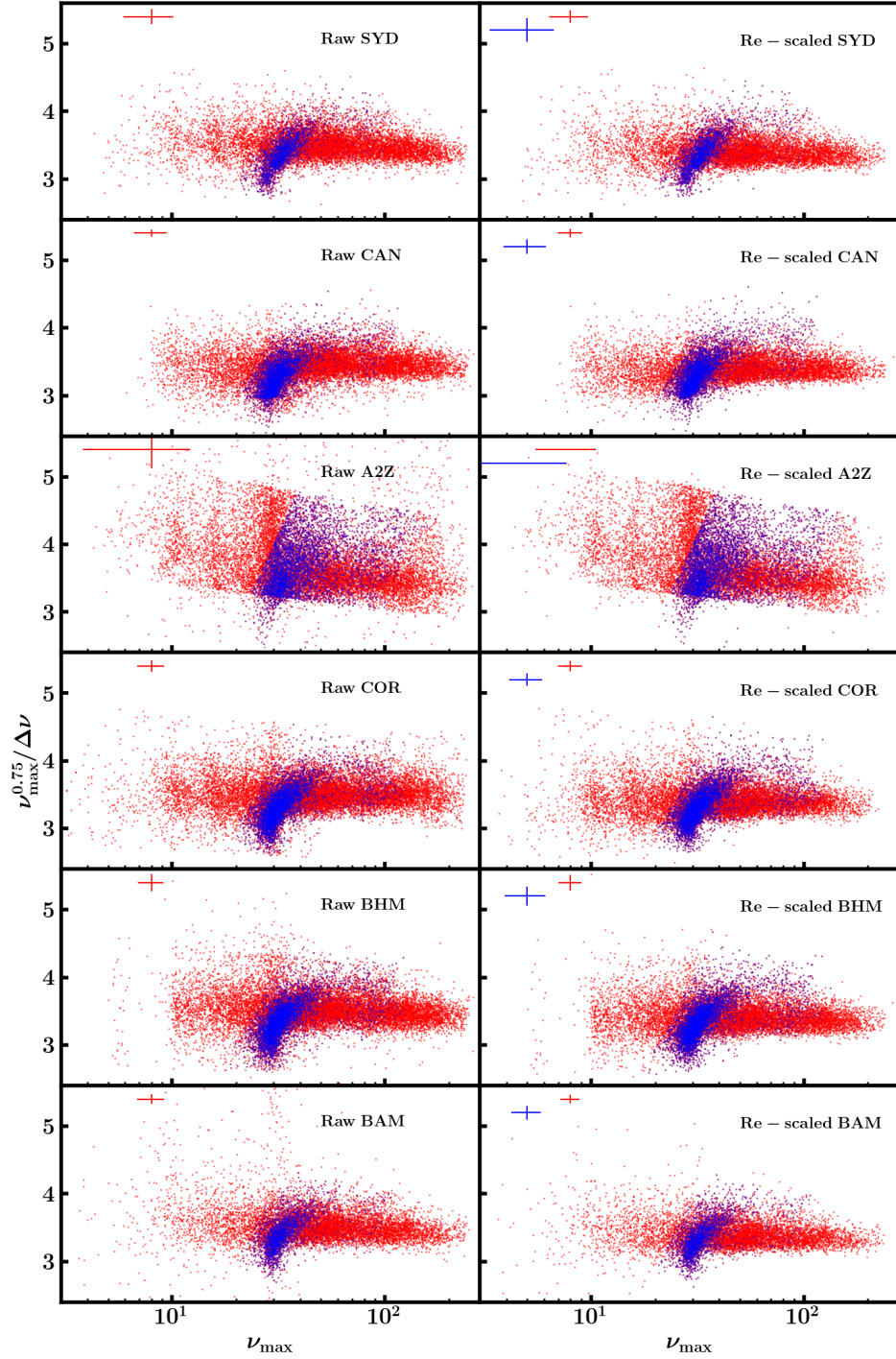[8] https://github.com/jobovy/mwdust

Figure 17. Asteroseismic mass diagram for each pipeline, where the ordinate is a proxy for mass. Red giant branch stars are shown as red points, and red clump stars are shown as blue points. The left column shows the raw pipeline-specific values ($\Delta\nu$, ν_{max}) and the right column shows the re-scaled pipeline-specific values ($\Delta\nu'$, ν'_{max}), which are only given for stars with results from at least two pipelines (see §3.2). Stars are classified as first-ascent red giant or not based on a machine-learning approach using pipeline-specific asteroseismic values (see §3.2). Typical uncertainties for RGB and RC stars are indicated by the red and blue error bars.

in the asteroseismic radii compared to Gaia at and below $R \approx 8 R_\odot$ among red giant branch stars.

The strong trend in radius agreement for the RC is of astrophysical interest, particularly given constraints on mass-loss (e.g., Miglio et al. 2012; Kallinger et al. 2018) that rely on the accuracy of asteroseismic scaling relations for the RC. However, as we noted in Zinn et al. 2020, the trend seems to be mostly a function of $\Delta\nu$, and therefore may be related to inadequacies in the red clump stellar structure models that underpin theoretical $f_{\Delta\nu}$ calculations (An et al. 2019). It is beyond the scope of the present work to further examine the cause of the discrepancy, but developments in better understanding this behavior in the RC are in preparation.

We calibrate our K2 GAP DR3 asteroseismic values to be on the Gaia parallactic scale by adopting the following:

$$f_{\nu_{\max}} \equiv \langle R_{\mathrm{seis}}/R_{Gaia} \rangle = \frac{\sum \frac{R_{\mathrm{seis}}}{R_{Gaia}}/\sigma_R^2}{\sum 1/\sigma_R^2},$$

where $\sigma_R = \frac{R_{\mathrm{seis}}}{R_{Gaia}} \sqrt{\left(\frac{\sigma_{R,Gaia}}{R_{Gaia}}\right)^2 + \left(\frac{\sigma_{R,\mathrm{seis}}}{R_{\mathrm{seis}}}\right)^2}$. We do this separately for RGB and RC stars, finding $f_{\nu_{\max},\mathrm{RGB}} = 1.017 \pm 0.001$ and $f_{\nu_{\max},\mathrm{RC}} = 1.008 \pm 0.003$. This can be thought of as a re-scaling of the solar reference value, $\nu_{\max,\odot}$, though for convenience, we apply this correction directly to the $\langle\nu'_{\max}\rangle$, $\langle\kappa_R\rangle$, and $\langle\kappa_M\rangle$ values provided in Table 2, and thus when working with $\langle\nu'_{\max}\rangle$, the K2 GAP DR3 $\nu_{\max,\odot}$ value given in Table 1 should be used, which is the same as that from (Pinsonneault et al. 2018). Even after accounting for this $f_{\nu_{\max}}$, the uncertainty in the $f_{\nu_{\max}}$ becomes a systematic uncertainty in the $\langle\kappa_R\rangle$, and $\langle\kappa_M\rangle$ scales, viz., 0.1% & 0.3% in $\langle\kappa_R\rangle$ & $\langle\kappa_M\rangle$ for RGB stars and 0.3% & 0.9% for RC stars. Note that it is possible there is a scalar correction required of $\langle\Delta\nu'\rangle$, as well. We therefore conservatively treat the uncertainty in $f_{\nu_{\max}}$ as an uncertainty in a scalar contribution to $f_{\Delta\nu}^2$, given that our calibration of the asteroseismic radius, which scales as $f_{\nu_{\max}}^{-1} f_{\Delta\nu}^2$ (Eq. 6), is formally a calibration of the quantity $f_{\nu_{\max}}^{-1} f_{\Delta\nu}^2$. This implies a systematic uncertainty in $\langle\Delta\nu'\rangle$ of 0.05% and 0.15% for RGB stars and RC stars, respectively. As discussed in Zinn et al. (2019b), there are additional systematics in the asteroseismology-Gaia radius comparison that could amount to about $\pm 2\%$ in $f_{\nu_{\max}}$, and which are due to intrinsic uncertainties in the bolometric correction scale, the temperature scale, and the spatial correlations in Gaia parallaxes.

On balance, the modest corrections required to bring the asteroseismic data onto the Gaia parallactic scale support previous findings that the asteroseismic scaling relations are accurate to within a few to several percent
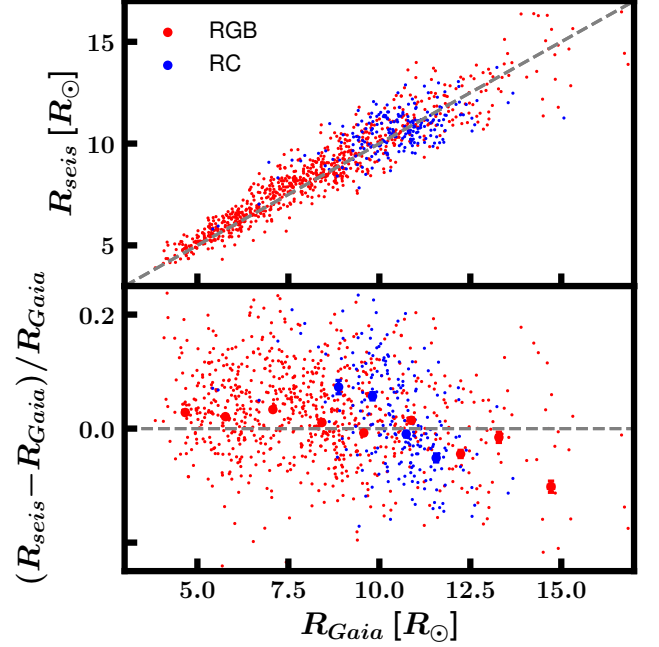

Figure 18. Comparison between Gaia radius and asteroseismic radius for the Gaia-APOGEE-K2 sample used for the calibration of K2 GAP DR3. Binned medians and uncertainties on the medians of the fractional difference in asteroseismic and Gaia radii are plotted as blue (red) error bars for red clump (red giant branch) stars in the bottom panel, while the radii are plotted versus each other in the top panel. Both panels have a grey dashed line to indicate perfect agreement between the two radii. We re-define $\nu_{\max,\odot}$ for the RGB stars and RC stars separately in K2 GAP DR3 such that their radii agree on average with Gaia radii (see Table 3).

on the lower giant branch (e.g., Silva Aguirre et al. 2012; Huber et al. 2012; Hall et al. 2019; Khan et al. 2019; Zinn et al. 2019b). With the assurance that the K2 GAP DR3 asteroseismic masses are well-calibrated, we turn to applications of those data to age-abundance patterns.

5. AGE-ABUNDANCE PATTERNS IN K2 GAP DR3

5.1. *Notes on GALAH abundances*

Our examination of age-abundance patterns makes use of GALAH (GALactic Archaeology with HERMES) DR3 (Buder et al. 2021) abundances for stars targeted as part of the K2-HERMES (Wittenmyer et al. 2018) program. Although our asteroseismic calibration uses APOGEE temperatures and metallicities for deriving asteroseismic radii (§4.2), we note that calibration using GALAH spectroscopic parameters instead results in an equivalent $f_{\nu_{\max}}$ to within uncertainties. We opt to use GALAH abundances in what follows because 1) there are neutron-capture element lines in the optical unavailable to APOGEE's infrared bandpass, and 2) GALAH

abundances are corrected for non-LTE effects for the elements H, Li, C, O, Na, Mg, Al, Si, K, Ca, Mn, Fe, and Ba. On the latter point, non-LTE spectral analysis seems especially important for bringing into agreement dwarf and giant abundances at fixed metallicitiy within ~ 0.05 dex (Amarsi et al. 2020), though some systematics at the 0.1-0.2dex level may remain for Al, Ba, and α-elements, which are mentioned below.

We note that APOGEE DR16 temperatures and GALAH DR3 temperatures for RGB stars differ by $\approx 30K$, in the sense that APOGEE temperatures tend to be hotter. This difference is at the same level as the intrinsic uncertainty in the APOGEE temperature scale, which is set by the accuracy of the infrared flux method (IRFM) temperature scale for red giants (e.g., Alonso et al. 1999; González Hernández & Bonifacio 2009). The metallicity scales of the two systems differ by ≈ -0.05dex, in the sense that APOGEE is more metal-rich. The combined effect of these small offsets means that the asteroseismic parameter calibration performed with APOGEE temperatures in §4 is consistent to within systematic uncertainties of $f_{\nu_{\max}}$ and thus the calibrated parameters are suitable for the following analysis using GALAH temperatures.

It should also be noted that scattering on background opacities was not included in the GALAH DR3 non-LTE calculations. Background scattering may affect giant abundances at the 0.01dex level for elements other than C, Mg, Ca, and Mn, which can have larger effects due to background scattering at lower metallicities (e.g., Hayek et al. 2011). Among metal-poor giants, Mg, Ca, and Mn may thus be under-estimated by up to 0.05 dex for stars with [Fe/H] < -2 (Amarsi et al. 2020).

5.2. Benchmark Galactic chemical evolution model

We compare our age-abundance patterns to the fiducial abundance models of Kobayashi et al. (2020a; K20). The models use nucleosynthetic yields from CCSNe, SNe Ia, AGB stars, and neutron stars mergers, which are discussed as relevant in the discussion that follows. The K20 models assume a one-zone enrichment model, wherein mixing of the interstellar medium is instantaneous, and there is pristine gas inflow. The infall rate and star formation efficiency are chosen to match the metallicity distribution function of the solar neighborhood. For the solar neighborhood model considered here, there is assumed to be no gas outflow. K20 assume single-degenerate SNe Ia, where the total number of SNe is determined from the O/Fe slope. The fraction of main sequence+white dwarf to RGB+white dwarf progenitors is fit to reproduce the observed Galactic metallicity distribution function (see, e.g., Figure A2 of Kobayashi

et al. 2020b). We note that the [Fe/H] at which SNe Ia begin to go off in the K20 models is not simply determined by the delay-time distribution of SNe Ia, but rather the metallicity-dependence of Fe production in SNe Ia (Kobayashi et al. 1998). This is because the K20 models' SNe Ia single-degenerate scenario assumes that white dwarfs surpass the Chandrasekhar mass limit by metallicity-dependent white dwarf winds that prevent common envelope production and encourage stable mass transfer (see Hachisu et al. 1996; Kobayashi et al. 1998; Kobayashi & Nomoto 2009).

The K20 models we use are representative of the solar neighborhood, and so we restrict our analysis to K2 GAP DR3 stars with Galactocentric distances between 7 and 9kpc.

Because the K20 models are calibrated to observations purely in abundance space and not with reference to stellar age measurements, comparing the observed K2 GAP DR3 age-abundance patterns to the models provides an independent check on the success of the assumed global (star formation rate, infall rate) and local (nucleosynthetic yields) model choices. Of particular interest in what follows are the implications for the nucleosynthetic site of production and yields. For comparisons of GALAH DR3 abundance ratios to K20 models, we refer the reader to Amarsi et al. (2020).

5.3. Ages

We derive ages from K2 GAP DR3 asteroseismic masses computed according to Equation 4 with $\langle \kappa_M \rangle$ and GALAH DR3 temperatures. The age inference is performed in a Bayesian framework using BSTEP (Sharma et al. 2018), a Bayesian stellar parameter estimator that may incorporate asteroseismic parameters, $\nu_{\max}$ and $\Delta\nu$, which essentially constrain the mass of the star and therefore its main sequence lifetime. Further details regarding the BSTEP ages used in this work are available in Sharma et al. (2021) (see also Buder et al. (2021)). In what follows, we only use stars that BSTEP classifies with high confidence as RGB, given uncertainties on RC ages due to mass loss (e.g., Casagrande et al. 2016).

5.4. [Mg/H] versus [Fe/H] space

We begin by dividing our sample into high- and low-α samples, following the high-low boundary from Weinberg et al. (2019; W19):

$$\text{for [Fe/H]} < 0 : \text{[Fe/Mg]} > 0.12 - 0.13\text{[Fe/H]}, \quad (9)$$
$$\text{for [Fe/H]} > 0 : \text{[Fe/Mg]} > 0.12. \quad (10)$$

The above division was initially used for stars with APOGEE abundances, though it has subsequently been

used successfully to divide GALAH DR2 (Buder et al. 2018) abundances into high- and low-α populations by Griffith et al. (2019; GJW19), who recently interpreted both APOGEE and GALAH DR2 abundance ratios in the context of Galactic chemical evolution. Following the example of GJW19, we also restrict analysis to those stars with effective temperatures between 4500K and 6200K, which avoids blending in cool stars from molecular lines and highly broadened lines in fully radiative stars.

We believe there is some contamination from genuinely α-poor stars that, by virtue of their abundance uncertainties, scatter into the high-α selection (and vice versa). For this reason, we require that each star's 2D uncertainty ellipse have more than 95% of its density on one side or the other of the high-/low-α division line. In order to construct the 2D uncertainty ellipse, we assume a uniform correlation between [Fe/H] and [Mg/Fe]. The Pearson correlation coefficient between [Fe/H] and [Mg/Fe] is observed to be ~ -0.4, though the precise value adopted does not significantly affect our results. We also require stars to have [Fe/H] > -1 at 95% confidence, since the metal-poor stellar population is likely populated by accretion (e.g., Belokurov et al. 2018; Haywood et al. 2018) rather than in situ formation, as the K20 models assume. The resulting division of the GALAH abundances is demonstrated in Figure 19, where each star is colored by its age. The high-/low-α division line is shown in black. The grey curve represents the raw K20 [Fe/H]-[Mg/Fe] trend, which has been shifted by a scalar offset in [Fe/H] and a scalar offset in [Mg/Fe] to reflect the same solar abundance scale used by GALAH DR3 (see Table A2 of Buder et al. 2021).[9] The segmented blue curve represents the K20 [Fe/H]-[Mg/Fe] trend, re-scaled by an additive offset in Mg such that the median predicted [Mg/Fe] agrees with the median observed [Mg/Fe]. The band around the curve corresponds to a 1σ uncertainty in the Asplund et al. (2009) solar abundances, which are used in the K20 models for abundance normalization.[10]

The sample consists of 396 high-α stars and 208 low-α stars, with typical uncertainties of 20-30% in age.[11] The ages for this sample, as well as their GALAH spec-

troscopic information, and high-/low-α classification are provided in Table 8.

We follow the example of W19 and GJW19 in considering abundance ratio and age-abundance patterns in [X/Mg] space instead of only [X/Fe] space due to the expectation that nearly all Mg production occurs in CC-SNe, whereas Fe is produced by both CCSNe and SNe Ia. Therefore, the low-α population can be interpreted as having SNe Ia contributions, and the high-α population as enriched by CCSNe. Normalizing by Mg means that elements produced only by CCSNe have the same trends in both the low- and high-α regimes. Elements with contributions from SNe Ia, however, will show a separation in [X/Mg] v. [Mg/H] that depends on the relative contribution of CCSNe and SNe Ia. We note that other enrichment channels like AGB winds that do not behave precisely like CCSNe or SNe Ia in their Mg production and delay-time distribution may complicate interpretations of the [X/Mg] versus [Mg/H] trends. Ultimately, showing age-abundance patterns and abundance ratios in [Mg/H] space in addition to [Fe/H] space can offer complementary information to the asteroseismic age information. For instance, CCSNe elements would be expected to 1) have constant [X/Mg] as a function of stellar age; 2) decreasing [X/Fe] as a function of stellar age; and 3) show similar [X/Mg] trends as a function of [Mg/H] for both high- and low-α populations.

We show the distribution of high-α ages in Figure 20. The filled orange histogram shows the distribution of high-α ages larger than 5 Gyr. The orange line indicates the distribution of a simulated population of these stars assuming a mean age of 9 Gyr and with uncertainties taken from the fractional uncertainties of the data. The grey line indicates a population consistent with being 'young' high-α stars, which were originally identified in CoRoT (Baglin et al. 2006) & APOGEE data (Chiappini et al. 2015), and have since been seen in Kepler and K2 data (e.g., Martig et al. 2015; Silva Aguirre et al. 2018; Warfield et al. 2021). These stars may be genuinely old and appear young due to having gained mass through stellar mergers (e.g., Martig et al. 2015; Jofré et al. 2016; Izzard et al. 2018; Sun et al. 2020), or perhaps are genuinely young and have formed in gas relatively unenriched by SNe Ia (Chiappini et al. 2015; Johnson et al. 2021). We therefore draw a distinction between this population and the rest of the high-α population, which are consistent with having a uniform age of ~ 9 Gyr according to a Kolmogorov-Smirnov test.

We show in Figures 21-29 abundance ratios ([X/Fe] versus [Fe/H] or [X/Mg] versus [Mg/H]) and age-abundance patterns/enrichment histories ([X/Fe] versus stellar age or [X/Mg] versus stellar age) for different nu-

---

[9] Where possible, we adopt the 'composite' abundance normalizations listed in Table A2 of Buder et al. (2021) and, otherwise, the average of a given elements' line-by-line normalizations.

[10] The exception is O, whose solar abundance is taken to be $A_\odot(O) = 8.76 \pm 0.02$ (Steffen et al. 2015).

[11] These are the number of stars with Mg and Fe measurements, which are necessary to define the high-α and low-α stars. Note that not all of these stars have abundance measurements for every element we consider in what follows.

cleosynthetic families of elements. A running weighted average of the data are shown as colored error bars connected by lines, with green indicating the low-α population and orange indicating the high-α population. Not plotted are stars with flagged GALAH DR3 abundance measurements in [Fe/H] or in [X/Fe]. As mentioned above, the extent to which the low-α (green curves) pattern is above the high-α (orange curves) pattern in [X/Mg]-[Mg/H] space is generally indicative of nucleosynthetic production site.

Regarding how to compare the K20 models with the data in these figures, we note that at young and intermediate ages, the K20 models may be best interpreted as a low-α population, while the models represent a high-α population at old ages. Because K20 models are one-zone models, there is a one-to-one mapping of age to abundance, which is not necessarily the case in the data. To guide the eye, we therefore highlight in Figure 19 and subsequent figures where the data should be compared to the models: bold curves indicate solidly old/metal-poor high-α stars or young/metal-rich low-α stars, which are comparable to the K20 modelled populations shown in blue, whereas light curves indicate apparent young high-α or old low-α populations not directly comparable to the K20 models. To evaluate the agreement of the models with the data for older, high-α stars, we make reference here and in what follows to a single weighted average of the high-α abundances (which can be seen as a single orange error bar in the following figures), since the width of the high-α age distribution is dominated by uncertainties, and has a central value of ≈ 9 Gyr.

5.5. α elements: O, Mg, Si, Ca, Ti

Looking at O in Figure 21, it is clear that, after a global correction, the observed abundance ratios for [Fe/H] > -1 are in excellent agreement with K20 model predictions. That the metallicity-dependence of O enrichment agrees with observations is a built-in feature of the models: K20 models are adjusted by tuning the total number of supernovae to agree with the observed literature O abundance metallicity dependence (K20). With age information in hand, however, we can independently test the models. We see that the agreement is good when looking at the low-α [O/Mg] trend as a function of time up to $\tau \sim 8$Gyr, tracking Mg production, as an α element would. We see that the high-α [O/Fe] enrichment history is in tension with model predictions at 9Gyr (orange error bar versus blue curve). Given the agreement of the high-α population [O/Fe] as a function of [Fe/H], the disagreement of [O/Fe] for the high-α population in age space suggests an offset in
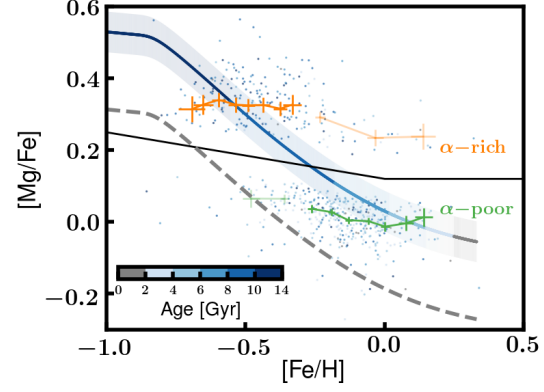

Figure 19. We divide our GALAH DR3 + K2 GAP DR3 sample into high- and low-α samples, following the proposed division from Weinberg et al. (2019; Eq. 9). The stars indicated by orange points are accordingly classified as high-α stars and the stars indicated by green points as low-α stars; the green and orange error bars and curves indicate the 2σ uncertainties on the binned weighted mean of the low-α and high-α stars. The Galactic chemical evolution model from Kobayashi et al. (2020a; K20) is shown before (grey dotted curve) and after (blue segmented curve) an additive correction to [Mg/Fe] to enforce agreement with the median [Mg/Fe] of the observed stars. The region around the blue segmented curve reflects the 1σ uncertainty in the K20 abundance normalization, taken to be the uncertainties in the solar abundances from Asplund et al. (2009). The transparency of the binned weighted means of the data emphasizes where the K20 models track the high-α stars ([Fe/H] $\lesssim -0.3$ and $\tau \gtrsim 8$Gyr) and the low-α stars ([Fe/H] $\gtrsim -0.3$ and $\tau \lesssim 8$Gyr).
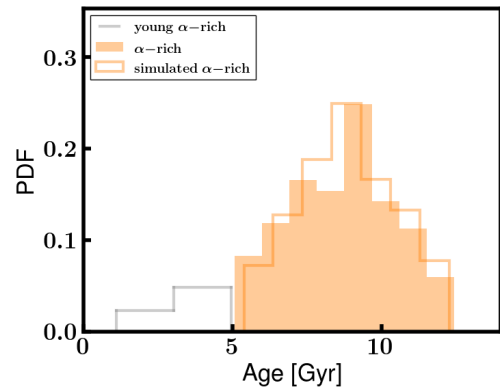

Figure 20. The distribution of high-α ages (filled orange) is consistent with being drawn from a uniform age of 9 Gyr (as simulated in the orange lines). A separate population of young high-α stars with ages $\lesssim 5$ Gyr is shown in grey, and is consistent with previous identifications of a young high-α population in the literature.
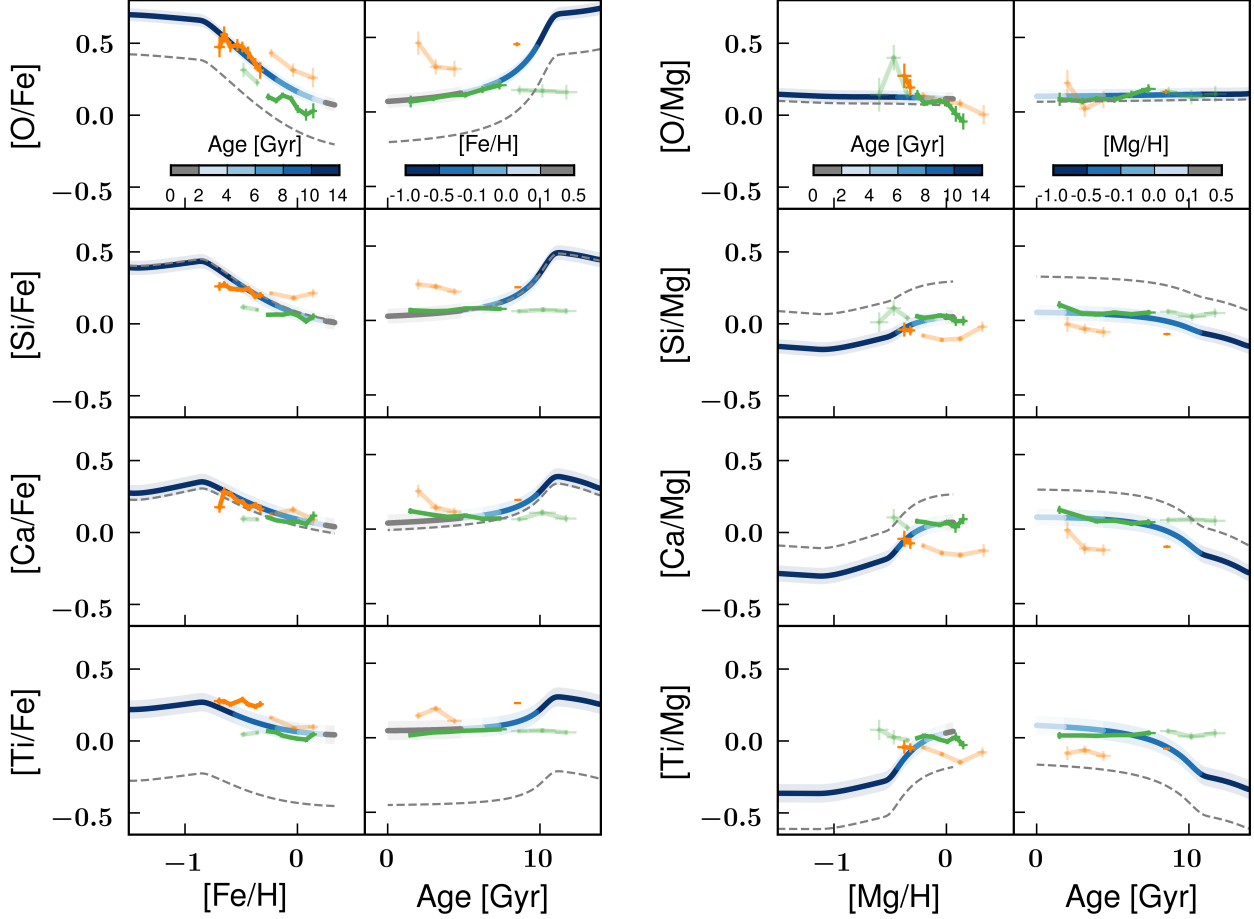
Figure 21. Abundance ratios and age-abundance patterns for α elements, shown in both [X/Fe] and [X/Mg] space. The green and orange error bars and curves indicate the 2σ uncertainties in the binned weighted mean of the low-α and high-α stars. The blue segmented curves show the predictions from the Galactic chemical evolution model of (Kobayashi et al. 2020a; K20), displaced additively in X to agree with the median [X/Fe] or [X/Mg] of the observed stars (grey dashed curves indicate the models before this re-scaling) and colored by either [Fe/H], [Mg/H], or age, according to the color bars. The transparency in the weighted means of the data emphasizes where the K20 models track the high-α stars ([Fe/H] $\lesssim -0.3$ and $\tau \gtrsim 5\,$Gyr) and the low-α stars ([Fe/H] $\gtrsim -0.3$ and $\tau \lesssim 8\,$Gyr). We note that not every star has GALAH measurements for every element, particularly at low metallicities.

the observed and predicted high-α ages. A natural solution would be to appeal to α-enhanced stellar model opacities. Indeed, Warfield et al. (2021) have demonstrated the increase in stellar opacities due to non-solar α abundances can increase low-mass (old) stellar ages by $\approx 10\%$ by decreasing core temperature and extending a red giant's main sequence lifetime. For the majority of elements considered in what follows of §5, an increase in the high-α ages of that magnitude would improve agreement between the data and models. The global offset required to match the O abundances at high metallicities (blue curves versus grey dashed curves), could be due to GALAH α-element abundances O, Mg, and Si having residual offsets of 0.1dex, in the sense that giants have larger [α/Fe] compared to dwarfs even after non-LTE corrections (Amarsi et al. 2020).

Both Ca and Si in Figure 21 show good agreement between the predicted and observed enrichment history: the predicted enrichment history at ages $\tau \lesssim 8\,$Gyr tracks the observed trend (green curve) in [Mg/H] and [Fe/H] space. The models also predict a [Si/Fe] at 9Gyr consistent with the observed abundances of the old high-α population (orange error bar).

We consider Ti an α element, based on the findings in GJW19 that its production seems to be dominated by CCSNe contributions. Indeed, both the low-α and high-α curves share a similar [Ti/Mg] in Figure 21. At older ages, however, the observed high-α [Ti/Fe] abundances are in tension with model predictions for 9Gyr, which
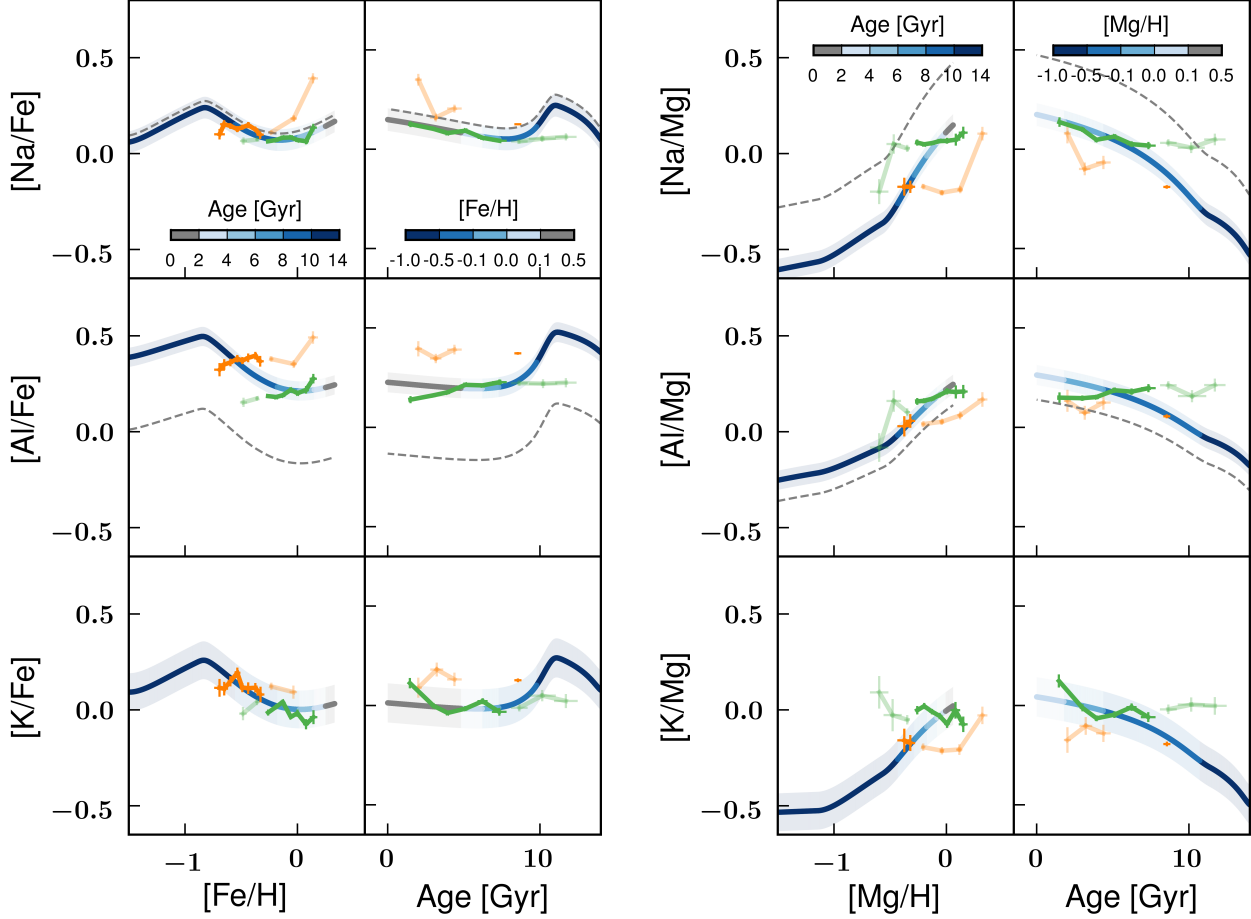
Figure 22. Same as Figure 21, but for light, odd-Z elements.

could be improved via older ages from aforementioned
α-enhanced stellar model opacities. Note that there is
a large zero-point offset between the raw model abun-
dances and the observed abundances (the offset to bring
the raw model abundances into agreement with obser-
vations is the difference between the grey dashed curves
and the blue segmented curves), which is a generic fea-
ture of nucleosynthetic Ti yield predictions, and may
be remedied by 2- or 3-dimensional supernovae models
(K20).

5.6. *Light odd-Z elements: Na, Al, K*

Odd-Z element production is thought to depend on
progenitor metallicity because their assumed produc-
tion during explosive nucleosynthesis in CCSNe depends
crucially on the neutron excess prior to the supernova,
which itself is dependent on CNO cycle efficiency and
therefore intial metal content (e.g., Truran & Arnett
1971). The prediction of nucleosynthetic models for
these elements, therefore is that 1) they should fol-
low a CCSNe enrichment history (either a decreasing

[X/Fe] with younger stellar ages or, equivalently, con-
stant [X/Mg] with stellar age), and 2) they should be
less abundant with decreasing metallicity. In Figure 22,
we show the light, odd-Z elements' abundance ratios and
age-abundance patterns to test these predictions.

The DR3 GALAH [Na/Mg] abundance ratios show a
positive metallicity trend, consistent with findings from
GJW19 using GALAH DR2, and broadly consistent
with the predicted metallicity slope from K20 models.
The enrichment history predictions appear to be consis-
tent with observations, across all ages probed (keeping
in mind the lack of resolution in age space for the high-α
stars, which, to within uncertainties, are drawn from a
single age of ≈ 9Gyr).

The strong, negative metallicity gradient seen by
GJW19 in [K/Mg] is less pronounced with non-LTE
corrections in GALAH DR3, and is in good agreement
with K20 models in [Fe/H] space. The absolute abun-
dances from K20 for K, however, are well below the ob-
served value (the grey dashed curve is below the plot-
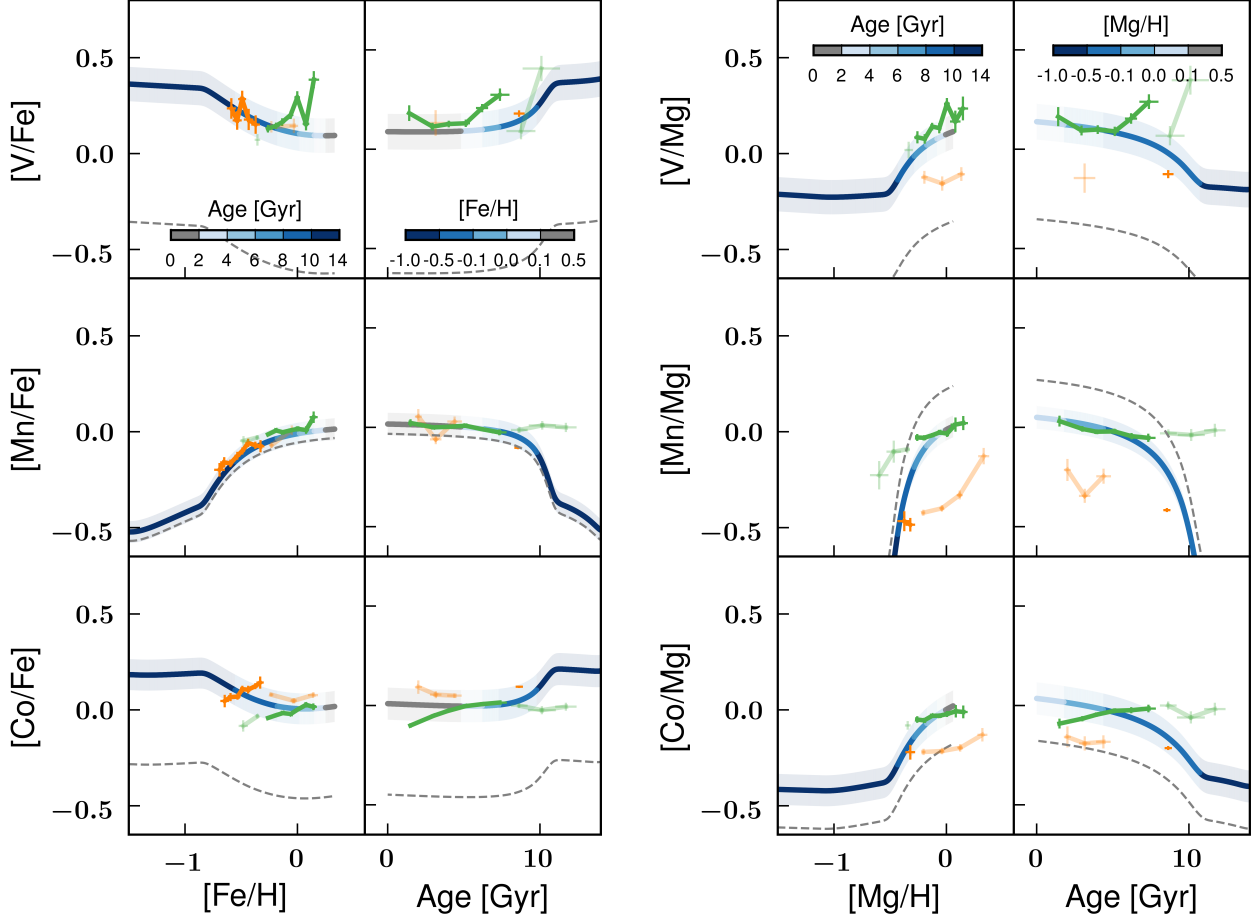ted region), and this offset may be alleviated by appeal-

Figure 23. Same as Figure 21, but for odd-Z iron-peak elements.

ing to, e.g., rotating stellar models (K20 and references therein). The predicted abundances at old stellar age are consistent with those observed among high-α at 9Gyr.

The non-LTE GALAH DR3 corrections to Al reveal a strong metallicity trend with [Al/Mg] not found in GALAH DR2 abundances, but corroborating the positive trend found in APOGEE abundances (GJW19). We confirm GJW19's interpretation of Al being produced largely in CCSNe production, given the relatively small separation between high- and low-α tracks (orange and green curves in [Mg/H] space) compared to, e.g., Na. These observations are both consistent with theoretical predictions of significant, metallicity-dependent Al production during explosive C burning (Truran & Arnett 1971). The observed and predicted enrichment histories are in disagreement. As with O, older high-α ages due to α-enhanced stellar model opacities could improve agreement at old ages. This adjustment would also bring Na and K into even better agreement at old ages. The absolute yields are, as with K, severely under-predicted. This may very well be due to an over-prediction of the abun-

dances on the observational side: even after non-LTE corrections, Al abundances for giants are larger than the dwarf abundances by 0.2dex (Amarsi et al. 2020).

5.7. *Iron-peak elements*

Following GJW19's typology of iron-peak elements, we separate the elements just beyond iron as cliff elements, which seem to have distinct properties from other iron-peak elements. First, we consider the odd-Z iron-peak elements, then the even-Z elements, and, finally, iron-peak cliff elements.

5.7.1. *Odd-Z iron-peak elements: V, Mn, Co*

In this section, we discuss the odd-Z iron-peak element abundance patterns and enrichment histories, as shown in Figure 23. First, we confirm with GALAH DR3 the metallicity trends at high metallicities in V and Mn abundances noted by W19 and GJW19 using APOGEE and GALAH DR2 abundances, respectively. This metallicity-dependent effect is most pronounced in Mn, and is in excellent agreement with the model pre-
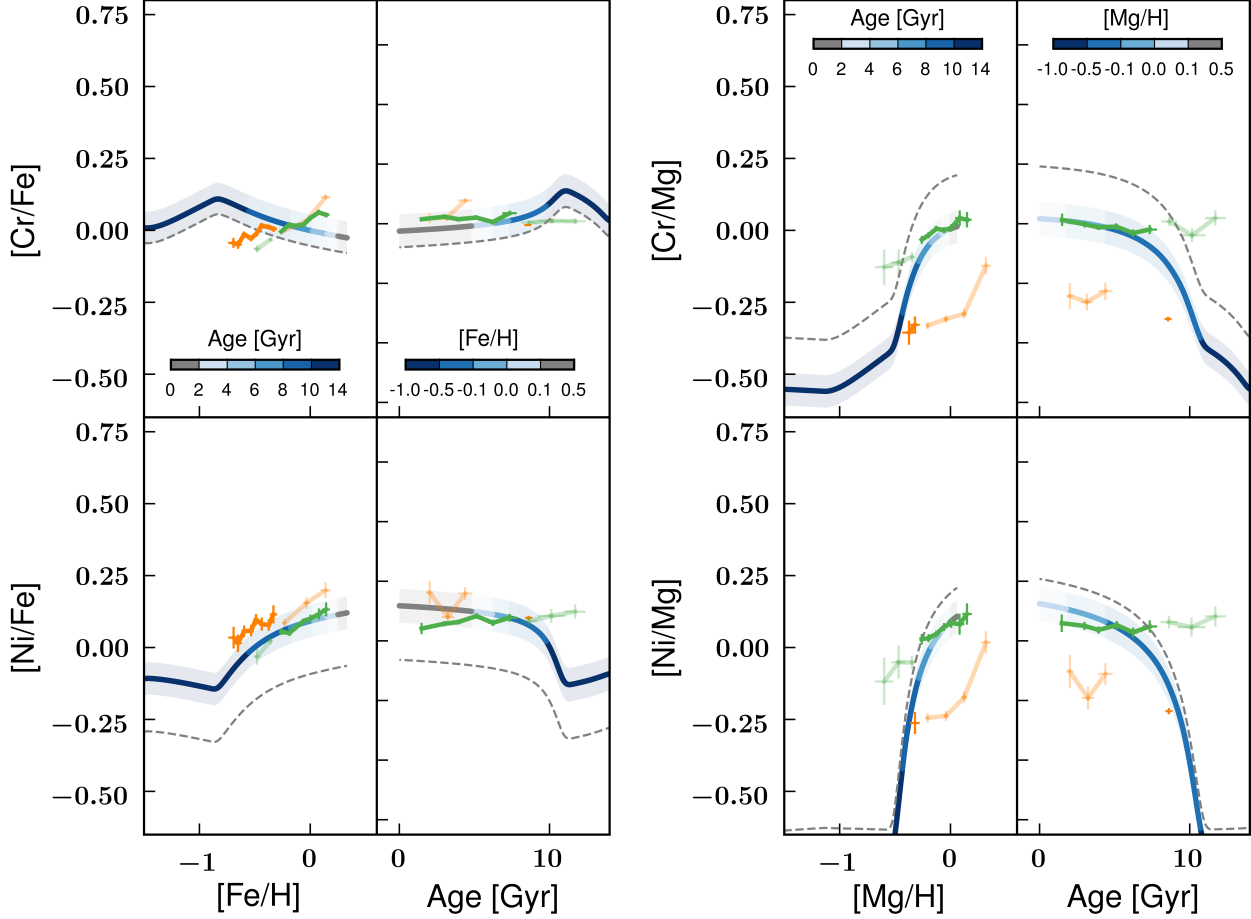
Figure 24. Same as Figure 21, but for even-Z iron-peak elements.

dictions for the trend, which is the result of Mn production in deflagrations with the single-degenerate scenario (Kobayashi et al. 2020b). That the non-LTE Mn abundances from GALAH DR3 still show a metallicity dependence is in contrast to the decrease in the metallicity dependence going from LTE to non-LTE found in Battistini & Bensby (2016).

The observed low-α V pattern agrees well with the K20 predicted [V/Mg] enrichment history including at older ages, where the observed high-α abundance at 9 Gyr broadly agree with the predicted abundance. Nevertheless, the model abundances are uniformly vastly under-predicted compared to observations before a rescaling is applied (grey dashed curves). This under-prediction could be remedied, however, by using yields from multi-dimensional supernovae yield predictions (K20).

The observed and predicted metallicity dependence for Mn are in very good agreement. K20 models also reproduce well the enrichment history of [Mn/Mg] and [Mn/Fe] in the low-α regime. For old, high-α popula-

tions, however, both the [Mn/Mg] and [Mn/Fe] enrichment histories could be improved by older high-α ages due to α-enhanced stellar model opacities (thereby shifting the orange error bar at 9 Gyr to older ages in the Mn enrichment history panels of Fig. 23).

The Co enrichment history agrees well in [Co/Mg] space at old ages, though K20 predicts a too-fast enrichment in the younger low-α population (slope of blue segmented curve versus slope of green curve). As with V, the models significantly under-predict the global abundances for Co.

5.7.2. *Even-Z iron-peak elements: Cr, Ni*

To better reproduce the [Cr/Fe] enrichment history and [Cr/Fe]-[Fe/H] ratios seen in Figure 24, [Cr/Fe] could be made to be produced less overall, such as in the double-degenerate scenario (the green dotted curve of Fig. 18 in Kobayashi et al. 2020a). Note, however, that such low [Cr/Fe] results in higher [α/Fe] and lower [Mn/Fe] and [Ni/Fe] than observed. Otherwise, the observed enrichment history is flatter than predicted in
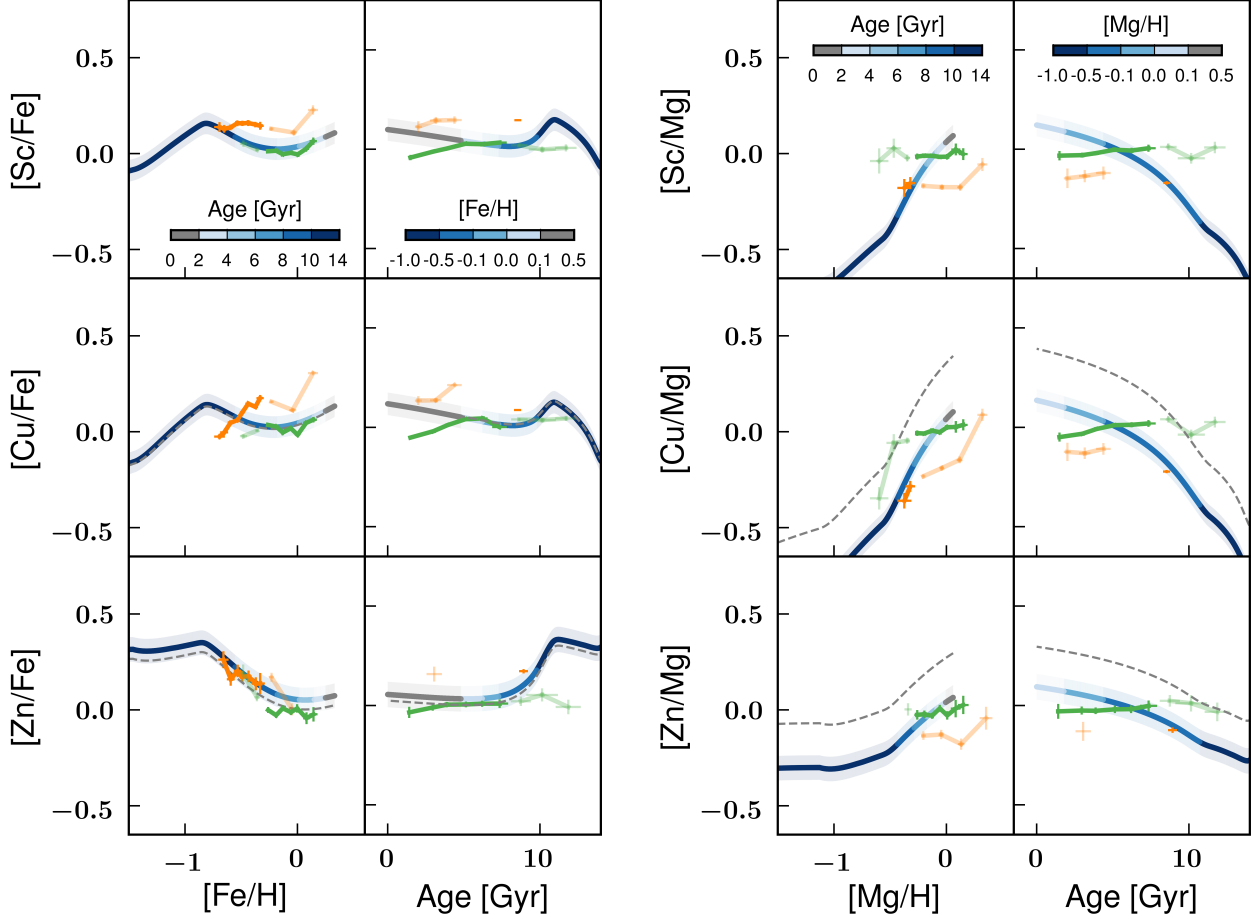
Figure 25. Same as Figure 21, but for iron-peak cliff elements.

[Fe/H] space, but is in better agreement with the models in [Mg/H] space. The disagreement between observed and predicted high-α [Cr/Mg] cannot be redressed only with aforementioned appeals to older high-α ages due to α-enhanced stellar model opacities, which would increase tension in high-α [Cr/Fe]. Rather, this would need to be coupled with a significant decrease in the production of Cr at early times.

Like Cr, the observed age-abundance pattern of Ni in [Fe/H] space seen in Figure 24 is flatter than predicted. Though there is broad agreement in the [Ni/Fe] and [Ni/Mg] high-α enrichment history, it could be improved by an increase (as opposed to a decrease, as with Cr) in Ni at early times combined with older high-α ages due to α-enhanced stellar model opacities, as mentioned earlier. There is also an offset between the raw model abundances (grey dashed curves) and the observed abundances, though the offset is in the opposite direction to that of Cr. Note that the metallicity dependence is in good agreement with model predictions in [Ni/Fe]-[Fe/H] space, in contrast to Cr.

5.7.3. *Iron-peak cliff elements: Sc, Cu, Zn*

Looking at Figure 25, the observed and predicted [Zn/Fe] v. [Fe/H] and age-abundance trend are in good agreement. The small separation in [Zn/Mg] of the low- and high-α sequences corroborate the CCSNe-dominated production assumed in the K20 models and the interpretations of the Zn abundance ratios in GJW19 that Zn is mostly a CCSNe element.

The enrichment history predicted by the K20 models for Cu show strong increases in both [Cu/Mg] and [Cu/Fe] for younger stellar age, which is in disagreement with a slight trend in the other direction among the low-α population (green curves in Fig. 25) in both [Fe/H] and [Mg/H] space. Slightly higher high-α ages in the data would help reconcile the observed and predicted [Cu/Fe].

The Sc age-abundance patterns in Figure 25 show the same behavior as Cu: the models predict an age-dependent trend that is in the opposite direction to that of the observed trends in [Fe/H] and [Mg/H] space, and
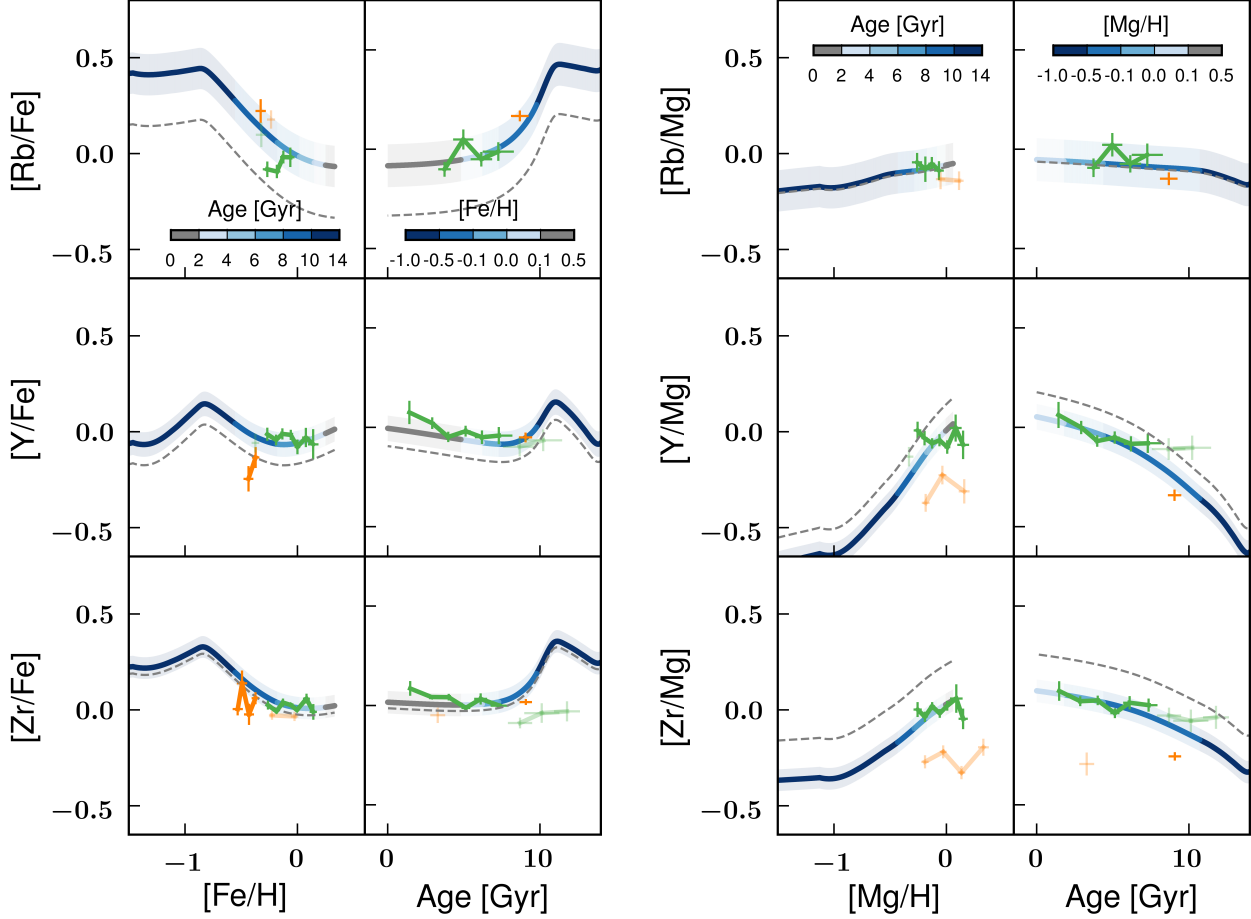
Figure 26. Same as Figure 21, but for weak s-process elements.

the observed high-α population is offset in age compared to the models.

Taken together, the Cu and Sc trends are suggestive of different nucleosynthetic histories compared to Zn. The predicted increase in Cu and Sc yields is theoretically expected due to the metallicity dependence of Cu and Sc yields since both elements are odd-Z (see §5.6). Indeed, the data do show this increase in [Cu/Fe] and at least a flat trend in [Sc/Fe] with [Fe/H] among the low-α population. The observed age trend (a flat or increasing abundance with increasing age among low-α stars) is therefore not straightforwardly related to metallicity-dependent yields, and is an interesting constraint on production of these elements; a similar enrichment history is also seen in the odd-Z element Al (see §5.6).

5.8. *Neutron-capture elements*

Neutron-capture elements can be produced in one of two primary channels: s-process and r-process, which occur in neutron-poor and neutron-rich environments (for a review, see Truran et al. 2002).

There is evidence of two different kinds of r-process production: a 'weak' process that creates elements $A \lesssim 130 - 140$ (e.g., Honda et al. 2004) and the main r-process for elements with $A \gtrsim 130 - 140$ (Truran et al. 2002). The main r-process production site has been proposed to be decompressing neutron-rich ejecta from a neutron star–neutron star (NS-NS) merger (Lattimer & Schramm 1974; Lattimer et al. 1977; Rosswog et al. 1999). However, the delay-time distribution of NS-NS mergers is difficult to reconcile with that needed to reproduce observed r-process enrichment histories both at early and late times (e.g., Hotokezaka et al. 2018; Haynes & Kobayashi 2019). Other r-process channels involving neutrino-driven winds during neutron or magnetar birth may be plausible alternatives (e.g., Qian & Woosley 1996; Hoffman et al. 1997).

Like the r-process, there seem to be a weak and main s-process. The weak s-process occurs in core He burning of $M > 25M_\odot$ stars (Peters 1968; Lamb et al. 1977; Raiteri et al. 1993), and works by way of neutron production from the ^{22}Ne$(\alpha, n)^{25}$Mg reaction to create free
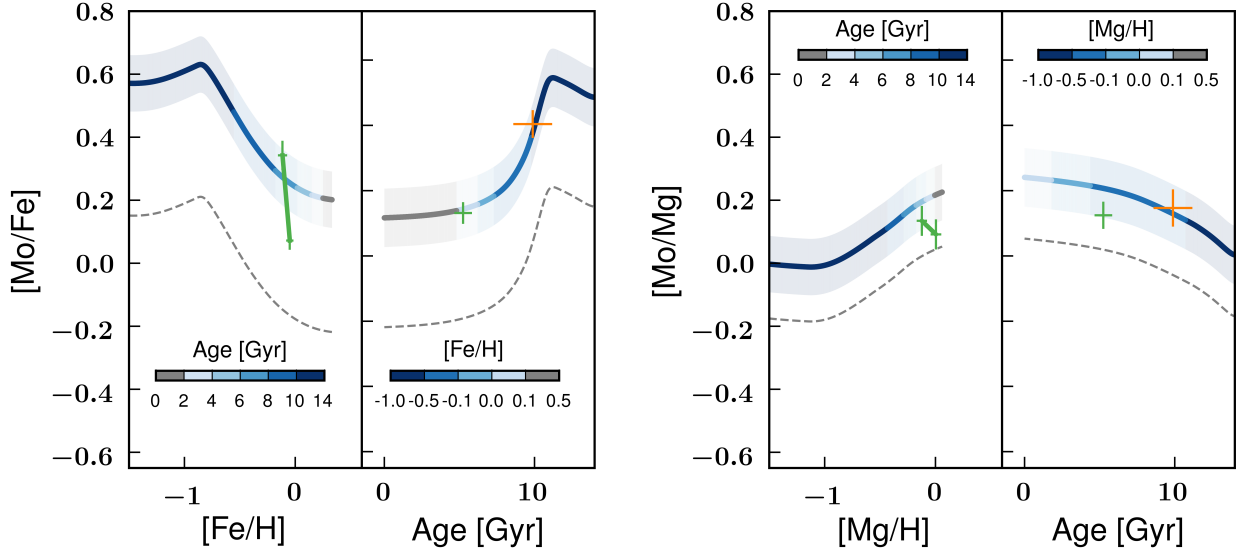
Figure 27. Same as Figure 21, but for the weak r-process element, Mo.

neutrons, which can then build elements up to $A \approx 90$ (Truran et al. 2002). The main s-process occurs during the AGB phase of low- and intermediate-mass stars, ($M \sim 1 - 3 M_\odot$; Schwarzschild & Härm 1967) acting through the $^{13}C(\alpha, n)^{16}O$ reaction, and forming elements with $A \gtrsim 90$.

With K2 GAP DR3 age estimates and GALAH DR3 abundances, we are in a position to test assumed production mechanisms of neutron-capture elements by comparisons to K20 models.

Electron-capture supernovae (ECSNe) are included as a source of neutron-capture elements in K20 models, the effect of which is to form first-peak s-process elements Sr, Y, Zr, Mo, and Ru via nuclear equilibrium processes, as well as weak r-process production from Nd to In (Wanajo et al. 2011). ECSNe are assumed in K20 models to occur between the relatively narrow mass range of $\sim 8.8 - 9 M_\odot$; increases of an order of magnitude in the electron-capture supernova rate have been assumed in the literature, and so may be a tunable parameter to increase bulk yields (see K20 and references therein). The largest contributors to r-process production in the K20 models, however, are magneto-rotational supernovae (MRSNe), which are theorized to be core-collapse supernovae of massive stars with large magnetic fields and/or strong rotation, which develop accretion discs and jets that can be conducive to r-process production (e.g., Symbalisty et al. 1985; Cameron 2003; Nishimura et al. 2017). There is also a NS-NS merger r-process contribution included in K20 models, though its contribution is subdominant compared to that of MRSNe.

5.8.1. *Weak s-process elements: Rb, Y, Zr*

Shown in Figure 26 are the age-abundance ratios of elements thought to be formed through the 'weak' s-process.[12]

The agreement between the observed and predicted age-abundance patterns of [Rb/Mg] and [Rb/Fe] is very good, across both high- and low-α populations.

Although there is an over-prediction in the abundances for the high-α stars at 9 Gyr, the agreement between K20 models and data are also good for [Zr/Mg] and [Zr/Fe], as well.

The K20 age-[Y/Mg] pattern does not reach an equilibrium value, indicating a metallicity-dependence to the s-process production of Y. This metallicity-dependence is also borne out in the data, save for a zero-point offset in [Y/Mg]. The predicted enrichment history is in good agreement in both [Y/Mg] and [Y/Fe] space. The agreement of the observed and predicted Y enrichment histories represents another endorsement of dating stars with Y abundances (e.g., Nissen 2015).

5.8.2. *Weak r-process: Mo*

Although GALAH can measure Ru, the number of stars with good Ru measurements is small, and so we only consider Mo as representative of elements produced as part of the so-called 'weak' r-process.

---

[12] In detail, the K20 models predict that Y and Zr are in fact produced mostly in low- and intermediate-mass AGB stars as part of what we label here the main s-process.
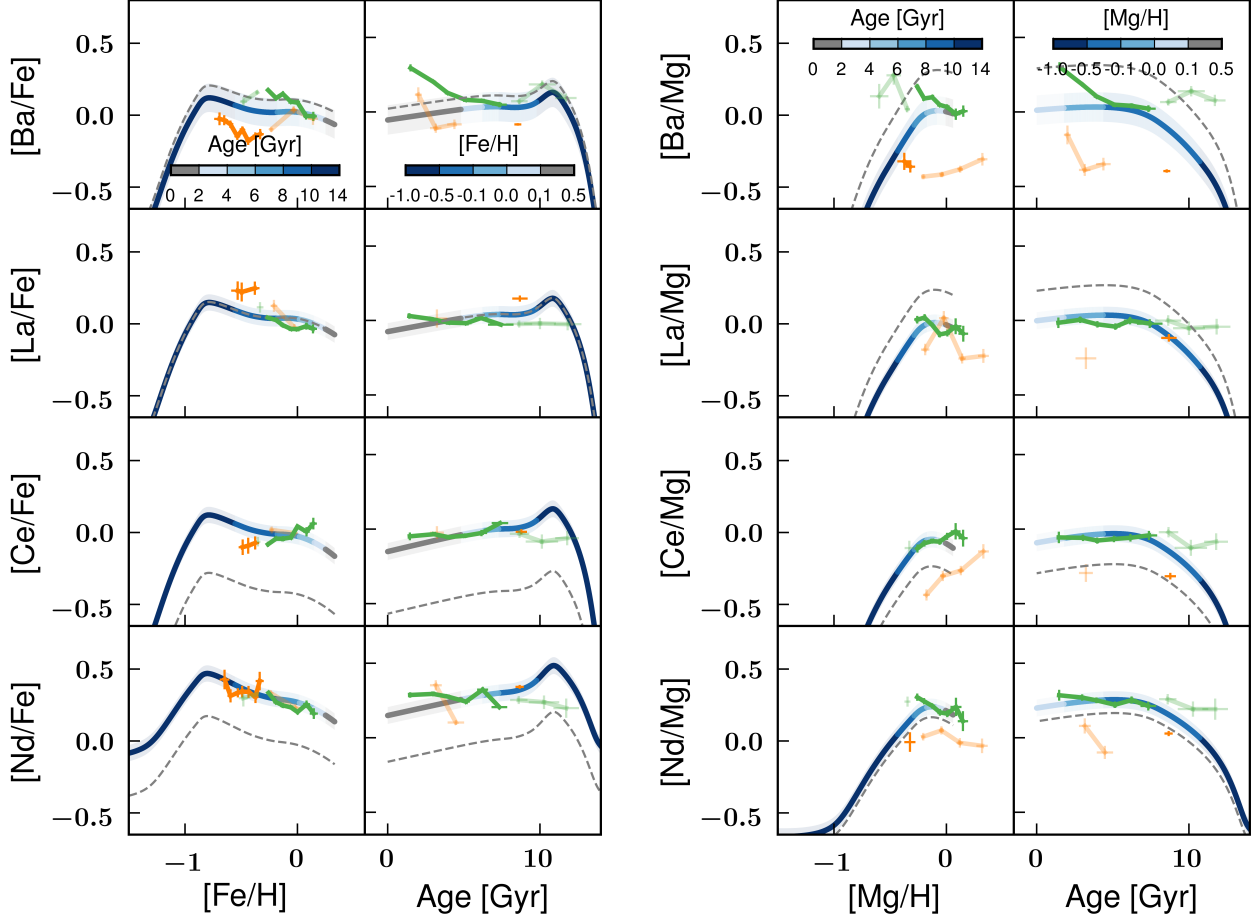
Figure 28. Same as Figure 21, but for main s-process elements.

The K20 models under-predict Mo compared to GALAH (grey curve versus error bars in Fig. 27), which is inconsistent with the inferred over-production compared to high-resolution Mo abundance measurements from the literature (K20). Nevertheless, the predicted history of Mo enrichment is consistent with the observed [Mo/Fe] and [Mo/Mg] age-abundance patterns (blue curve compared to error bars).

5.8.3. Main s-process: Ba, La, Ce, Nd

Ba, shown in Figure 28 is thought to be primarily produced by the s-process at the metallicities considered here ([Fe/H] > −2; Gilroy et al. 1988; Arlandini et al. 1999; Burris et al. 2000). [Ba/Mg] is predicted to reach a plateau in young stars according to K20 models, but the data disfavor a plateau and rather suggest a continually-increasing ratio with younger ages, like [Y/Mg].

D'Orazi et al. (2009) have observed a similar unexpected increase in [Ba/Fe] at young stellar ages, based on open cluster measurements. They proposed that an increased production in low-mass stars would ex-

plain the observations, and which could possibly be related to enhanced mixing into the helium-burning shell thought to be the site of s-process production in low- and intermediate-mass AGB stars. Similar behavior has also been seen in more recent studies (Mishenina et al. 2013; Magrini et al. 2018; Casamiquela et al. 2021). It is unlikely that this enrichment history is explicable by an astrophysical, metallicity-dependent yield, since [Ba/Fe] decreases with increasing [Fe/H], which demonstrates the advantage of analyzing nucleosynthetic yields with age information.

Our results therefore corroborate a mass-dependent Ba yield interpretation, though it is possible the GALAH DR3 Ba abundances themselves are responsible: a trend in Ba with stellar mass would mimic this effect. One candidate for such a systematic may be choice in the microturbulance parameter, given the sensitivity of one of the GALAH Ba lines, Ba II, to that parameter (Dobrovolskas et al. 2012). GALAH DR3 Ba abundances are calculated assuming that RGB stars with the same effective temperature, surface gravity, and [Fe/H]
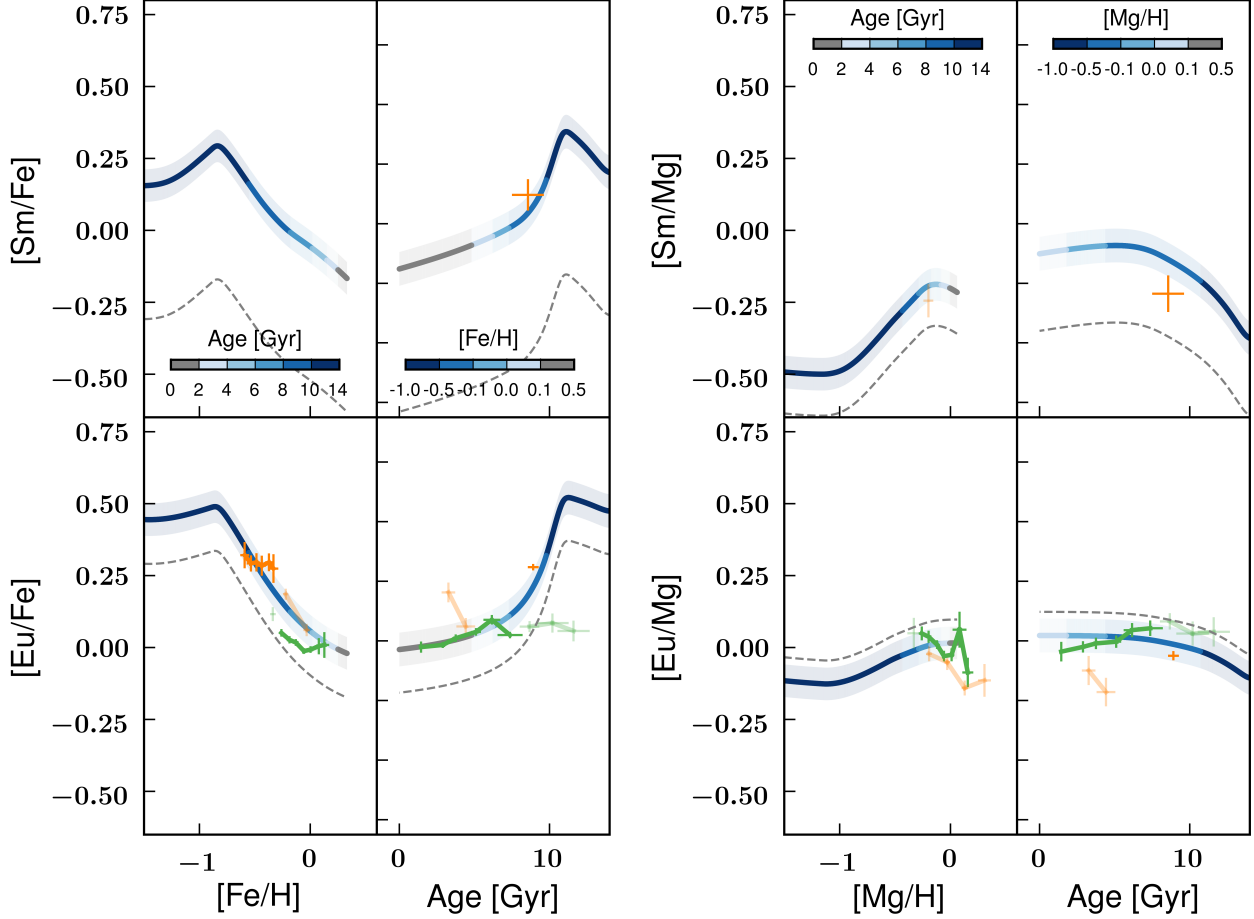
Figure 29. Same as Figure 21, but for main r-process elements.

have the same microturbulence velocity. That is not necessarily the case, and could lead to artificial shifts in the measured Ba abundance with, e.g., mass/age. Regarding the zero-point offset in the Ba abundances compared to the K20 models under no re-scaling (grey dashed lines), the RGB Ba abundances are systematically larger than the dwarf abundances by 0.2 dex. Were the RGB Ba abundances placed on the dwarf scale, then, there would be an even larger global offset between observations and models than shown here. On the model side, K20 noted offsets compared to other literature Ba abundances, noting that they could be remedied by imposing a smaller mixing region during AGB dredge-up. Based on our findings, the models may improve agreement with observations more specifically with a mass-dependent increase in the mixing region.

The predicted and observed enrichment histories of La, Ce, and Nd are in good agreement, as seen in Figure 28. The exception in this agreement is Ce among high-α stars, which is low compared to predictions, even after considering a $\approx 10\%$ increase in the observed ages,

potentially indicating the need for less Ce production in K20 models at early times.

5.8.4. *Main r-process elements: Sm, Eu*

We show in Figure 29 the abundances of the two main r-process elements available in GALAH DR3, Sm and Eu.

Given the relatively few stars in GALAH DR3 with measured Sm abundances, it is difficult to determine the precise agreement with K20 models as a function of age. It does, however, appear that the high-α abundances at old ages are broadly consistent with the predicted enrichment history, though could be improved more with older high-α ages from α-enhanced stellar opacities.

Eu is mostly produced via the r-process (Arlandini et al. 1999; Battistini & Bensby 2016), and, according to the K20 models, the primary site of r-process production is MRSNe (see Fig. 32 in K20), where the rate of MRSNe is chosen to be 3% of massive CCSNe (hypernovae) with mass $M > 25M_{\odot}$ in order to reproduce the [Eu/Fe]-[Fe/H] trend in the solar neighborhood.

The K20 models are in good agreement with both GALAH abundance ratios, and the asteroseismic age-abundance patterns in [Eu/Fe], when comparing models to low-α stars (green curves) at intermediate and young ages ($\tau \lesssim 8$Gyr) and comparing models to high-α stars (orange error bars at 9Gyr in the Eu enrichment history panels of Fig. 29) at older ages. Consistent with studies of metal-poor systems with significant r-process enrichment (e.g., Barklem et al. 2005; Hansen et al. 2018), Lin et al. (2019) corroborated the short time-delay of Eu production sites using isochronal stellar ages of subgiants combined with GALAH DR2 abundances. In this context, the agreement of the observed K2 GAP DR3–GALAH DR3 Eu enrichment history with that of the MNSRe-dominated K20 Eu models gives further credence to a significant contribution to r-process elements from a prompt source — e.g., late-time collapsar accretion disk outflows associated with MRSNe (Symbalisty et al. 1985; Cameron 2003; Nicholl et al. 2013; Vlasov et al. 2014; Siegel et al. 2019).

6. CONCLUSIONS

The K2 GAP DR3 sample, as the largest asteroseismic sample published to date, and probing a range of Galactic environment, represents an important tool for Galactic archaeology and stellar physics. With 18821 total radius and mass coefficients for red giant branch (RGB) and red clump (RC) stars delivered as part of this final data release, below are our main results.

1. We calibrated our asteroseismic values to be on the Gaia parallactic scale. The radius and mass coefficients, κ_R and κ_M, that are released in K2 GAP DR3 need only be multiplied by a temperature-dependent factor according to the user's preferred temperatures to yield radii and masses. The typical uncertainties in these coefficients are 2.9% (stat.) $\pm$ 0.1% (syst.) & 6.7% (stat.) $\pm$ 0.3% (syst.) in κ_R & κ_M for RGB stars and 4.7% (stat.) $\pm$ 0.3% (syst.) & 11% (stat.) $\pm$ 0.9% (syst.) for RC stars. All of the stars with κ_R and κ_M are classified as red giant branch or red clump stars, according to a machine-learning approach.

2. Using injection tests, we estimate that our completeness in radius peaks for stars with $R \sim 10R_\odot$,

where our recovery rate is around 80%. There is a sharp decline in completeness at smaller radii, and a more gradual decline in completeness at larger radii. We estimate a nearly uniform completeness in mass space of $\sim 60\%$.

3. Injection tests suggest systematics of $1 - 3\%$ may arise due to the shorter time baseline of K2 compared to Kepler, and take the form of both zero-point biases and trends as a function of $\nu_{\max}$, $\Delta\nu$, and signal-to-noise ratio. These findings should be informative for future studies using short–time baseline TESS light curves, which would presumably suffer from similar, if not more severe, systematics.

4. We derived ages with typical precisions of 20% for a subset of the K2 GAP DR3 sample based on GALAH metallicities and effective temperatures. In combination with GALAH abundances, we compared observed age-abundance patterns with those predicted by Kobayashi et al. (2020a) as an independent check on the abundance evolution of low- and high-α stars. We corroborate recent inferences regarding the nucleosynthesis of α, light, iron-peak, and neutron-capture elements based on abundance ratios alone (e.g., Griffith et al. 2019). Following similar indications from the Lin et al. (2019) analysis of GALAH DR2 subgiants with isochronal ages, we find evidence for significant production of Eu at early times, consistent with core-collapse supernovae as the predominant site of r-process production. Our findings also suggest mass-dependent Ba yields, in support of indications from D'Orazi et al. (2009).

Studies of Galactic chemical evolution stand to benefit enormously from a continued focus on considering age and not just stellar abundances themselves, as we have shown here. Indeed, ages are of crucial importance in interpreting chemo-kinematic relations (Minchev et al. 2019) — particularly ages with the level of precision reported here (e.g., Martig et al. 2014). As the largest asteroseismic dataset in the literature, K2 GAP DR3 will prove useful not only for Galactic studies, but also for testing stellar models using the sample's evolutionary state classifications coupled with its accurate and precise asteroseismic masses and radii.

Table 2. Derived asteroseismic $\nu_{\max}$ and $\Delta\nu$ values

EPIC ID	$\langle\nu'_{\max}\rangle$	$\sigma_{\langle\nu'_{\max}\rangle}$	$\varsigma_{\langle\nu'_{\max}\rangle}$	$N_{\nu\max}$	$\langle\Delta\nu'\rangle$	$\sigma_{\langle\Delta\nu'\rangle}$	$\varsigma_{\langle\Delta\nu'\rangle}$	$N_{\Delta\nu}$	X_{Sharma}	$\sigma_{X\mathrm{Sharma}}$	$\langle\Delta\nu\rangle$	$\nu'_{\max,\mathrm{A2Z}}$	$\nu'_{\max,\mathrm{BAM}}$	$\nu'_{\max,\mathrm{BHM}}$	$\nu'_{\max,\mathrm{CAN}}$	$\nu'_{\max,\mathrm{COR}}$	$\nu'_{\max,\mathrm{SYD}}$	$\Delta\nu'_{\mathrm{A2Z}}$	$\Delta\nu'_{\mathrm{BAM}}$	$\Delta\nu'_{\mathrm{BHM}}$	$\Delta\nu'_{\mathrm{CAN}}$	$\Delta\nu'_{\mathrm{COR}}$	$\Delta\nu'_{\mathrm{SYD}}$	EPIC T_{eff}	σ_T	EPIC [Fe/H]	$\sigma_{\mathrm{[Fe/H]}}$
	μHz	μHz	μHz		μHz	μHz	μHz				μHz	μHz	μHz	μHz	μHz	μHz	μHz	μHz	μHz	μHz	μHz	μHz	μHz	K	K		
210306475	28.041	1.274	1.495	5	3.495	0.112	0.176	3	1.026	0.008	3.405	28.575	30.053	26.808	27.801	—	29.351	—	3.361	3.568	—	—	3.539	4797	134	-0.266	0.300
210307958	28.380	0.933	1.308	5	3.965	0.134	0.100	3	1.032	0.014	3.842	27.964	30.233	—	29.399	28.349	28.369	—	3.852	—	4.112	3.925	—	4750	138	-0.359	0.260
210314854	30.482	1.034	1.669	6	4.171	0.064	0.129	5	1.017	0.019	4.102	29.055	31.776	31.093	30.745	31.639	31.693	—	4.201	4.169	4.119	4.268	4.112	4953	174	-0.510	0.330
210315825	58.454	0.341	1.990	6	6.093	0.059	0.096	5	1.025	0.011	5.944	59.632	59.091	59.795	59.671	58.958	59.540	—	6.065	6.175	6.083	6.123	6.018	4827	180	-0.298	0.300
210318976	24.052	0.501	1.350	5	3.541	0.043	0.083	2	1.031	0.014	3.434	24.821	25.012	—	23.772	24.539	24.162	—	—	—	3.568	3.507	—	4680	140	-0.199	0.260

NOTE—Asteroseismic values re-scaled for scalar offsets among pipelines are denoted by a prime (the pipeline-specific solar reference scale factors are listed in Table 3); mean $\nu_{\max}$ and $\Delta\nu$ values for each star across all pipelines are denoted by $\langle\nu'_{\max}\rangle$ and $\langle\Delta\nu'\rangle$; the standard deviation of these values for each star across all pipelines are denoted by $\sigma_{<\nu\max'>}$ and $\sigma_{<\Delta\nu'>}$, and are the adopted uncertainties for K2 GAP DR3. $\varsigma_{\langle\nu'_{\max}\rangle}$ and $\varsigma_{\langle\Delta\nu'\rangle}$ are conservative estimates of statistical uncertainties based on reported pipeline statistical uncertainties. $\langle\Delta\nu'\rangle$ is adjusted using theoretically-motivated correction factors, X_{Sharma} (Sharma et al. 2016), for use in asteroseismic scaling relations; an uncorrected version of $\langle\Delta\nu'\rangle$ for each star is provided, $\langle\Delta\nu\rangle = \langle\Delta\nu'\rangle/X_{\mathrm{Sharma}}$, should the user wish to compute custom $\Delta\nu$ corrections. EPIC temperatures and metallicities are provided for this purpose, though these are relatively uncertain estimates of the true temperatures and metallicities (these uncertainties are also provided for convenience). The uncertainties in X_{Sharma}, $\sigma_{X\mathrm{Sharma}}$, are computed by perturbing the EPIC temperature and metallicities in a Monte Carlo procedure. Note that $\sigma_{X\mathrm{Sharma}}$ are not provided for EPIC ID 240289249 and EPIC ID 235193028, which have anomalously large EPIC temperature uncertainties. $\langle\nu'_{\max}\rangle$ values have an evolutionary state–dependent correction applied to align asteroseismic radii with Gaia radii, per §4. Pipeline-specific re-scaled values, $\nu'_{\max}$ and $\Delta\nu'$, are only provided for targets for which at least two pipelines returned concordant results, and otherwise have a blank entry; the numbers of pipelines returning valid results for $\nu_{\max}$ or $\Delta\nu$ are denoted by $N_{\nu\max}$ and $N_{\Delta\nu}$. A2Z $\Delta\nu'$ values are not provided, since A2Z $\Delta\nu$ values do not contribute to $\langle\Delta\nu'\rangle$. See text for details. A full version of this table is available in the online journal.

Table 3. Solar reference value scale factors and solar reference values

	A2Z	CAN	COR	SYD	BAM	BHM	K2 GAP DR3
$X_{\nu_{max}, \text{RGB, APOKASC2}}$	1.00230 ± 0.00002	1.00820 ± 0.00002	0.99890 ± 0.00002	1.00060 ± 0.00002	—	—	
$X_{\nu_{max}, \text{RGB}}$	0.9991 ± 0.0006	0.9953 ± 0.0003	1.0000 ± 0.0003	0.9990 ± 0.0007	1.0027 ± 0.0003	1.0034 ± 0.0003	
$\nu_{max,\odot,\text{RGB}}$	$3095 \pm 2~\mu\text{Hz}$	$3125 \pm 1~\mu\text{Hz}$	$3050 \pm 1~\mu\text{Hz}$	$3087 \pm 2~\mu\text{Hz}$	$3102 \pm 1~\mu\text{Hz}$	$3060 \pm 1~\mu\text{Hz}$	$3076~\mu\text{Hz}$
$X_{\Delta\nu, \text{RGB, APOKASC2}}$	0.99930 ± 0.00001	1.00070 ± 0.00001	1.00510 ± 0.00001	0.99950 ± 0.00001	—	—	
$X_{\Delta\nu, \text{RGB}}$	—	1.0042 ± 0.0002	1.0004 ± 0.0004	1.0001 ± 0.0012	0.9969 ± 0.0007	0.9978 ± 0.0005	
$\Delta\nu_{\odot,\text{RGB}}$	—	$135.48 \pm 0.03~\mu\text{Hz}$	$134.97 \pm 0.05~\mu\text{Hz}$	$135.1 \pm 0.2~\mu\text{Hz}$	$134.42 \pm 0.10~\mu\text{Hz}$	$134.62 \pm 0.06~\mu\text{Hz}$	$135.146~\mu\text{Hz}$
$X_{\nu_{max}, \text{RC, APOKASC2}}$	1.00350 ± 0.00003	1.00670 ± 0.00002	0.99090 ± 0.00002	1.00100 ± 0.00003	—	—	
$X_{\nu_{max}, \text{RC}}$	0.9951 ± 0.0011	0.9935 ± 0.0006	0.9992 ± 0.0005	0.996 ± 0.001	1.0131 ± 0.0005	1.0024 ± 0.0006	
$\nu_{max,\odot,\text{RC}}$	$3082 \pm 4~\mu\text{Hz}$	$3120 \pm 2~\mu\text{Hz}$	$3048 \pm 2~\mu\text{Hz}$	$3077 \pm 4~\mu\text{Hz}$	$3134 \pm 1~\mu\text{Hz}$	$3057 \pm 2~\mu\text{Hz}$	$3076~\mu\text{Hz}$
$X_{\Delta\nu, \text{RC, APOKASC2}}$	0.99650 ± 0.00003	1.01080 ± 0.00002	0.99600 ± 0.00001	1.00320 ± 0.00002	—	—	
$X_{\Delta\nu, \text{RC}}$	—	1.0066 ± 0.0005	1.0010 ± 0.0005	0.999 ± 0.002	0.993 ± 0.002	0.9971 ± 0.0007	
$\Delta\nu_{\odot,\text{RC}}$	—	$135.81 \pm 0.07~\mu\text{Hz}$	$135.06 \pm 0.07~\mu\text{Hz}$	$134.9 \pm 0.3~\mu\text{Hz}$	$133.9 \pm 0.3~\mu\text{Hz}$	$134.53 \pm 0.10~\mu\text{Hz}$	$135.146~\mu\text{Hz}$

NOTE—Solar reference value scale factors and solar reference values (see §3), compared to those computed for some of the same pipelines using a similar method with *Kepler* data (Pinsonneault et al. 2018; "APOKASC-2"). The adopted solar reference values for K2 GAP DR3 are listed in the last column. A2Z $\Delta\nu$ solar reference value scale factors and solar reference values are not provided, since A2Z $\Delta\nu$ values do not contribute to $\langle\Delta\nu'\rangle$; see Table 1 for the default A2Z $\Delta\nu_\odot$ value.

Table 4. Radius and mass coefficients

EPIC ID	$\langle\kappa_R\rangle$	$\sigma_{\langle\kappa_R\rangle}$	$\langle\kappa_M\rangle$	$\sigma_{\langle\kappa_M\rangle}$	$\kappa'_{R,\mathrm{A2Z}}$	$\kappa'_{R,\mathrm{BAM}}$	$\kappa'_{R,\mathrm{BHM}}$	$\kappa'_{R,\mathrm{CAN}}$	$\kappa'_{R,\mathrm{COR}}$	$\kappa'_{R,\mathrm{SYD}}$	$\sigma_{\kappa R',\mathrm{A2Z}}$	$\sigma_{\kappa R',\mathrm{BAM}}$	$\sigma_{\kappa R',\mathrm{BHM}}$	$\sigma_{\kappa R',\mathrm{CAN}}$	$\sigma_{\kappa R',\mathrm{COR}}$	$\sigma_{\kappa R',\mathrm{SYD}}$	$\kappa'_{M,\mathrm{A2Z}}$	$\kappa'_{M,\mathrm{BAM}}$	$\kappa'_{M,\mathrm{BHM}}$	$\kappa'_{M,\mathrm{CAN}}$	$\kappa'_{M,\mathrm{COR}}$	$\kappa'_{M,\mathrm{SYD}}$	$\sigma_{\kappa M',\mathrm{A2Z}}$	$\sigma_{\kappa M',\mathrm{BAM}}$	$\sigma_{\kappa M',\mathrm{BHM}}$	$\sigma_{\kappa M',\mathrm{CAN}}$	$\sigma_{\kappa M',\mathrm{COR}}$	$\sigma_{\kappa M',\mathrm{SYD}}$
210306475	13.406	1.086	1.694	0.331	12.815	15.798	12.502	—	—	13.912	1.012	1.901	1.298	—	—	1.573	1.515	2.438	1.362	—	—	1.847	0.359	0.605	0.324	—	—	0.484
210307958	10.541	0.818	1.060	0.186	—	12.100	—	10.323	10.927	—	—	0.836	—	0.594	0.562	—	—	1.439	—	1.019	1.100	—	—	0.213	—	0.142	0.134	—
210314854	10.232	0.480	1.073	0.133	10.158	10.690	10.625	10.757	10.313	11.131	0.926	0.493	1.029	0.599	0.479	1.870	0.968	1.181	1.141	1.157	1.094	1.277	0.233	0.125	0.236	0.180	0.123	0.552
210315825	9.194	0.193	1.661	0.075	10.034	9.539	9.312	9.576	9.338	9.763	0.818	0.292	0.609	0.335	0.332	0.541	1.938	1.748	1.686	1.779	1.671	1.845	0.412	0.140	0.235	0.151	0.143	0.296
210318976	11.201	0.368	1.015	0.084	13.643	—	—	11.089	11.847	—	1.087	—	—	0.798	0.623	—	1.492	—	—	0.950	1.120	—	0.347	—	—	0.175	0.139	—

NOTE—$\langle\kappa_R\rangle$ and $\langle\kappa_M\rangle$, and their uncertainties, computed based on $\langle\Delta\nu'\rangle$ and $\langle\nu'_{\max}\rangle$, according to Equations 6 & 8. $\langle\kappa_R\rangle$ and $\langle\kappa_M\rangle$ values have an evolutionary state–dependent correction to align asteroseismic radii with Gaia radii, per §4. Pipeline-specific radius and mass coefficients, κ'_R and κ'_M, are computed with pipeline-specific asteroseismic parameters, $\Delta\nu'$ and $\nu'_{\max}$. See §3 for details. A full version of this table is available in the online journal.

Table 5. Median fractional uncertainties of Kepler and K2 asteroseismic quantities (in percent)

	RGB or	RGB/AGB			RC			
	APOKASC-2	Y18	K2 GAP DR2	K2 GAP DR3	APOKASC-2	Y18	K2 GAP DR2	K2 GAP DR3
$\sigma_{\nu_{\mathrm{max}}}$	0.9	1.0	1.7	1.3	1.3	2.1	2.4	2.2
$\sigma_{\Delta\nu}$	0.4	0.3	1.7	1.1	1.1	1.1	2.3	1.8
σ_{κ_R}	1.3	1.1	3.3	2.9	2.7	3.3	5.0	4.7
σ_{κ_M}	3.4	3.1	7.7	6.7	6.2	8.4	10.5	11

NOTE—"APOKASC-2" indicates median fractional uncertainties from the analysis of Pinsonneault et al. (2018), while "Y18" refers to the analysis of Yu et al. (2018). K2 GAP DR2 uncertainties are taken from Table 7 of Zinn et al. (2020).

Table 6. Raw asteroseismic $\nu_{\max}$ and $\Delta\nu$ values, with evolutionary states

ID	EPIC ID	Campaign	Priority	Evo. State (EV)	A2Z EV	BAM EV	BHM EV	CAN EV	COR EV	SYD EV
210306475_4	210306475	4	903	RGB	RGB	RGB	RC	—	—	RC
210307958_4	210307958	4	2771	RGB	—	RC	—	RC	RGB	—
210314854_4	210314854	4	1141	RGB	RGB	RC	RGB	RGB	RC	RC
210315825_4	210315825	4	1651	RGB	RGB	RGB	RGB	RGB	RGB	RGB
210318976_4	210318976	4	988	RGB	RGB	—	—	RGB	RGB	—

$\nu_{\max,\mathrm{A2Z}}$	$\sigma_{\nu\max,\mathrm{A2Z}}$	$\Delta\nu_{\mathrm{A2Z}}$	$\sigma_{\Delta\nu,\mathrm{A2Z}}$	$\nu_{\max,\mathrm{BAM}}$	$\sigma_{\nu\max,\mathrm{BAM}}$	$\Delta\nu_{\mathrm{BAM}}$	$\sigma_{\Delta\nu,\mathrm{BAM}}$	$\nu_{\max,\mathrm{BHM}}$	$\sigma_{\nu\max,\mathrm{BHM}}$	$\Delta\nu_{\mathrm{BHM}}$
μHz	μHz	μHz	μHz	μHz	μHz	μHz	μHz	μHz	μHz	μHz
28.550	2.25	3.620	0.010	30.135	0.808	3.277	0.197	26.900	1.4	3.470
27.940	2.47	3.890	—	30.316	0.723	3.723	0.124	—	—	—
29.030	2.03	4.100	0.120	31.863	0.743	4.115	0.083	31.200	1.0	4.090
59.580	3.63	5.910	0.160	59.253	1.379	5.899	0.060	60.000	1.3	6.010
24.800	1.88	3.270	0.040	25.080	0.841	—	—	21.700	1.1	3.080

$\sigma_{\Delta\nu,\mathrm{BHM}}$	$\nu_{\max,\mathrm{CAN}}$	$\sigma_{\nu\max,\mathrm{CAN}}$	$\Delta\nu_{\mathrm{CAN}}$	$\sigma_{\Delta\nu,\mathrm{CAN}}$	$\nu_{\max,\mathrm{COR}}$	$\sigma_{\nu\max,\mathrm{COR}}$	$\Delta\nu_{\mathrm{COR}}$	$\sigma_{\Delta\nu,\mathrm{COR}}$	$\nu_{\max,\mathrm{SYD}}$	$\sigma_{\nu\max,\mathrm{SYD}}$	$\Delta\nu_{\mathrm{SYD}}$	$\sigma_{\Delta\nu,\mathrm{SYD}}$
μHz	μHz	μHz	μHz	μHz	μHz	μHz	μHz	μHz	μHz	μHz	μHz	μHz
0.160	27.670	1.27	—	—	—	—	—	—	29.322	1.742	3.450	0.170
—	29.260	1.03	4.004	0.094	28.350	0.83	3.805	0.083	28.341	1.478	—	—
0.190	30.600	1.49	4.066	0.056	31.640	0.89	4.204	0.079	31.662	3.853	4.033	0.238
0.190	59.390	1.28	5.960	0.084	58.960	1.26	5.975	0.087	59.482	3.086	5.873	0.058
0.100	23.660	1.22	3.482	0.090	24.540	0.73	3.402	0.076	24.138	2.070	—	—

NOTE.—'Raw' asteroseismic parameters returned by a given pipeline, along with their uncertainties, without the re-scaling described in §3 applied. Evolutionary states are also given for stars with both $\langle\nu'_{\max}\rangle$ and $\langle\Delta\nu'\rangle$ values (EV) as well for individual pipeline values (A2Z EV, BAM EV, etc.); see text for details. If classified, a star's evolutionary state is assigned as either "RGB", "RGB/AGB", or "RC". "Priority" refers to the K2 GAP target priority for a given K2 campaign, which is discussed in §2 (a smaller numerical value corresponds to higher priority); serendipitous targets do not have a populated priority entry. 'ID' is a unique combination of the EPIC ID and from which campaign the measurements come (some stars were observed in multiple campaigns). A full version of this table is available in the online journal.

Table 7. Numbers of stars with raw asteroseismic values (ν_{max}, $\Delta\nu$), re-scaled asteroseismic values (ν'_{max}, $\Delta\nu'$), and radius & mass coefficients (κ'_R, κ'_M), as a function of pipeline and campaign

		ν_{max}	ν'_{max}	$\Delta\nu$	$\Delta\nu'$	κ'_R	κ'_M
C1	A2Z	672	541	672	0	541	541
C2	A2Z	2326	993	1932	0	833	833
C3	A2Z	1418	834	1042	0	636	636
C4	A2Z	1966	1272	1536	0	1116	1116
C5	A2Z	3088	2088	2398	0	1761	1761
C6	A2Z	1086	1311	1086	0	1215	1215
C7	A2Z	993	835	293	0	224	224
C8	A2Z	1254	718	959	0	581	581
C10	A2Z	1660	832	1213	0	629	629
C11	A2Z	1359	670	1058	0	540	540
C12	A2Z	1717	866	1280	0	678	678
C13	A2Z	2393	1578	1924	0	1304	1304
C14	A2Z	1571	799	1138	0	621	621
C15	A2Z	3777	2598	2906	0	2055	2055
C16	A2Z	2685	1621	2025	0	1388	1388
C17	A2Z	1913	1173	1458	0	1016	1016
C18	A2Z	423	230	323	0	221	221
Total	A2Z	30301	17291	23243	0	13827	13827
C1	BAM	948	698	757	457	457	457
C2	BAM	2591	1030	361	264	264	264
C3	BAM	1288	791	493	434	434	434
C4	BAM	2478	1282	844	751	751	751
C5	BAM	3001	2066	1158	1242	1242	1242
C6	BAM	2529	1626	955	1005	1005	1005
C7	BAM	2315	1202	677	587	587	587
C8	BAM	1107	719	426	385	385	385
C10	BAM	1568	852	428	348	348	348
C11	BAM	1339	647	275	229	229	229
C12	BAM	1603	878	471	419	419	419
C13	BAM	2262	1547	817	734	734	734
C14	BAM	1304	810	479	433	433	433
C15	BAM	3526	2589	1367	1261	1261	1261
C16	BAM	2269	1645	2269	1400	1400	1400
C17	BAM	1713	1209	609	763	763	763
C18	BAM	408	227	108	149	149	149
Total	BAM	32249	18115	12494	9641	9641	9641
C1	BHM	1030	670	1030	592	592	592
C2	BHM	1818	1009	1551	933	933	933
C3	BHM	1191	842	1086	775	775	775
C4	BHM	1984	1251	1529	1126	1126	1126
C5	BHM	2750	2120	2550	1933	1933	1933

Table 7 *continued*

Table 7 *(continued)*

		$\nu_{\max}$	$\nu'_{\max}$	$\Delta\nu$	$\Delta\nu'$	κ'_R	κ'_M
C6	BHM	2275	1606	1702	1370	1370	1370
C7	BHM	1803	1186	1238	989	989	989
C8	BHM	1094	722	869	656	656	656
C10	BHM	1590	871	1081	723	723	723
C11	BHM	1012	612	807	546	546	546
C12	BHM	1416	867	1053	749	749	749
C13	BHM	2112	1548	1764	1403	1403	1403
C14	BHM	1261	817	1003	739	739	739
C15	BHM	3216	2532	2730	2299	2299	2299
C16	BHM	2198	1648	1731	1400	1400	1400
C17	BHM	1697	1226	1307	1069	1069	1069
C18	BHM	344	249	266	218	218	218
Total	BHM	28791	18049	23297	16014	16014	16014
C1	CAN	1105	778	582	482	482	482
C2	CAN	1609	948	616	503	503	503
C3	CAN	1116	816	494	433	433	433
C4	CAN	1897	1204	968	793	793	793
C5	CAN	2530	2030	1559	1458	1458	1458
C6	CAN	1956	1514	1455	1273	1273	1273
C7	CAN	1564	1083	1048	879	879	879
C8	CAN	935	713	785	606	606	606
C10	CAN	1234	840	1093	679	679	679
C11	CAN	1000	612	874	515	515	515
C12	CAN	1181	854	1104	753	753	753
C13	CAN	1975	1548	1851	1326	1326	1326
C14	CAN	958	755	854	677	677	677
C15	CAN	3032	2497	2817	2250	2250	2250
C16	CAN	1814	1581	1633	1336	1336	1336
C17	CAN	780	1039	733	884	884	884
C18	CAN	297	235	260	191	191	191
Total	CAN	24983	17386	18726	13650	13650	13650
C1	COR	777	681	777	610	610	610
C2	COR	1635	960	1635	930	930	930
C3	COR	1022	757	1022	699	699	699
C4	COR	1803	1233	1803	1177	1177	1177
C5	COR	2526	1953	2526	1774	1774	1774
C6	COR	1443	1404	1443	1286	1286	1286
C7	COR	1561	1162	1561	1127	1127	1127
C8	COR	955	681	955	617	617	617
C10	COR	1449	824	1449	737	737	737
C11	COR	1048	613	1048	570	570	570
C12	COR	1309	819	1309	740	740	740
C13	COR	1879	1470	1879	1389	1389	1389
C14	COR	1034	755	1034	699	699	699
C15	COR	2944	2432	2944	2342	2342	2342
C16	COR	1833	1490	1833	1323	1323	1323

Table 7 *continued*

Table 7 *(continued)*

		$\nu_{\max}$	$\nu'_{\max}$	$\Delta\nu$	$\Delta\nu'$	κ'_R	κ'_M
C17	COR	1368	1080	1368	977	977	977
C18	COR	265	201	265	164	164	164
Total	COR	24851	17019	24851	15850	15850	15850
C1	SYD	558	490	472	418	418	418
C2	SYD	1290	684	486	397	397	397
C3	SYD	1066	752	668	588	588	588
C4	SYD	2151	1270	735	670	670	670
C5	SYD	2627	2001	1627	1515	1515	1515
C6	SYD	2232	1472	782	743	743	743
C7	SYD	1678	1088	505	481	481	481
C8	SYD	937	681	588	518	518	518
C10	SYD	1138	715	466	385	385	385
C11	SYD	1583	699	459	378	378	378
C12	SYD	1097	751	584	511	511	511
C13	SYD	2007	1519	1230	1103	1103	1103
C14	SYD	1079	768	672	586	586	586
C15	SYD	3128	2492	1990	1819	1819	1819
C16	SYD	1886	1598	1229	1184	1184	1184
C17	SYD	598	1091	325	629	629	629
C18	SYD	266	232	176	183	183	183
Total	SYD	25321	16688	12994	11080	11080	11080

Table 8. K2 GAP DR3 ages with GALAH spectroscopy

EPIC ID	sobject_id	τ	σ_τ	[Fe/H]	$\sigma_{\rm [Fe/H]}$	[Mg/Fe]	$\sigma_{\rm [Mg/Fe]}$	$T_{\rm eff}$	$\sigma_{T_{\rm eff}}$	$\alpha_{\rm hi}$
		Gyr	Gyr					K	K	
220387110	161007003801220	7.7	1.8	-0.2	0.1	0.2	0.1	4691	91	—
220352927	161007003801158	11.1	1.5	-1.3	0.1	0.1	0.1	4883	124	—
220420379	161007003801285	5.2	2.9	-0.6	0.1	0.3	0.2	4705	136	—
220329169	161007003801110	4.1	0.7	-0.3	0.1	0.1	0.1	4864	95	—
220425435	161007003801301	9.2	2.7	-1.6	0.2	0.1	0.2	5060	174	—
220377647	161007003801390	4.2	0.9	-0.4	0.1	0.2	0.1	4995	116	—
220382480	161007003801378	10.8	1.7	-0.7	0.2	0.2	0.2	5085	190	—
220392564	161007003801360	6.6	2.5	-0.9	0.1	0.3	0.2	4791	137	—
220408286	161007003801353	6.0	4.0	-0.2	0.1	0.1	0.1	4770	111	—
220272081	161006004401209	9.1	3.0	-0.6	0.1	0.4	0.1	4559	87	1

NOTE—Ages and GALAH metallicities, [Mg/Fe], and effective temperatures for the subset of the K2 GAP DR3 sample with GALAH data. sobject_id is the GALAH observation ID, which may be used to cross-match with GALAH catalogues. $\alpha_{\rm hi}$ is 1 (0) if the star has GALAH abundances indicative of a high-α (low-α) star at 2σ confidence; if the classification is ambiguous, the entry is blank (see text for details). A full version of this table is available in the online journal.

REFERENCES

Adibekyan, V. Z., Sousa, S. G., Santos, N. C., et al. 2012, A&A, 545, A32

Ahumada, R., Prieto, C. A., Almeida, A., et al. 2020, ApJS, 249, 3

Alonso, A., Arribas, S., & Martínez-Roger, C. 1999, A&AS, 139, 335, doi: 10.1051/aas:1999506

Amarsi, A. M. 2020, Grid/NLTE, Zenodo, doi: 10.5281/zenodo.3982506

Amarsi, A. M., Lind, K., Osorio, Y., et al. 2020, A&A, 642, A62

An, D., Pinsonneault, M. H., Terndrup, D. M., & Chung, C. 2019, ApJ, 879, 81

Anders, F., Chiappini, C., Rodrigues, T. S., et al. 2017, A&A, 597, A30

Arlandini, C., Käppeler, F., Wisshak, K., et al. 1999, ApJ, 525, 886

Asplund, M., Grevesse, N., Sauval, A. J., & Scott, P. 2009, ARA&A, 47, 481

Baglin, A., Michel, E., Auvergne, M., & COROT Team. 2006, in ESA Special Publication, Vol. 624, Proceedings of SOHO 18/GONG 2006/HELAS I, Beyond the spherical Sun, 34.1

Barklem, P. S., Christlieb, N., Beers, T. C., et al. 2005, A&A, 439, 129

Battistini, C., & Bensby, T. 2016, A&A, 586, A49

Bedding, T. R., Mosser, B., Huber, D., et al. 2011, Nature, 471, 608

Belkacem, K., Goupil, M. J., Dupret, M. A., et al. 2011, A&A, 530, A142

Belkacem, K., Samadi, R., Mosser, B., Goupil, M. J., & Ludwig, H. G. 2013, in Astronomical Society of the Pacific Conference Series, Vol. 479, Progress in Physics of the Sun and Stars: A New Era in Helio- and Asteroseismology, ed. H. Shibahashi & A. E. Lynas-Gray, 61

Belokurov, V., Erkal, D., Evans, N. W., Koposov, S. E., & Deason, A. J. 2018, Monthly Notices of the Royal Astronomical Society, 478, 611

Bennett, M., & Bovy, J. 2019, MNRAS, 482, 1417

Bensby, T., Feltzing, S., & Lundström, I. 2003, A&A, 410, 527

Bland-Hawthorn, J., Sharma, S., Tepper-Garcia, T., et al. 2019, MNRAS, 486, 1167, doi: 10.1093/mnras/stz217

Blanton, M. R., Bershady, M. A., Abolfathi, B., et al. 2017, AJ, 154, 28

Borucki, W., Koch, D., Basri, G., et al. 2008, in IAU Symposium, Vol. 249, Exoplanets: Detection, Formation and Dynamics, ed. Y.-S. Sun, S. Ferraz-Mello, & J.-L. Zhou, 17–24, doi: 10.1017/S174392130801630X

Bovy, J., Rix, H.-W., Green, G. M., Schlafly, E. F., & Finkbeiner, D. P. 2016, ApJ, 818, 130, doi: 10.3847/0004-637X/818/2/130

Brogaard, K., Hansen, C. J., Miglio, A., et al. 2018, MNRAS, 476, 3729

Brown, T. M., Gilliland, R. L., Noyes, R. W., & Ramsey, L. W. 1991, ApJ, 368, 599, doi: 10.1086/169725

Buder, S., Asplund, M., Duong, L., et al. 2018, MNRAS, 478, 4513

Buder, S., Sharma, S., Kos, J., et al. 2021, MNRAS, 506, 150

Burbidge, E. M., Burbidge, G. R., Fowler, W. A., & Hoyle, F. 1957, Rev. Mod. Phys., 29, 547

Burris, D. L., Pilachowski, C. A., Armand roff, T. E., et al. 2000, ApJ, 544, 302

Cameron, A. G. W. 2003, ApJ, 587, 327

Campante, T. L., Schofield, M., Kuszlewicz, J. S., et al. 2016, ApJ, 830, 138

Carlberg, R. G., & Sellwood, J. A. 1985, ApJ, 292, 79, doi: 10.1086/163134

Casagrande, L., Silva Aguirre, V., Schlesinger, K. J., et al. 2016, MNRAS, 455, 987

Casamiquela, L., Soubiran, C., Jofré, P., et al. 2021, arXiv e-prints, arXiv:2103.14692

Chan, V. C., & Bovy, J. 2020, MNRAS, 493, 4367

Chaplin, W. J., Houdek, G., Appourchaux, T., et al. 2008, A&A, 485, 813, doi: 10.1051/0004-6361:200809695

Chiappini, C., Matteucci, F., & Gratton, R. 1997, ApJ, 477, 765

Chiappini, C., Anders, F., Rodrigues, T. S., et al. 2015, A&A, 576, L12

Clarke, A. J., Debattista, V. P., Nidever, D. L., et al. 2019, MNRAS, 484, 3476

Corsaro, E., Fröhlich, H. E., Bonanno, A., et al. 2013, MNRAS, 430, 2313

De Silva, G. M., Freeman, K. C., Bland-Hawthorn, J., et al. 2015, MNRAS, 449, 2604

Dobrovolskas, V., Kučinskas, A., Andrievsky, S. M., et al. 2012, A&A, 540, A128

D'Orazi, V., Magrini, L., Randich, S., et al. 2009, ApJL, 693, L31

Epstein, C. R., Elsworth, Y. P., Johnson, J. A., et al. 2014, ApJL, 785, L28

Foreman-Mackey, D. 2016, The Journal of Open Source Software, 1, 24, doi: 10.21105/joss.00024

Foreman-Mackey, D., Hogg, D. W., Lang, D., & Goodman, J. 2013, PASP, 125, 306, doi: 10.1086/670067

Fuhrmann, K. 1998, A&A, 338, 161

Gaia Collaboration, Brown, A. G. A., Vallenari, A., et al. 2016, A&A, 595, A2

—. 2018, A&A, 616, A1, doi: 10.1051/0004-6361/201833051

García, R. A., Mathur, S., Pires, S., et al. 2014, A&A, 568, A10, doi: 10.1051/0004-6361/201323326

García Pérez, A. E., Allende Prieto, C., Holtzman, J. A., et al. 2016, AJ, 151, 144

Gilroy, K. K., Sneden, C., Pilachowski, C. A., & Cowan, J. J. 1988, ApJ, 327, 298

González Hernández, J. I., & Bonifacio, P. 2009, A&A, 497, 497, doi: 10.1051/0004-6361/200810904

Grand, R. J. J., Springel, V., Gómez, F. A., et al. 2016, MNRAS, 459, 199

Gratton, R. G., Carretta, E., Matteucci, F., & Sneden, C. 2000, A&A, 358, 671

Gravity Collaboration, Abuter, R., Amorim, A., et al. 2019, A&A, 625, L10

Green, G. M., Schlafly, E. F., Finkbeiner, D. P., et al. 2015, ApJ, 810, 25, doi: 10.1088/0004-637X/810/1/25

Griffith, E., Johnson, J. A., & Weinberg, D. H. 2019, ApJ, 886, 84

Gunn, J. E., Siegmund, W. A., Mannery, E. J., et al. 2006, AJ, 131, 2332

Hachisu, I., Kato, M., & Nomoto, K. 1996, ApJL, 470, L97

Hall, O. J., Davies, G. R., Elsworth, Y. P., et al. 2019, MNRAS, 486, 3569

Handberg, R., & Lund, M. N. 2014, MNRAS, 445, 2698

Hansen, T. T., Holmbeck, E. M., Beers, T. C., et al. 2018, ApJ, 858, 92

Hayden, M. R., Recio-Blanco, A., de Laverny, P., Mikolaitis, S., & Worley, C. C. 2017, A&A, 608, L1

Hayden, M. R., Bovy, J., Holtzman, J. A., et al. 2015, ApJ, 808, 132

Hayek, W., Asplund, M., Collet, R., & Nordlund, Å. 2011, A&A, 529, A158

Haynes, C. J., & Kobayashi, C. 2019, MNRAS, 483, 5123

Haywood, M., Di Matteo, P., Lehnert, M. D., Katz, D., & Gómez, A. 2013, A&A, 560, A109

Haywood, M., Di Matteo, P., Lehnert, M. D., et al. 2018, ApJ, 863, 113

Heiter, U., Jofré, P., Gustafsson, B., et al. 2015, A&A, 582, A49

Hekker, S., Broomhall, A.-M., Chaplin, W. J., et al. 2010, MNRAS, 402, 2049, doi: 10.1111/j.1365-2966.2009.16030.x

Hekker, S., Elsworth, Y., Mosser, B., et al. 2012, A&A, 544, A90

Hoffman, R. D., Woosley, S. E., & Qian, Y. Z. 1997, ApJ, 482, 951

Holtzman, J. A., Shetrone, M., Johnson, J. A., et al. 2015, AJ, 150, 148

Holtzman, J. A., Hasselquist, S., Shetrone, M., et al. 2018, AJ, 156, 125

Hon, M., Stello, D., & Yu, J. 2017, MNRAS, 469, 4578

—. 2018, MNRAS, 476, 3233

Honda, S., Aoki, W., Kajino, T., et al. 2004, ApJ, 607, 474

Hotokezaka, K., Beniamini, P., & Piran, T. 2018, International Journal of Modern Physics D, 27, 1842005

Howell, S. B., Sobeck, C., Haas, M., et al. 2014, PASP, 126, 398

Huber, D., Stello, D., Bedding, T. R., et al. 2009, Communications in Asteroseismology, 160, 74. https://arxiv.org/abs/0910.2764

Huber, D., Bedding, T. R., Stello, D., et al. 2010, ApJ, 723, 1607

Huber, D., Ireland, M. J., Bedding, T. R., et al. 2012, ApJ, 760, 32, doi: 10.1088/0004-637X/760/1/32

Huber, D., Bryson, S. T., Haas, M. R., et al. 2016, ApJS, 224, 2, doi: 10.3847/0067-0049/224/1/2

Huber, D., Zinn, J., Bojsen-Hansen, M., et al. 2017, ApJ, 844, 102, doi: 10.3847/1538-4357/aa75ca

Hunter, J. D. 2007, Computing in Science & Engineering, 9, 90, doi: 10.1109/MCSE.2007.55

Izzard, R. G., Preece, H., Jofre, P., et al. 2018, MNRAS, 473, 2984

Jofré, P., Jorissen, A., Van Eck, S., et al. 2016, A&A, 595, A60

Johnson, J. W., Weinberg, D. H., Vincenzo, F., et al. 2021, arXiv e-prints, arXiv:2103.09838

Jørgensen, A. C. S., Montalbán, J., Miglio, A., et al. 2020, MNRAS, 495, 4965

Jørgensen, A. C. S., Montalbán, J., Angelou, G. C., et al. 2021, MNRAS, 500, 4277

Jørgensen, B. R., & Lindegren, L. 2005, A&A, 436, 127, doi: 10.1051/0004-6361:20042185

Kallinger, T., Beck, P. G., Stello, D., & Garcia, R. A. 2018, A&A, 616, A104

Kallinger, T., Hekker, S., Garcia, R. A., Huber, D., & Matthews, J. M. 2016, Science Advances, 2, 1500654, doi: 10.1126/sciadv.1500654

Kallinger, T., Mosser, B., Hekker, S., et al. 2010, A&A, 522, A1, doi: 10.1051/0004-6361/201015263

Kenney, J. F., & Keeping, E. S. 1962, Mathematics of Statistics, Pt. 1, 3rd ed. (Princeton, NJ: Van Nostrand)

Khan, S., Miglio, A., Mosser, B., et al. 2019, A&A, 628, A35

Kjeldsen, H., & Bedding, T. R. 1995, A&A, 293, 87

Kobayashi, C., Karakas, A. I., & Lugaro, M. 2020a, ApJ, 900, 179

Kobayashi, C., Leung, S.-C., & Nomoto, K. 2020b, ApJ, 895, 138

Kobayashi, C., & Nakasato, N. 2011, ApJ, 729, 16

Kobayashi, C., & Nomoto, K. 2009, ApJ, 707, 1466

Kobayashi, C., Tsujimoto, T., Nomoto, K., Hachisu, I., & Kato, M. 1998, ApJL, 503, L155

Kos, J., Lin, J., Zwitter, T., et al. 2017, MNRAS, 464, 1259

Lamb, S. A., Howard, W. M., Truran, J. W., & Iben, I., J. 1977, ApJ, 217, 213

Lattimer, J. M., Mackie, F., Ravenhall, D. G., & Schramm, D. N. 1977, ApJ, 213, 225

Lattimer, J. M., & Schramm, D. N. 1974, ApJL, 192, L145

Lin, J., Asplund, M., Ting, Y.-S., et al. 2019, MNRAS, 2724

Lindegren, L., Hernández, J., Bombrun, A., et al. 2018, A&A, 616, A2

Luger, R., Kruse, E., Foreman-Mackey, D., Agol, E., & Saunders, N. 2018, AJ, 156, 99

Mackereth, J. T., Crain, R. A., Schiavon, R. P., et al. 2018, MNRAS, 477, 5072

Magrini, L., Spina, L., Randich, S., et al. 2018, A&A, 617, A106, doi: 10.1051/0004-6361/201832841

Majewski, S. R., Wilson, J. C., Hearty, F., Schiavon, R. R., & Skrutskie, M. F. 2010, in IAU Symposium, Vol. 265, Chemical Abundances in the Universe: Connecting First Stars to Planets, ed. K. Cunha, M. Spite, & B. Barbuy, 480–481, doi: 10.1017/S1743921310001298

Majewski, S. R., Schiavon, R. P., Frinchaboy, P. M., et al. 2017, AJ, 154, 94

Mamajek, E. E., Prsa, A., Torres, G., et al. 2015, arXiv e-prints, arXiv:1510.07674

Martell, S. L., Sharma, S., Buder, S., et al. 2017, MNRAS, 465, 3203

Martig, M., Minchev, I., & Flynn, C. 2014, MNRAS, 443, 2452

Martig, M., Rix, H.-W., Silva Aguirre, V., et al. 2015, MNRAS, 451, 2230

Mathur, S., García, R. A., Huber, D., et al. 2016, ApJ, 827, 50, doi: 10.3847/0004-637X/827/1/50

Mathur, S., García, R. A., Régulo, C., et al. 2010, A&A, 511, A46

McKinney, W. 2010, in Proceedings of the 9th Python in
    Science Conference, ed. S. van der Walt & J. Millman, 51
    – 56

McWilliam, A. 1997, ARA&A, 35, 503

Miglio, A., Brogaard, K., Stello, D., et al. 2012, MNRAS,
    419, 2077

Miglio, A., Chiappini, C., Mackereth, J. T., et al. 2021,
    A&A, 645, A85

Minchev, I., Martig, M., Streich, D., et al. 2015, ApJL, 804,
    L9

Minchev, I., & Quillen, A. C. 2006, MNRAS, 368, 623,
    doi: 10.1111/j.1365-2966.2006.10129.x

Minchev, I., Matijevic, G., Hogg, D. W., et al. 2019,
    MNRAS, 487, 3946

Mishenina, T., Korotin, S., Carraro, G., Kovtyukh, V. V.,
    & Yegorova, I. A. 2013, MNRAS, 433, 1436

Mosser, B., & Appourchaux, T. 2009, A&A, 508, 877,
    doi: 10.1051/0004-6361/200912944

Mosser, B., Belkacem, K., Goupil, M. J., et al. 2010, A&A,
    517, A22, doi: 10.1051/0004-6361/201014036

Mosser, B., Dziembowski, W. A., Belkacem, K., et al. 2013,
    A&A, 559, A137

Ness, M., Hogg, D. W., Rix, H. W., Ho, A. Y. Q., &
    Zasowski, G. 2015, ApJ, 808, 16

Ness, M., Hogg, D. W., Rix, H.-W., et al. 2016, ApJ, 823,
    114, doi: 10.3847/0004-637X/823/2/114

Newberg, H. J., Carlin, J. L., Chen, L., et al. 2012, in
    Astronomical Society of the Pacific Conference Series,
    Vol. 458, Galactic Archaeology: Near-Field Cosmology
    and the Formation of the Milky Way, ed. W. Aoki,
    M. Ishigaki, T. Suda, T. Tsujimoto, & N. Arimoto, 405

Nicholl, M., Smartt, S. J., Jerkstrand, A., et al. 2013,
    Nature, 502, 346

Nidever, D. L., Bovy, J., Bird, J. C., et al. 2014, ApJ, 796,
    38

Nidever, D. L., Holtzman, J. A., Allende Prieto, C., et al.
    2015, AJ, 150, 173

Nishimura, N., Sawai, H., Takiwaki, T., Yamada, S., &
    Thielemann, F.-K. 2017, The Astrophysical Journal, 836,
    L21

Nissen, P. E. 2015, A&A, 579, A52

Nissen, P. E., Christensen-Dalsgaard, J., Mosumgaard,
    J. R., et al. 2020, A&A, 640, A81

Nordström, B., Mayor, M., Andersen, J., et al. 2004, A&A,
    418, 989

Pérez, F., & Granger, B. E. 2007, Computing in Science &
    Engineering, 9, 21, doi: 10.1109/MCSE.2007.53

Peters, J. G. 1968, ApJ, 154, 225

Pinsonneault, M. H., Elsworth, Y. P., Tayar, J., et al. 2018,
    The Astrophysical Journal Supplement Series, 239, 32,
    doi: 10.3847/1538-4365/aaebfd

Pires, S., Mathur, S., García, R. A., et al. 2015, A&A, 574,
    A18

Piskunov, N., & Valenti, J. A. 2017, A&A, 597, A16

Pont, F., & Eyer, L. 2004, MNRAS, 351, 487

Prochaska, J. X., Naumov, S. O., Carney, B. W.,
    McWilliam, A., & Wolfe, A. M. 2000, AJ, 120, 2513

Qian, Y. Z., & Woosley, S. E. 1996, ApJ, 471, 331

Raiteri, C. M., Gallino, R., Busso, M., Neuberger, D., &
    Kaeppeler, F. 1993, ApJ, 419, 207

Rendle, B. M., Miglio, A., Chiappini, C., et al. 2019,
    MNRAS, 490, 4465

Reyes, C., Stello, D., Hon, M., & Zinn, J. C. 2022, arXiv
    e-prints, arXiv:2202.05478.
    https://arxiv.org/abs/2202.05478

Rosswog, S., Liebendörfer, M., Thielemann, F. K., et al.
    1999, A&A, 341, 499

Saha, K., Tseng, Y.-H., & Taam, R. E. 2010, ApJ, 721,
    1878, doi: 10.1088/0004-637X/721/2/1878

Salaris, M., Chieffi, A., & Straniero, O. 1993, ApJ, 414, 580

Schönrich, R., & Aumer, M. 2017, MNRAS, 472, 3979

Schönrich, R., & Binney, J. 2009a, MNRAS, 396, 203

—. 2009b, MNRAS, 399, 1145

Schönrich, R., McMillan, P., & Eyer, L. 2019, MNRAS,
    487, 3568

Schwarzschild, M., & Härm, R. 1967, ApJ, 150, 961

Sharma, S., & Stello, D. 2016, Asfgrid: Asteroseismic
    parameters for a star. http://ascl.net/1603.009

Sharma, S., Stello, D., Bland-Hawthorn, J., Huber , D., &
    Bedding, T. R. 2016, ApJ, 822, 15,
    doi: 10.3847/0004-637X/822/1/15

Sharma, S., Stello, D., Buder, S., et al. 2018, MNRAS, 473,
    2004

Sharma, S., Stello, D., Bland-Hawthorn, J., et al. 2019,
    MNRAS, 490, 5335

Sharma, S., Hayden, M. R., Bland-Hawthorn, J., et al.
    2021, MNRAS, 506, 1761, doi: 10.1093/mnras/stab1086

Sheinis, A., Barden, S., Birchall, M., et al. 2014, in Society
    of Photo-Optical Instrumentation Engineers (SPIE)
    Conference Series, Vol. 9147, Ground-based and Airborne
    Instrumentation for Astronomy V, ed. S. K. Ramsay,
    I. S. McLean, & H. Takami, 91470Y

Siegel, D. M., Barnes, J., & Metzger, B. D. 2019, Nature,
    569, 241

Silva Aguirre, V., Casagrande, L., Basu, S., et al. 2012,
    ApJ, 757, 99, doi: 10.1088/0004-637X/757/1/99

Silva Aguirre, V., Bojsen-Hansen, M., Slumstrup, D., et al.
    2018, MNRAS, 475, 5487

Spitoni, E., Silva Aguirre, V., Matteucci, F., Calura, F., & Grisoni, V. 2019, A&A, 623, A60

Spitzer, Jr., L., & Schwarzschild, M. 1951, ApJ, 114, 385, doi: 10.1086/145478

Steffen, M., Prakapavičius, D., Caffau, E., et al. 2015, A&A, 583, A57

Steinmetz, M., Zwitter, T., Siebert, A., et al. 2006, AJ, 132, 1645

Stello, D., Chaplin, W. J., Basu, S., Elsworth, Y., & Bedding, T. R. 2009, MNRAS, 400, L80, doi: 10.1111/j.1745-3933.2009.00767.x

Stello, D., Compton, D. L., Bedding, T. R., et al. 2014, ApJL, 788, L10

Stello, D., Huber, D., Sharma, S., et al. 2015, ApJL, 809, L3, doi: 10.1088/2041-8205/809/1/L3

Stello, D., Zinn, J., Elsworth, Y., et al. 2017, ApJ, 835, 83, doi: 10.3847/1538-4357/835/1/83

Stello, D., Saunders, N., Grunblatt, S., et al. 2021, arXiv e-prints, arXiv:2107.05831

Sun, W. X., Huang, Y., Wang, H. F., et al. 2020, ApJ, 903, 12

Symbalisty, E. M. D., Schramm, D. N., & Wilson, J. R. 1985, ApJL, 291, L11

Timmes, F. X., Woosley, S. E., & Weaver, T. A. 1995, ApJS, 98, 617

Ting, Y.-S., & Rix, H.-W. 2019, ApJ, 878, 21, doi: 10.3847/1538-4357/ab1ea5

Tinsley, B. M. 1979, ApJ, 229, 1046

Truran, J. W., & Arnett, W. D. 1971, Ap&SS, 11, 430

Truran, J. W., Cowan, J. J., Pilachowski, C. A., & Sneden, C. 2002, PASP, 114, 1293

Ulrich, R. K. 1986, ApJL, 306, L37, doi: 10.1086/184700

Valenti, J. A., & Piskunov, N. 1996, A&AS, 118, 595

Vanderburg, A., & Johnson, J. A. 2014, PASP, 126, 948, doi: 10.1086/678764

Viani, L. S., Basu, S., Chaplin, W. J., Davies, G. R., & Elsworth, Y. 2017, ApJ, 843, 11

Virtanen, P., Gommers, R., Oliphant, T. E., et al. 2020, Nature Methods, 17, 261, doi: https://doi.org/10.1038/s41592-019-0686-2

Vlasov, A. D., Metzger, B. D., & Thompson, T. A. 2014, MNRAS, 444, 3537

Walt, S. v. d., Colbert, S. C., & Varoquaux, G. 2011, Computing in Science & Engineering, 13, 22, doi: 10.1109/MCSE.2011.37

Wanajo, S., Janka, H.-T., & Müller, B. 2011, ApJL, 726, L15, doi: 10.1088/2041-8205/726/2/L15

Warfield, J. T., Zinn, J. C., Pinsonneault, M. H., et al. 2021, AJ, 161, 100

Weinberg, D. H., Holtzman, J. A., Hasselquist, S., et al. 2019, ApJ, 874, 102

White, T. R., Bedding, T. R., Stello, D., et al. 2011, ApJ, 743, 161

Wilson, J. C., Hearty, F. R., Skrutskie, M. F., et al. 2019, PASP, 131, 055001

Wittenmyer, R. A., Sharma, S., Stello, D., et al. 2018, AJ, 155, 84

Wolniewicz, L. M., Berger, T. A., & Huber, D. 2021, AJ, 161, 231

Yanny, B., Rockosi, C., Newberg, H. J., et al. 2009, AJ, 137, 4377

Yıldız, M., Çelik Orhan, Z., & Kayhan, C. 2016, MNRAS, 462, 1577

Yu, J., Huber, D., Bedding, T. R., et al. 2018, ApJS, 236, 42, doi: 10.3847/1538-4365/aaaf74

Zasowski, G., Johnson, J. A., Frinchaboy, P. M., et al. 2013, AJ, 146, 81

Zasowski, G., Cohen, R. E., Chojnowski, S. D., et al. 2017, AJ, 154, 198

Zhao, G., Mashonkina, L., Yan, H. L., et al. 2016, ApJ, 833, 225

Zhou, Y., Asplund, M., Collet, R., & Joyce, M. 2020, MNRAS, 495, 4904

Zinn, J. C., Huber, D., Pinsonneault, M. H., & Stello, D. 2017, ApJ, 844, 166, doi: 10.3847/1538-4357/aa7c1c

Zinn, J. C., Pinsonneault, M. H., Huber, D., & Stello, D. 2019a, The Astrophysical Journal, 878, 136, doi: 10.3847/1538-4357/ab1f66

Zinn, J. C., Pinsonneault, M. H., Huber, D., et al. 2019b, ApJ, 885, 166, doi: 10.3847/1538-4357/ab44a9

Zinn, J. C., Stello, D., Huber, D., & Sharma, S. 2019c, ApJ, 884, 107, doi: 10.3847/1538-4357/ab43c0

Zinn, J. C., Stello, D., Elsworth, Y., et al. 2020, The Astrophysical Journal Supplement Series, 251, 23